Università degli Studi di Catania

Dipartimento di Fisica e Astronomia
Dottorato di Ricerca in Fisica - XXVI Ciclo

Gianpaolo Garilli

Study of the performances of the AMIGA muon detectors of the Pierre Auger Observatory

PhD Thesis

Coordinatore:
Prof. F. Riggi

Tutors:
Prof. A. Insolia
Dr. A. Castellina

Triennio 2010-2013

Contents

Introduction

The evolution of the spectrum through the second knee and ankle, and the corresponding predicted changes in composition, are crucial to the understanding of the end of Galactic confinement and the effects of propagation on the lower energy portion of the extragalactic flux. The latter is strongly related to the cosmological distribution of sources and to the composition of the injected spectrum. To study this energy region, the Pierre Auger Collaboration has extended the energy range of its Observatory in Argentina from 3×10^{18} down to 10^{17} eV by means of new detectors including three additional fluorescence telescopes with a more elevated field of view (HEAT) and a nested surface array with 750 m spacing and additional muon detection capabilities (AMIGA). With these enhancements, the Pierre Auger Observatory will provide full efficiency detection of cosmic rays down to 10^{17} eV, a direct measurement of the muonic component of the extensive air showers (EAS), and the possibility to study the transition between the galactic and the extragalactic component of high energy cosmic rays.

The number of muons in extensive air showers reflects the composition of the primary cosmic rays which interact at the top of the atmosphere; together with the optical detection of the depth of maximum development of the showers it can be used to disentangle the composition information from the different hadronic models scenarios. The muon detectors of AMIGA allow to perform a direct measure of the muonic component of the showers, exploiting the fact that muons lose a small fraction of their energy in the atmosphere and can penetrate several meters underground, while the lower energy electromagnetic component is on the contrary almost completely absorbed.

The main aim of this work is that of evaluating the performances of the muon counters of AMIGA. They have been studied during the costruction phase of six

modules in the mechanical workshop of INFN-Torino (Italy) and by developing a simulation code to study the propagation of the particles through air and soil down to the scintillator detectors, in order to evaluate their response.
This thesis is organized as follows.
In the first chapter, a general overview of cosmic rays physics will be given, with particular attention to the energy region hosting the transition between a galactic and an extragalactic origin of cosmic rays.
In the second chapter, the EAS characteristics will be discussed, focusing on the muonic component and analyzing the relevant interaction processes and energy losses.
A general description of the Pierre Auger Observatory is presented in Chapter 3, where we underline the characteristics of the Surface and Fluorescence Detectors. The Infill area enhancements, and in particular the AMIGA one, object of this thesis, are discussed presenting their science motivation.
In the fourth chapter, the technical characteristics of the muon detectors will be introduced, describing all their components in detail. An analysis of the counter segmentation and muon pile-up correction will be made.
The basic properties of the muon detectors as measured during the construction will be discussed in the fifth chapter describing the tests performed to check their technical performances and the calibration procedure.
In chapter 6, we describe the simulation of the muon detector, in which extensive use of the laboratory measurements described above are made. We also explain how a library of muon traces, adequately filtered and resampled in order to fulfill the requirements of the module electronics, has been created.
A brief introduction to the simulation framework based on Geant4 and CORSIKA will be made in chapter 7. We describe the Module Sequence written to simulated the AMIGA detector and its inclusion in the $\overline{Offline}$ software framework developped by the Pierre Auger Collaboration, giving a detailed description of: (a) the calculation of the mean number of photoelectrons from the energy deposited by particles in the scintillator; (b) the evaluation of the detector efficiency for different muon counting strategies.
Finally in the eighth chapter, the results of the simulations both with a single particle beam and with showers will be discussed.

Chapter 1

Cosmic Rays

1.1 Short history

The study of cosmic rays started approximately in 1900 as a result of the observation of ionization in gases contained in closed vessels. First hypothesis to explain this phenomena were that it was the consequence of radioactive radiation coming from the surface of the Earth, from the walls of the vessel or from radioactive emanations in the gas. In order to rule out these hypothesis, balloon flights were undertaken. They led to the definite discovery of the cosmic rays by Victor Hess in 1912 (Hess V. F., 1912) (Fig. 1.1), who observed that the ionization rate at altitude around 5 km was several times that the observed at sea level, and therefore, the radiation must come from outside the Earth.

The term Cosmic Rays to this radiation was coined by Robert Millikan. The interaction of the Earths magnetic field on charged particles propagation trough the atmosphere was discovered in 1927. It was demonstrated that it affects the cosmic rays that come from the East differently than those from the West, so that it was proved that cosmic rays are mainly charged particles. The discovery of cosmic rays was an invaluable tool for early particle physicists because they are the most energetic particles of the Universe and, when hitting the atmosphere, provide the circumstances for the creation of previously undiscovered particles. In 1931, Anderson (Anderson C. D., 1961) gave the proof of the existence of a positively charged particle with an identical mass as the electron using cosmic rays. This particle had been previously proposed by Dirac (Dirac P. A. M., 1931)

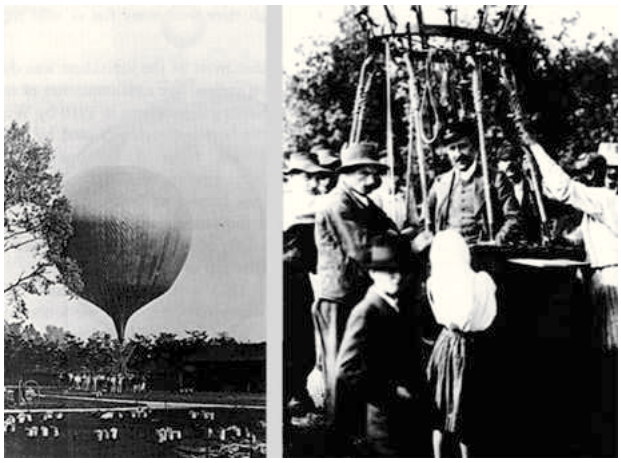

Figure 1.1: V. Hess in the balloon flights which led to the discovery of cosmic rays.

and it was correctly interpreted later as an anti-electron, called positron. Anderson and Hess shared the Nobel prize in 1936 for their work. In 1937 Anderson and Neddermeyer, and at the same time Street and Stevenson (Griffiths D., 1987), discovered a particle with the same mass as the one that Yukawa had proposed associated with the strong nuclear force (Lattes C. M. G., 1947). It was in 1947 when it was discovered that they are two different particles with similar masses that abound in cosmic ray air showers, called muon (μ) and pion (π). The latter was the one proposed by Yukawa. In 1947, a new type of particle was discovered that was different from the previously known ones. It was a new particle with the mass of at least twice that of pions later called the kaon (K^0) (Rochester G. D. and Butler C. C., 1947). It is formed by strange quarks, and it was the first of these kind of particles that were discovered using cosmic rays. A crucial advance by Pierre Auger and collaborators took place in 1938 (Auger P., 1939). They observed an unexpectedly high rate of coincidences among counters located at the same altitude and separated by large distances using electronics with microsecond timing. They correctly interpreted this result as proving the existence of Extensive Air Showers (EAS) generated by a single particle, the cosmic ray, entering in the atmosphere. The interaction of a cosmic ray of high enough energy with an atmospheric nucleus causes a cascade of particles falling to the Earth surface at the same time. On the basis of their measurements, and using a sim-

ple model of shower development and the distance between counters, they were able to estimate that the energy of this primary particle should be as high as 10^{15} eV. In the second half of the 20th century, first studies of the high energy cosmic rays have been performed. Large array of surface detectors were first used encouraged by Bassi et al. at MIT in 1953 (Bassi P., G. Clark, and B. Rossi, 1953), who were able to reconstruct the original direction of the cosmic ray from the timing information in their array of scintillation detectors. In 1963, Linsley, using the Volcano Ranch array, detected for the first time a cosmic ray with an energy estimated to be as large as 10^{20} eV (Linsley J., 1963). Five years later, Tanahashi detected an air shower from an incident cosmic ray of 10^{19} eV using a different technique: fluorescence in the atmosphere (Hara T., 1970). In the subsequent years, the ultrahigh energy events have been studied either by means of scintillator or water detectors in ground arrays at Haverah Park (Edge D., 1973), SUGAR (Bell C., 1974), Akeno (Nagano M, 1992), and AGASA (Chiba N., 1992) or by means of a new technique exploiting air fluorescence in atmosphere at Fly's Eye (Baltrusaitis R.M., 1985) and HiRes (Bird D. J., 1993). The Pierre Auger Observatory (Abraham J., 2004) is going to study the final region of the cosmic rays energy spectrum, those with energies above 10^{18} eV, which are called ultrahigh energy cosmic rays (UHECRs). It started taking data in 2004 and uses the hybrid technique, that together with its huge array, provides the best chance to go further in cosmic ray discoveries. Over the past thirty years, the new field of the "astroparticle physics" aims understanding the nature and structure of the matter in the universe.

1.2 Cosmic rays flux and composition

To understand the origin and nature of the cosmic rays we begin with the analysis of their all particle energy spectrum. The cosmic ray spectrum extends over about 12 decades in energy with a flux which follows a power law $E^{-\gamma}$ and spans about 32 orders of magnitude (see Figure 1.2). At several GeV, particles hit the Earth with a differential flux about 1000 particles/$m^2 sec$. This flux is reduced to $\sim$ 1 particle/$m^2 year$ for energies in the PeV region and further to 1 particle/$km^2 century$ for energies above 100 EeV.

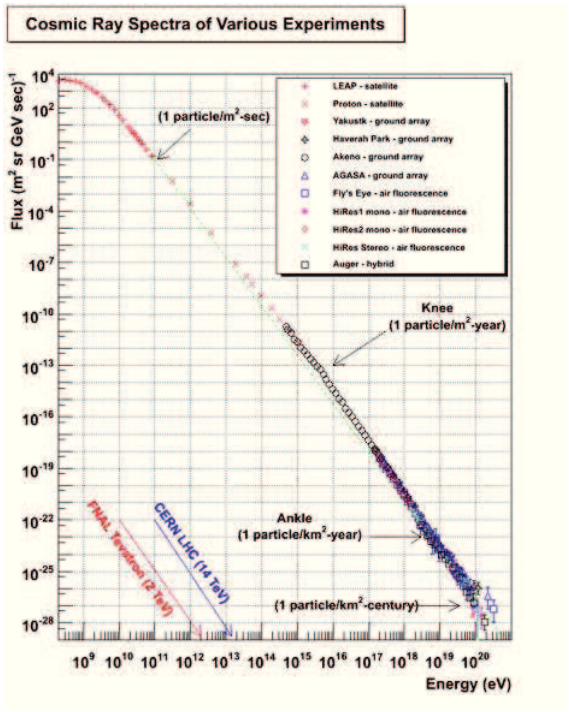

Figure 1.2: All-particle energy spectrum of cosmic rays measured by several experiments.

Up to energies of 10^{14} eV, cosmic rays can be detected directly and identified in satellite-based or balloon-borne experiments. The low flux at higher energies, on the contrary, requires long measurement periods and large detection areas; these cosmic rays are measured indirectly by the registration of secondary particles produced in extensive air shower (EAS) with experiments on Earth, that can be located at different altitudes. The flux ϕ of particles as a function of energy E can be described by a broken power law

$$\frac{d\phi}{dE} \propto E^{-\gamma} \tag{1.1}$$

with spectral index γ.

Different features in the spectrum are described with a change in the spectral index. A first kink appears at $\sim 4 \times 10^{15}$ eV: the so called *knee* indicates a change in the source mechanism, and thus in acceleration processes of the cosmic rays. This is consistent with the idea that the galactic cosmic rays are accelerated by supernovae and the acceleration process becomes less efficient above 10^{15}

eV. The knee can be interpreted as superposition of the energy spectra of the different elements, that exhibit their cutoff at different energies. It is still under investigation whether the exact shape of the knee can be described by a rigidity or mass dependent cutoff energy.

From 10^{16} eV to $4 \times 10^{18} eV$ the spectrum is again a power-law with spectral index 3.0 - 3.1. The existence of a *second knee* at around 4×10^{17} eV has been observed by Akeno (Nagano M., 1984), Flys Eye stereo (Abu-Zayyad, 2001), Yakutsk (Pravdin M.I., 2003) and HiRes (Douglas R. Bergman, 2004). This feature could be the signature of the end of the galactic component and of the emergence of the extragalactic one, provided that the latter cuts off at low energies. It would primarily be caused by the break of the galactic Fe component.

The region round $10^{18.5}$ eV, known as *ankle*, appears with a flattening of the spectrum. Debating interpretations are currently present in literature, dealing with the transition from galactic to extragalactic sources and with the source properties. The ankle at $\sim 3 \cdot 10^{18}$ eV was first observed by Haverah Park, Akeno, and Yakutsk and is traditionally explained in terms of the transition from galactic to EGCRs. The key point here is that one expects the galactic magnetic field to lose its efficiency at about this energy as the gyroradius of a particle at charge Z in a μGauss field, $r_g \simeq 1\ kpc Z^{-1} B_{\mu G}^{-1}$, becomes comparable to the thickness of the galactic disk. It then becomes natural to think of hard EGCRs starting to penetrate into the galaxy and dominating the flux at higher energies.

The *ankle* has been reported convincingly by a number of experiments, but there is still no consensus about the existence of a *second knee*. This is because of both the weakness of the structure making it difficult to detect and because of only few experimental data, most of which are either at their upper or lower limit of detectable energies.

Above $10^{19.5}$ eV the experimental data of HiRes and Auger, put in evidence a cutoff in the spectrum, compatible with the suppression expected from the GZK effect.

1.2.1 The galactic component

1.2.1.1 Direct measurements

The composition of the cosmic radiation has been studied with the highest precision by satellite and balloon experiments up to energies of 10^{14} eV. Up to these energies CR are mainly composed by about 98% of hadrons and about 2% of electrons. Only $\sim$ 0.2% is composed by photons and neutrinos. The hadronic component is dominated by protons (87%) and helium (12%), while the rest 1% corresponds to fully ionized nuclei of heavy elements. The predominance of protons and helium nuclei is due to the fact that the Earths magnetic field and the solar wind shield heavy nuclei. Comparing the relative abundances of cosmic rays with those of Solar System elements, a similar trend with some exceptions is observable (Figure 1.3a). The first is the lower abundance of hydrogen and helium in the cosmic radiation with respect to the abundance in oursolar system. This is probably originate from their relatively high ionization energies and, since the most popular acceleration processes are only efficient for charged particles, it is assumed that only the ionized fraction of hydrogen and helium atoms is accelerated. The second exceptions concerns two groups of elements, Li, Be, B and Sc ,Ti ,V ,Cr ,Mn, that are more abundant in the cosmic ray composition than in the Solar System. This discrepancy is easily explained as a result of spallation. In fact the primary cosmic rays accelerated in their sources have to propagate through the interstellar medium to reach the Earth and in this process there are spallation phenomena between the cosmic rays and the ambient interstellar gas. The net result is that the common elements in the cosmic rays are chipped away and fragmented populating the nuclear channel with atomic and mass numbers just less than those of the common groups of elements. Those elements which are produced in large abundances in the sources are called *primary elements*, while those mainly produced by spallation in the interstellar gas are called *secondary elements*. In Figure 1.3b the energy spectra for protons, helium, carbon and iron nuclei are plotted as a function of the kinetic energy per nucleon.

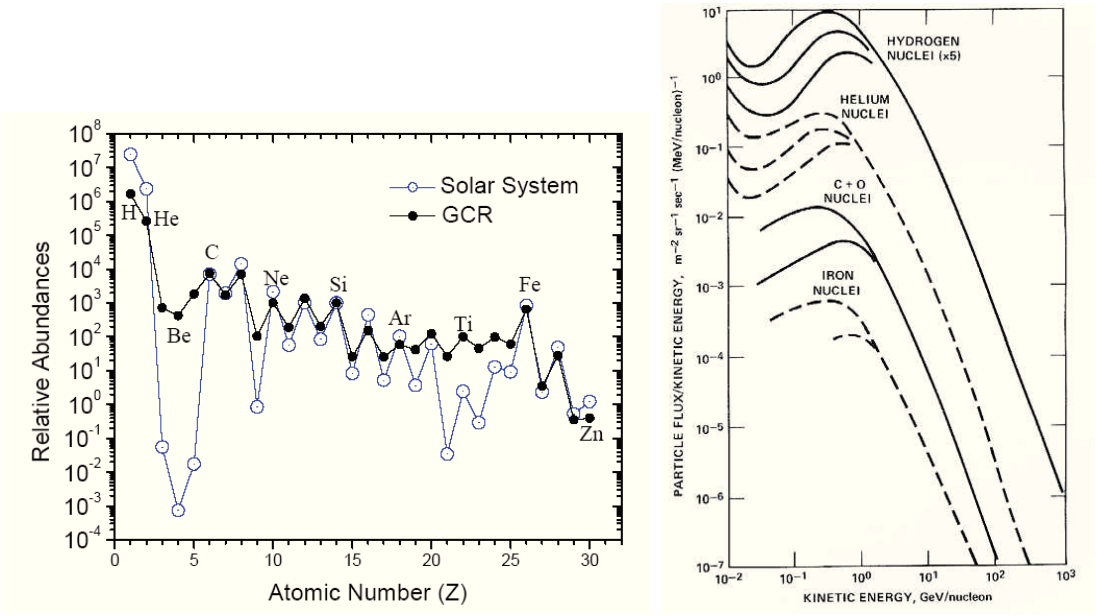

(a) (b)

Figure 1.3: (a): The abundances of various nuclei in the cosmic radiation compared to the abundances in the solar system. The nuclear charge scale refers to the elementary group H-Ni. The abundances are normalized to Si=1. (Compilation is based on (Wefel J. P., 1991)); **(b):** Cosmic rays energy spectra for the major components present in the primary radiation.

1.2.1.2 The Knee

At energies around the knee, since it is not possible to perform a direct measurement of the cosmic radiation, the nature of primary particles is inferred from Extensive Air Shower studies. Proposed explanations in the literature for the knee may be divided into four categories. The first three discuss astrophysical reasons, arguing that the knee is an intrinsic property of the energy spectrum, while in the last class the authors consider new particle physics processes in the atmosphere. In these theories the knee does not exist in the primary energy spectrum, but is only an effect of observing extensive air showers in the atmosphere: **I:** Models in the first category relate the knee to the acceleration process. The standard approach of particle acceleration in shock fronts from supernova explosions and several extensions are discussed in the models by (Berezhko E.G. and

Ksenofontov L.T., 1999), (Stanev T., 1993), (Kobayakawa K., 2002), and (Sveshnikova L.G., 2003). The maximum energy attained is taken to be responsible for the knee. Also source related is the proposal of (Erlykin A.D. and Wolfendale A.W., 2001), namely that a nearby supernova as a single source of cosmic rays causes the structure in the energy spectrum. (Volk H.J. and Zirakashvili V.N., 2003) consider reacceleration by spiral shocks in the galactic wind. (Plaga R., 2002) proposes cosmic rays being accelerated by cannon balls ejected into the galactic halo.

II: Models of the second category connect the knee with leakage of cosmic rays from the Galaxy. (Swordy S.P., 1995) combines diffusive shock acceleration with an energy dependent propagation pathlength in a Leaky Box model. In the models by (Lagutin A.A., 2001), (Ogio S. and Kakimoto F., 2003) the knee follows from diffusive propagation of cosmic-ray particles through the Galaxy.

III: Interactions of cosmic rays with background particles in the Galaxy are considered as origin for the knee in the third category. (Tkaczyk W., 2001) suggests diffusive propagation in combination with photo-disintegration. (Candia J., 2002) discuss the interaction of cosmic rays with the neutrino background.

IV: A last class of theories accounts the air shower development in the atmosphere for the knee. The basic idea is that a new type of interaction transfers energy to a component not observable (or not yet observed) in air shower experiments. The threshold for these new interactions is in the knee region, above the energy of todays collider experiments. In the model by Kazanas and Nicolaidis the energy is transfered into techni-hadrons, lightest supersymmetric particles, and gravitons.

1.2.2 The extragalactic component

Cosmic rays during their propagation could interact with background radiation fields like the cosmic microwave background (CMB), the infrared background (IB) and radio background (RB), losing energy. Other energy losses are due to the Hubble expansion of the Universe and due to the interaction with dust, but they are not significant at the energies of our interest. The most important interaction at the highest energies is the GZK effect proposed by Greisen (Greisen K., 1966),

Zatsepin, and Kuzmin (Zatsepin G. T. and Kuzmin V. A., 1966) immediately after the CMB discovery by Penzias and Wilson in 1965 (Penzias A. A. and Wilson R. W., 1965). They independently pointed out that this radiation would make the Universe opaque to cosmic rays of sufficiently high energy. Protons with an energy exceeding $E \sim 5 \times 10^{19}$ eV (called GZK threshold) have a large probability to interact with the CMB photons, losing energy by pion photo-production:

$$p + \gamma_{CMB} \rightarrow p + \pi^0 \tag{1.2}$$

$$p + \gamma_{CMB} \rightarrow n + \pi^+ \tag{1.3}$$

These interactions occur via the Δ^+ resonance whose cross section at that energy is very high ($\sim 10^{-28} cm^{-2}$). Assuming typical value for the CMB photon density (400 cm^{-3}), the mean free path[1] for a proton can be estimated as $\sim$ 8 Mpc. The energy loss per interaction for the proton is $\sim$ 20%, giving an attenuation length[2] of the order of some tenths of Mpc, beyond which the proton energy falls below the GZK threshold. Figure 1.4 shows how the energy of a proton degrades due to successive interactions with the CMB. On the other hand, the neutron decay length ($n \rightarrow p + e^- + \overline{\nu}_e$) is about 1 Mpc at 10^{20} eV, so that it decays before interacting.

If cosmic rays are protons, another energy loss process will be important between 10^{18} eV and the GZK threshold. It is the photo-pair production when protons interact with photons of the CMB producing a electron-positron pair ($p + \gamma_{CMB} \rightarrow p + e^+ + e^-$). The energy loss in each interaction is small. It may, however, contribute to the shape of the spectrum at these energies if the primaries are protons from distant sources. At lower energies the attenuation length tends to become constant and equal to the energy loss due to the expansion of the universe ($\sim$ 4 Gpc). If cosmic rays are nuclei of mass A, they will undergo due to photo-disintegration and pair production, both with CMB and IR backgrounds:

$$A + \gamma_{CMB,IR} \rightarrow (A-1) + N \tag{1.4}$$

[1]The average distance covered by a particle between subsequent interactions.

[2]The distance at which the probability that a particle has not been absorbed drops to 1/e.

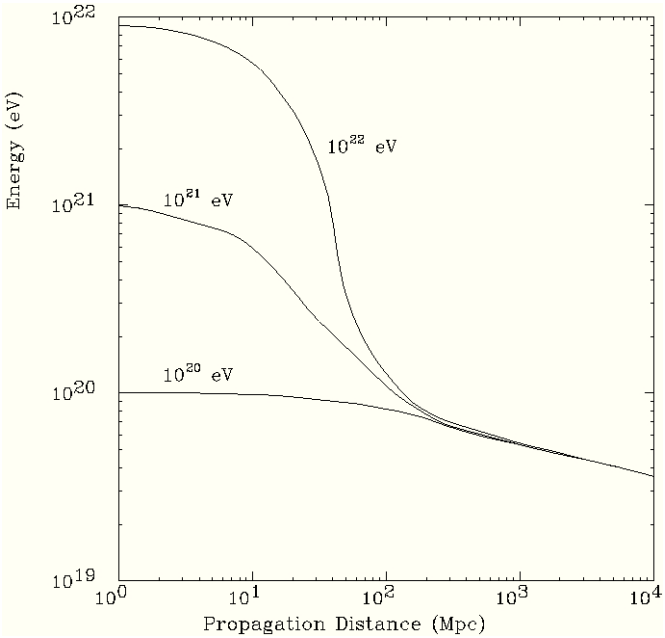

Figure 1.4: Energy of a proton traveling through the CMBR. The three curves correspond to three different starting energies (as noted), each one averaged from the simulation of 1000 protons (CroninJ. W., 1994).

$$A + \gamma_{CMB,IR} \rightarrow (A-2) + N \tag{1.5}$$

$$A + \gamma_{CMB,IR} \rightarrow A + e^+ + e^- \tag{1.6}$$

Since the energy is shared between nucleons, the threshold energy for these processes increases compared to that of protons. The inelasticity is lower by a factor $\sim 1/\mathrm{A}$, while the cross section increases with Z^2. This means that the loss length, in case of heavy nuclei, will be smaller ($\sim$ 1 Mpc) with respect to protons, but it occurs at a higher energies. Finally, if cosmic rays are photons, the dominant interaction is pair production with the cosmic background photons ($\gamma + \gamma_{CMB,IR} \rightarrow e^+ + e^-$). Pair creation with the CMB is important above 4×10^{14} eV while attenuation from pair creation with the radio background dominates the energy loss above 2×10^{19} eV. On the other hand, at energies higher than 10^{22} eV, the attenuation length grows to values of order of 100 Mpc, making possible

the hypothesis of photons as primary of extremely-high energy cosmic rays. In fact, these photons could produce secondary photons at energies higher than the GZK-threshold. If this were the case, a secondary photon spectrum $\propto E^{-2}$ should be observed, independently on the source spectrum.

1.2.3 The transition region

In this section we discuss the region of transition between galactic and extragalactic cosmic rays. Currently it is not well defined partially because of the low statistics at the highest end of the cosmic ray spectrum. This transition may occur at position of the second knee. There is a debate on the transition from the galactic to the extragalactic cosmic ray component. The most popular models explaining this features are:

- The ankle model (Hillas A.M., 1984): it is assumed that the transition occurs at the flat part of the observed spectrum in the energy interval $E \sim$ (3-10) EeV. The transition energy is given by the intersection of a flat extragalactic spectrum and a very steep galactic one. In the majority of ankle models the extragalactic component is assumed to be pure proton, while the galactic one should be naturally represented by Iron nuclei at energies above the Iron knee. These models predict a transition from an Iron-dominated composition to a proton-dominated one at the ankle energy.

- The dip model (Berezinsky V. and Grigoreva S.I., 1987): in this model the transition begins at the second knee and is completed at the beginning of the dip, at $E \sim 1$ EeV. The ankle in this model appears as an intrinsic part of the dip. Like in the ankle model, the transition here also occurs as an intersection of the flat extragalactic component (this flatness is especially prominent in the case of diffusive propagation) with a steep Galactic spectrum. In contrast to the ankle and mixed composition models, the dip model predicts an almost pure proton composition above $E \sim 1$ EeV and a pure Iron composition below this energy.

- The mixed composition model (Allard D., 2005): it is assumed that the extragalactic component consists of nuclei of various types. Thus transition here occurs from Iron to lighter nuclei of mixed composition; it can occur at the ankle or nearby it.

One feature is common for all of them: the transition is described as an intersection of a steep Galactic spectrum with a more flat extragalactic one. The three models have also to satisfy the "standard model" of galactic cosmic rays.

Detailed measurements of the composition as a function of energy, while not sufficient, would be valuable to break the present degeneracy among competing models for the Galactic-extragalactic transition (Medina-Tanco, 2007). Furthermore, this kind of information could help to determine what the highest energy accelerators in the Galaxy are and provide indicators of the kind and level of magnetohydrodynamic turbulence present in the intergalactic medium traversed by the lowest energy cosmic ray particles (De Donato C., 2007).

1.3 Sources and acceleration of UHECR

The origin of the highest energy cosmic rays is still a mystery. Different scenarios, explaining how and where they can gain such energies, are proposed and typically classified into two general category:
- The **bottom-up** scenario in which particles are accelerated from low energies to higher energies in astrophysical environments;
- The **top-down** scenario in which exotic particles, from early universe, decay producing cosmic rays.

1.3.1 Bottom-up scenarios

Bottom-up scenarios can be classified into models that assume a single-shock acceleration of particles in an electromagnetic field or statistical acceleration via Fermi acceleration in magnetized plasma. The maximum energy attainable in diffusive shock acceleration depends on the size and on the magnetic field strength

of the object where the acceleration takes place. Large sizes and strong fields are required to accelerate particles up to 10^{20} eV, since particles with a Larmor radius exceeding the size of the astrophysical objects are able to escape from the acceleration region. Hillas (Hillas A.M., 2006) proposed that in order to be able to accelerate charged particles they have to be at least partially confined into some acceleration region and that the maximum achievable energy is given by

$$E_{max}(EeV) \simeq \beta Z B(\mu G) L(kpc) \tag{1.7}$$

where β is the characteristic velocity of particles or fields driving the acceleration in a shock front, Z is the charge of the accelerated particle and B the magnetic field needed to keep the particles inside the acceleration region of size L. This relation is the basis for the so-called Hillas plot shown in Figure 1.5. It shows that to achieve a given maximum energy, one must have acceleration sites that have either a large magnetic field or a large size of the acceleration region. Only a few astrophysical sources such as active galaxies, hot spots of radio-galaxies, gamma ray bursts and compact objects like neutron stars, seem to satisfy the conditions necessary for acceleration of protons up to 10^{20} eV (diagonal line). Some remarks about them are given in the following:

- Pulsars ($B \sim 10^{13}\ Gauss,\ L \sim 10\ km$): They have a strong rotating magnetic field which results in a large electromotive force. This can trap the particle while accelerating it to high energies. However, there are some problems with this model. For example, the power law spectrum observed in cosmic rays is not immediately obvious in this scenario and, the acceleration occurs in a dense region of space where chances for energy loss are high due to meson photo-production, photo-nuclear fission and pair creation. These affect the energy spectrum and the composition of the resulting cosmic rays which are not in agreement with experimental data.

- Gamma Ray Burst (GRB, $B \sim 10^{9}\ Gauss,\ L \sim 10^{4} - 10^{5}\ km$): The origin of the detected gamma ray bursts can be explained by the collapse of massive stars or mergers of black holes or neutron stars. A relativistic shock is caused by a relativistic fireball in a pre-existing gas, such as a stellar wind, producing or

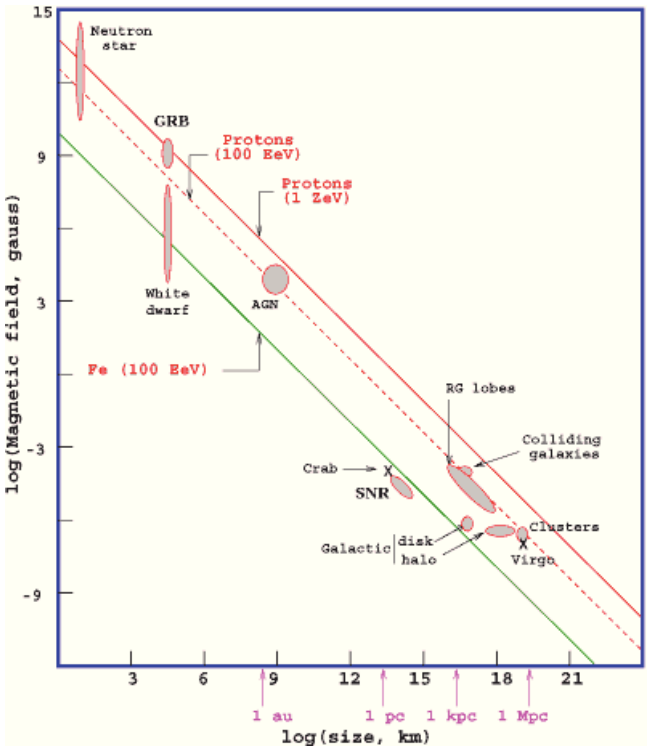

Figure 1.5: Adapted Hillas plot of the magnetic field strength required to accelerate protons and iron to a given energy as a function of the confinement region size. Objects must lie above the given lines in order to be able to accelerate particles to the given energies.

accelerating electrons/positrons to very high energies. The observed gamma-rays are emitted by relativistic electrons via synchrotron radiation and inverse Compton scattering. The detected GRBs release energy up to 10^{51} erg/s which would account for the luminosity required for cosmic rays above 10^{19} eV if the GRBs are uniformly distributed (independently of redshift). However, recent studies indicate that their redshift distribution seems to follow the average star formation rate of the Universe and that GRBs are more numerous at high redshifts.

- Active Galactic Nuclei (AGN, $B \sim 10^3\ Gauss,\ L \sim 10^{10}\ km$): AGNs are one of the most favored sources for cosmic rays at the highest energies (Protheroe R. J. and Szabo A. P., 1992). AGNs are powered by the accretion of matter onto a super massive black hole of $10^6 - 10^8$ solar masses. Typical

values of the central engine are L $\sim 10^{-2}$ pc and $B \sim 5$ G, which make possible the confinement of protons up to 10^{20} eV. The main problem here is the large energy loss in a region of high field density, which would limit the maximum energy achievable for protons and forbid the escape for heavy nuclei. Another solution is that the acceleration occurs in AGN jets, where particles are injected with Lorentz factors larger than 10 and energy losses are less significant.

- Cluster of Galaxies ($B \sim 10^{-6}\ Gauss,\ L \sim 0.1 - 1\ Mpc$)**:** Galaxy clusters are reasonable sites for ultra-high energy cosmic rays acceleration since particles with energy up to 10^{20} eV can be contained by cluster fields ($\sim 5\mu G$) in a region of size up to 500 kpc. Acceleration in clusters of galaxies could be originated by the large scale motions and the related shock waves resulting from structure formation in the Universe. However, losses due to interactions with the microwave background during the propagation inside the clusters limit UHECRs in cluster shocks to reach 10 EeV.

- Radio Galaxies Hot spots (RGH, $B \sim 0.1 - 1\ mGauss,\ L \sim 1\ kpc$**)** and **Radio Galaxies Lobes (RGL,** $B \sim 0.1\ \mu Gauss,\ L \sim 100\ kpc$**):** In Fanaroff-Riley II galaxies there are regions of intense synchrotron emission observed within their lobes, known as hot spots, and they are produced when the jet ejected by a central super massive black hole interacts with the intergalactic medium generating turbulent fields. The result is a strong shock responsible for particle re-acceleration and magnetic field amplification. The acceleration of particles up to ultra relativistic energies in the hot spots is achieved by repeated scattering through the shock front, similar to the Fermi acceleration mechanism. For typical hot-spot conditions, a maximum acceleration energy for protons is around 5×10^{20} eV.

1.3.2 Top-down scenarios

An alternative to acceleration models, introduced to explain the highest energy cosmic rays, are the so called top-down models, which involve the decay or annihi-

lation of exotic particles. These can be: topological and non-topological solitons, X-particles, cosmic defects, microscopic black-holes, fundamental strings, basically decaying in quarks and leptons. The quarks produce jets of hadron, mainly pions and a few percent of nucleons. The pions decay then to photons, muons, neutrinos (anti neutrinos) and electrons (positrons). The general characteristic of these models is a photon domination of the spectrum at the highest energies. This signature makes the hypothesis testable. In order to detect the produced UHECR, the X-particle must be super-massive ($> 10^{11}$ GeV). The density and the rate of decay must be large enough to account for an observable cosmic rays flux. Moreover, to avoid energy loss during the propagation from the source, the decays must take place within a limited distance ($\sim 100 Mpc$). To explain the UHECR one commonly classifies between two cases :

- Decay Top-Down Scenario: in this case unstable particles decay and, among their decay products the UHECR are produced. An unified formula for the quantum decay rate of all these objects was provided in (De Vega H.J.and Sanchez N.G., 2003). For all relics one has to fine tune the lifetime of these objects to be the age of the universe and the value of their mass that must be adjusted to be larger than 10^{20} eV. Heavy relics could have been formed by the end of inflation at typical GUTs energy scales.

- Annihilation Top-Down Scenario: other models proposed that stable heavy relics can produce UHECR through annihilation by pairs (Chung D.J.H., Kolb E.W. and Riotto A., 1999). In this scenario, the relics are assumed to have masses around $M_X \sim 10^{12}$ GeV and produce UHECR through annihilation when they collide. Here, the lifetime free parameter is replaced by the annihilation cross section. These super-heavy particles are assumed to be produced during reheating.

Chapter 2

Extensive Air Showers

2.1 Physics of extensive air showers

Direct measurements of CRs are possible only up to an energy around 10^{15} eV. Above this energy, the number of particles per unit of time, area and solid angle, namely the flux, is very low. In order to increase the number of detected particles, it is necessary to increase both the size of detectors and their observation time: ground based experiments are the only ones able to cover surfaces ranging from hundreds of m^2 to thousands of km^2. Extensive air showers (EAS) are the particle cascades generated by the interaction of an UHECR with an atom or a molecule in the atmosphere, which acts like a calorimeter of variable density. In Figure 2.1 we show a schematic representation of an extensive air shower. The cascades of secondary particles mainly develop through hadronic interactions, decays and energy-loss because of the emission of electromagnetic radiation. At ground level nucleons, mesons, muons, electrons, positrons and photons are generally observed.

A common approach to the study of EAS is to consider three main components: i) electromagnetic, consisting of electrons, positrons and photons, ii) muonic, consisting of muons generated by the decay of charged mesons, and iii) hadronic, consisting of nucleons and mesons. For instance, a 10^{19} eV primary proton produces at sea level more than 10^{10} particles: 99% of such particles, with energy between 1 and 10 MeV, contributes to the electromagnetic component, transporting $\sim$ 85% of total energy; the remaining 1% of particles are either muons, with an average energy of about 1 GeV (carrying about 10% of

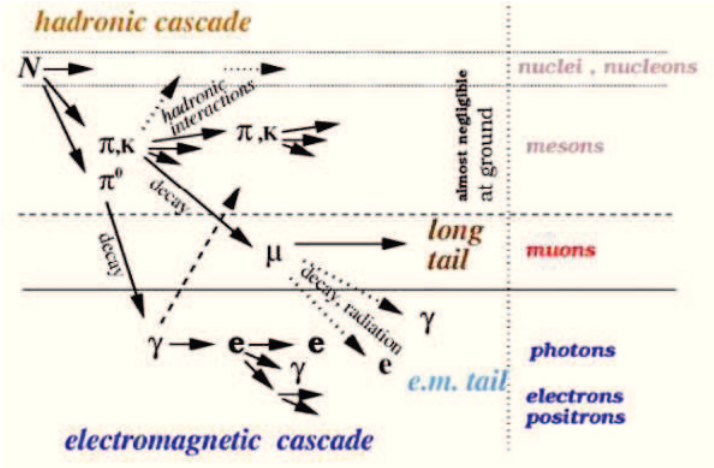

Figure 2.1: Schematic representation of an extensive air shower. A CR interacts with an atom or a molecule in the atmosphere and generates cascades of secondary particles, including nucleons, mesons, muons, electrons, positrons and photons at ground level.

the total energy), few GeV pions (about 4% of the total energy) and, in smaller proportions, neutrinos and baryons (Letessier-Selvon A. and Stanev T., 2011). A realistic modeling of EAS is rather difficult, because of the complex dynamics of interactions and decays to which the large number of secondary particle are subjected to. A simplified approach in the case of the electromagnetic cascade is due to Heitler (Heitler W., 1938), who had previously developed the theoretical background for the stopping of fast particles and positron creation with Bethe (Bethe H. and Heitler W. , 1934), and the passage of fast electrons with Bhabha (Bhabha H. and Heitler W. , 1937). Recently, a similar approach has been adopted to model hadronic showers (Matthews J. , 2005). In both cases, the main idea is to describe the cascade as a tree: the path from the sea level to the point where the cascade begins is divided into several slices. For electromagnetic cascades the length of each slice is equal to the radiation length, whereas in the case of hadronic cascades, it is equal to the interaction length. At each step, particles split their energy into two or more particles with smaller energy and this mechanism continues until a certain critical energy is reached. Such models are schematically represented in Figure 2.2, and we will describe them in more detail, in the following.

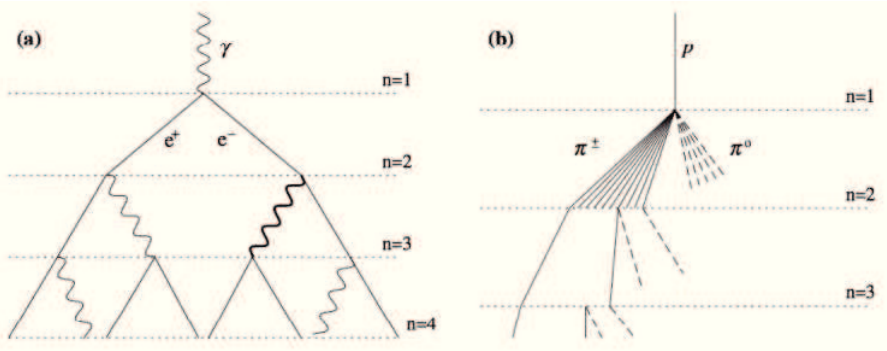

Figure 2.2: Heitler models for development of electromagnetic (a) and hadronic (b) cascades.

Electromagnetic cascade. The electromagnetic cascade is originated by the decay of neutral mesons producing high energy photons. The shower path is divided into n steps, and the interaction step-length is given by $d = \lambda_r log2$, being λ_r the radiation length λ_r of the medium ($\lambda_r = 37\ g/cm^2$ in air). At each step all particles interact, producing two secondary particles of equal energy: each photon produces an electron/positron pair, whereas electrons and positrons lose half of their energy by emitting a photon because of bremsstrahlung. The cross sections of processes are considered as independent of energy and collision energy losses are totally ignored. If E_0 is the energy of the primary photon, after n steps a number $N_n = 2^n$ of secondary particles is expected, each one with energy $E_n = E_0/N_n$. The shower development continues until E_n becomes smaller than a critical energy $\epsilon_\lambda (\approx 80\ MeV$ in air), more precisely when the rate of energy loss by electrons via bremsstrahlung is equal to the rate of energy loss by ionization. The number of particles reaches a maximum value $N_{max} = E_0/\epsilon_\lambda$ and increases no more until reaching the sea level. The atmospherical depth X_{max} at which N_{max} is reached depends on the first interaction point X_0 , and is defined by

$$X_{max} = X_0 + \lambda_r log \frac{E_0}{\epsilon_\lambda} \tag{2.1}$$

The *elongation rate*, defined as the rate of evolution of X_{max} with energy, is

defined by

$$D_{10}^{\lambda} \equiv \frac{dX_{max}}{d\ log_{10}E_0} = 2.3\lambda_r \tag{2.2}$$

that is $\approx 85\ g/cm^2$ in air. Monte Carlo simulations show that such predictions, obtained from a very simplified approach, qualitatively describe the electromagnetic shower development, with differences smaller than one order of magnitude.

Hadronic cascade. The hadronic cascade is originated by the decay of charged mesons producing high energy muons (and neutrinos). The approach is similar to that of the electromagnetic shower, although, in this case, the relevant parameter is the hadronic interaction length λ_h instead of λ_r . Another important difference is in the production of particles at each step: in fact, hadronic interactions produce multiple particles at each step. In this recent Heitler model for hadronic showers, it is assumed that $2N_\pi$ charged pions and N_π neutral ones are produced per interaction. Neutral pions contribute to the electromagnetic shower because of the decay $\pi^0 \rightarrow \gamma\gamma$, whereas π^+ and π^- continue to interact until their decay rate is more likely than a new interaction (the critical energy in this case is $\epsilon_\pi \approx 20GeV$ in air). The decay of charged pions produce muons via $\pi \rightarrow \mu\nu_\mu$, contributing to the muonic component of the EAS. In this case, the simplified model assume that i) interaction length and pion multiplicity do not depend on energy, ii) one third of the available energy goes into the electromagnetic component while the remaining 2/3rd continues as hadrons (Matthews J. , 2005). It is worth remarking that the density profile of the atmosphere is not constant and the critical energy is larger high above ground than at see level and deep showers will produce fewer muons. The number of steps needed to reach the critical energy is simply given by $n_n = log(E_0/\epsilon_\pi)/log(3N_\pi)$. By assuming that all pions decay into muons at the critical energy, the number of muons in the shower will be $N_\mu = (2N_\pi)^{n_c}$, or, equivalently, $N_\mu = (E_0/\epsilon_\pi)^\beta$, where $\beta = log(2N_\pi)/log(3N_\pi)$. For pion energy between 1 GeV and 10 TeV, $N_\mu = 5$ (hence, $\beta \simeq 0.85$) correctly describes the corresponding showers. At variance with the number of electrons in the electromagnetic shower, which grows linearly with the primary energy, the number of muons nonlinearly grows at a slower rate,

strongly depending on the value of β. Such a parameter depends on the multiplicity and on the inelasticity of the hadronic interactions. Simulations show that the value of β ranges from 0.9 to 0.95, compatible with the assumption that only half of the available energy goes into the pions at each step (rather than all of it, as previously assumed)(Alvarez-Muniz J., 2002). Moreover, at variance with the case of electromagnetic cascades, the position of shower maximum is more difficult to be determined. The larger cross section and the larger multiplicity at each step will reduce the value of X_{max} while the energy evolution of those quantities will modify the elongation rate. Hence, this simplified model only partially accounts for real observations. However, a more precise result can be obtained by mean of simulations. Assuming a proton-air cross section of 550 mb at 1 EeV and a rate of change of about 50 mb per decade of energy (Ulrich R., 2009), the interaction length becomes

$$\lambda_h \simeq 90 - 9log\Big(\frac{E_0}{EeV}\Big)\ g/cm^2. \tag{2.3}$$

If we assume that the first interaction initiates $2N_\pi$ electromagnetic cascades of energy $E_0/6N_\pi$, and $N_\pi \propto (E_0/PeV)^{1/5}$ for the evolution of the first interaction multiplicity with energy (Matthews J. , 2005) the elongation rate reads

$$D_{10}^p = \frac{dX_{max}}{dlog_{10}E_0} = \frac{d(\lambda_h log2 + \lambda_r log[E_0/(6N_{\pi\epsilon_\gamma})])}{dlog_{10}E_0} = \frac{4}{5}D_{10}^\gamma - 9ln2 \simeq 62\ g/cm^2, \tag{2.4}$$

in agreement with simulations. Such a value has been obtained under the hypothesis that the primary UHECR is a proton. The extension to heavier primary nuclei can be obtained by adopting the superposition model, where the nuclear interaction of a nucleus with atomic number A is simply viewed as the superposition of the interactions of A nucleons of individual energy E_0/A. It follows that showers from heavier nuclei develop faster than those from lightest ones. As a direct consequence, pions in the hadronic cascade reach their critical energy faster, increasing the relative number of muons with respect to the electromagnetic component. Hence, showers induced by nuclei will develop higher in the atmosphere, with $X_{max}^A = X_{max}^p - \lambda_r logA$, and will have a larger number of muons, namely $N_\mu^A = N_\mu^p A^{1-\beta}$. It is evident that the direct measurement of X_{max}

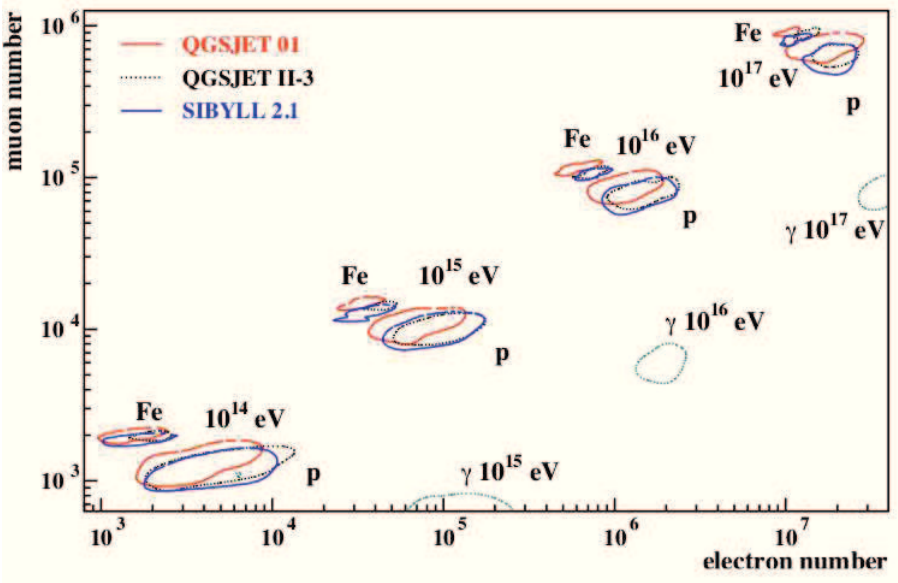

Figure 2.3: Expected number of muons and electrons in vertical showers, at sea level, originated by proton, iron and gamma-ray primaries. The curves show the full with at half maximum of the distributions for different primary particles and energies, as obtained with three different hadronic models (Blmer J.,Engel R. ,and Hrandel J., 2009).

and N_μ provides information about the mass of the primary cosmic ray. The predicted muon distributions depend on the assumptions on hadron production in air showers. This is evident in Figure 2.3 where the expected number of muons and electrons is shown for showers initiated by proton, iron, and gamma-ray primaries, as calculated with different interaction models.

2.2 Muons in EAS

Muons are the most numerous energetic charged particles at sea level. A charged particle cannot avoid losing energy by ionization. As it passes through matter the charged particle interacts with the electric fields and typically knocks loose some of the loosely bound outer electrons. A muon interacts very little with matter except by ionization. Because of this, muons can travel large distances and commonly reach the ground. However, they lose energy proportional to the amount of matter they pass. This is proportional to the density (g/cm^3) times the

path length (cm). This *interaction length* has units of grams per square centimeter (Interaction Depth[1]). Muons lose energy at a fairly constant rate of about 2 MeV per g/cm^2. Since the vertical depth of the atmosphere is about 1000 g/cm^2, muons will lose about 2 GeV to ionization before reaching the ground. The mean energy of muons at sea level is still 4 GeV. Therefore the mean energy at creation is probably about 6 GeV.

2.2.1 Interaction processes

For muons in the GeV energy range the only essential energy loss process is ionization, while for the muons underground other processes become important:
- Bremsstrahlung: this is the electromagnetic radiation produced by the acceleration of a charged particle when deflected by another charged particle, such as an atomic nucleus. The bremsstrahlung cross section for muons is

$$\frac{d\sigma_{Br}}{du} = \alpha\Big(2Zr_e\frac{m_e}{m_\mu}\Big)^2\frac{1}{u}\Big[\frac{4}{3}(1-u)+u^2\Big]\xi(\delta) \tag{2.5}$$

where u is the fraction of energy transferred to the photon and the screening function $\xi(\delta)$ depends on the minimum momentum tranfer to the nucleus $\delta = m_\mu^2 u/[2E(1-u)]$. The screening function has been parametrized with the form

$$\xi(\delta) = ln\Big[f_n\frac{m_\mu}{m_e}\frac{189Z^{-1/3}}{1+(\delta/m_e)\sqrt{e}189Z^{-1/3}}\Big] \tag{2.6}$$

where fn is the nuclear form factor (Petrukhin A.A., Shestakov V.V., 1968).

- Pair Production: in this process the muon emits a virtual photon that produces an electron-positron pair. Because of the two electromagnetic vertices

[1]At any point along the path, the number of interactions is proportional to the density times the path length. If we were to add up all of these interactions along the particle's path, we would get a number that should be proportional to the total absorption. If density has units of g/cm^3 and the path length is in units of cm, then this Interaction Depth, X, has units of g/cm^2.

the cross section is proportional to α^2 and not to as for the bremsstrahlung. In general form the cross section can be written as

$$\frac{d\sigma_{pair}}{dv} = \frac{2\alpha^2 r_e^2}{3\pi} Z^2 \frac{1-v}{v} \int [F_e(r) + \frac{m_e^2}{m_\mu^2} F_\mu(r)] dr \tag{2.7}$$

where v is the fractional energy loss of the muon and r is $(E_{e^+} - E_{e^-})/v$. (For the parametrizations of functions F_e and F_μ see ref (Kokoulin R.P., Petrukhin A.A., 1971). The cross section for pair production is higher than the bremsstrahlung one, however the energy losses of the two processes are of the same order.

- Photoproduction: in this case the muon emits a virtual photon that, interacting hadronically with matter, generates secondary hadrons. Only higher energy photons are important, so the cross-section for muon energies in the GeV range is very small. The photo- production cross-section for muons is given by

$$\frac{\sigma_{ph}(E_\mu)}{dv} = \frac{A\alpha}{2\pi} \sigma_{\gamma N}(vE_\mu) v \times F[E_\mu, v, \sigma(vE_\mu)] \tag{2.8}$$

where v is again the fractional energy loss of the muon and $\sigma_{\gamma N}$ is the interaction cross-section of a real photon with nucleons. (For the parametrization of functions F see ref. (Bezrukov L.B., Bugaev E.V., 1981)

In Figure 2.4 the relative energy loss is reported for the three processes in standard rock (an artificial material with atomic mass A = 22, atomic number Z = 11 and density 2.65 g/cm^3).

2.2.2 Energy loss

Ionization energy loss depends weakly on the muon energy so we can consider it as a constant, with a value of about 2 MeV per g/cm^2. The processes described above, instead, are proportional to the muon energy so the total muon energy loss becomes

$$\frac{dE_\mu}{dx} = -a - bE_\mu \tag{2.9}$$

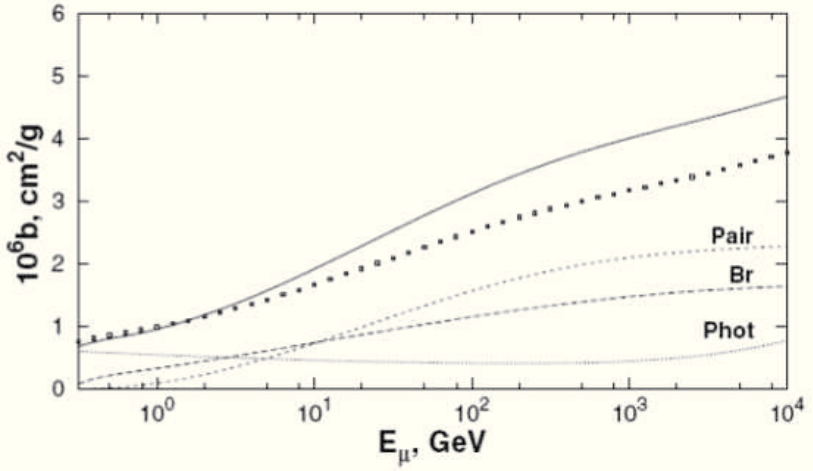

Figure 2.4: Relative energy loss in standard rock. Solid line shows the sum of the three processes. Circles show the energy loss for clean ice with density 0.93 g/cm^3.

where a is the ionization loss and b is the sum of the three contributions related to radiation processes

$$b = b_{br} + b_{pair} + b_{ph} \tag{2.10}$$

For standard rock it assumes a value of 4×10^{-6}. The energy at which the energy loss by radiation is equal to the one by ionization is the critical energy $\epsilon = a/b \simeq$ 500 GeV. When $E_\mu \gg \epsilon$ radiation processes dominate, while when $E_\mu \ll \epsilon$ ionization process dominates, as showed in Figure 2.5.

Now we can calculate the average energy E_μ of a muon with initial energy E_μ^0 after propagating through a material of thickness X expressed in (g/cm^2):

$$E_\mu = (E_\mu^0 + \epsilon) \times exp(-bX) - \epsilon \tag{2.11}$$

and the reverse quantity

$$E_\mu^0 = (E_\mu + \epsilon) \times exp(-bX) - \epsilon \tag{2.12}$$

So, from Eq.2.12 we can obtain also the minimum energy for a muon to

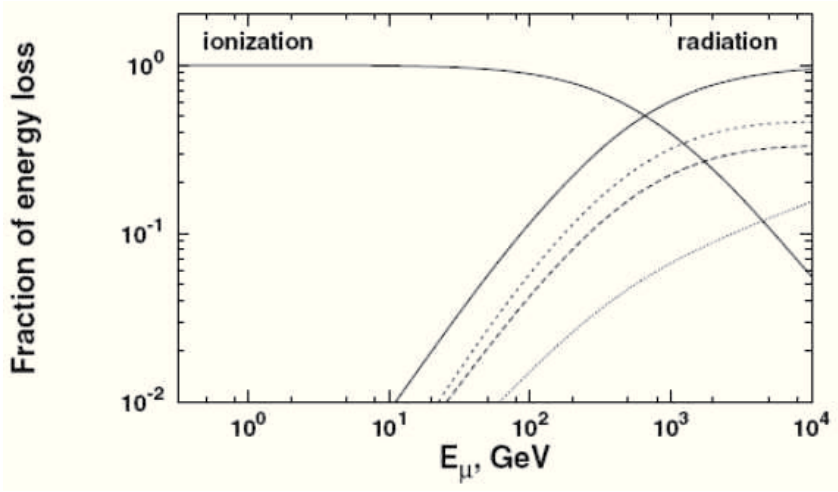

Figure 2.5: Relative importance of different energy loss processes as a function of the muon energy normalized to the total energy loss per g/cm^2.

penetrate at depth X

$$E_\mu^{min} = \epsilon[exp(bX) - 1] \tag{2.13}$$

The intensity of muons underground can be estimated from the muon intensity in the atmosphere and their rate of energy loss. To the extent that the mild energy dependence of a and b can be neglected, Eq.2.9 can be integrated to provide the following relation between the energy $E_{\mu,0}$ of a muon at production in the atmosphere and its average energy E_μ after traversing a thickness X of rock (or ice or water):

$$E_{\mu,0} = (E_\mu + \epsilon)e^{bX} - \epsilon \tag{2.14}$$

Especially at high energy, however, fluctuations are important and an accurate calculation requires a simulation that accounts for stochastic energy-loss processes (Lipari P. and Stanev T., 1991).
There are two depth regimes for which Eq.2.14 can be simplified. For $X \ll b^{-1} \approx$ 2.5 km water equivalent, $E_{\mu,0} \approx E_\mu(X) + aX$, while for $X \gg b^{-1}$

$E_{\mu,0} \approx (\epsilon + E_\mu(X))exp(bX)$. Thus at shallow depths the differential muon energy spectrum is approximately constant for $E_\mu < aX$ and steepens to reflect the surface muon spectrum for $E_\mu > aX$, whereas for $X > 2.5$ km.w.e. the differential spectrum underground is again constant for small muon energies but steepens to reflect the surface muon spectrum for $E_\mu > \epsilon \approx 0.5$ TeV. In the deep regime the shape is independent of depth although the intensity decreases exponentially with depth. In general the muon spectrum at slant depth X is

$$\frac{dN_\mu(X)}{dE_\mu} = \frac{dN_\mu}{dE_{\mu,0}} \frac{dE_{\mu,0}}{dE_\mu} = \frac{dN_\mu}{dE_{\mu,0}} e^{bX} \tag{2.15}$$

where $E_{\mu,0}$ is the solution of Eq.2.14 in the approximation neglecting fluctuations. Figure 2.6 shows the vertical muon intensity versus depth. In constructing this "depth-intensity curve", each group has taken account of the angular distribution of the muons in the atmosphere, the map of the overburden at each detector, and the properties of the local medium in connecting measurements at various slant depths and zenith angles to the vertical intensity. Use of data from a range of angles allows a fixed detector to cover a wide range of depths. The flat portion of the curve is due to muons produced locally by charged-current interactions of ν_μ . The inset shows the vertical intensity curve for water and ice published in Refs. (Babson J., 1990; Belolaptikov I.A., 1997; Desiati P., 1373; Pradier T. for ANTARES Collaboration, 2009). It is not as steep as the one for rock because of the lower muon energy loss in water.

In conclusion, at small depth ($X \ll 1/b\ g/cm^2$) muons lose energy mostly by ionization and $E_\mu^{min} \simeq aX$. The muon spectrum underground reflects the surface spectrum with a flattening under $E_\mu \simeq aX$. Instead at big depths ($X \gg 1/b\ g/cm^2$) the spectrum has an almost constant shape up to $E_\mu \approx \epsilon$.

2.3 Observables for composition studies

The UHECR mass composition is another key aspect to understand their origin and propagation. It can be inferred through observables related to the EAS development. This section is devoted to explain the main composition observables

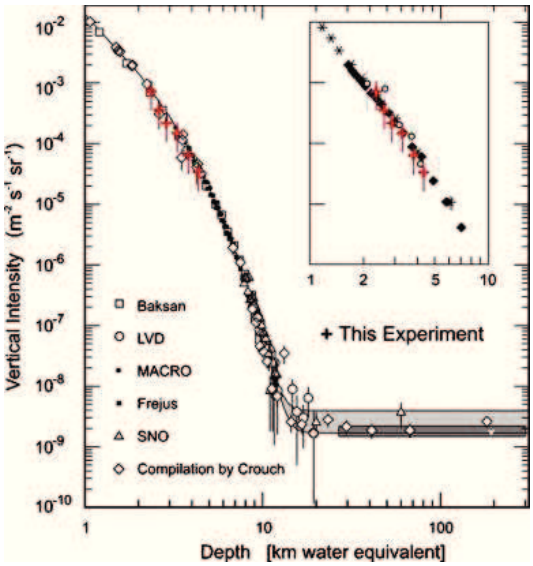

Figure 2.6: Vertical muon intensity vs depth (1 km.w.e. = 105 $g\ cm^{-2}$ of standardrock). The shaded area at large depths represents neutrino-induced muons of energy above 2 GeV. The upper line is for horizontal neutrino-induced muons, the lower one for vertically upward muons. Darker shading shows the muon flux measured by the SuperKamiokande experiment.

used by the Pierre Auger Observatory. First, the parameters from the fluorescence technique are shown. Second, those obtained from the surface detectors information are explained.

2.3.1 Parameters from the fluorescence technique

The number of particles in the EAS (or shower size) as a function of the atmospheric slant depth (the amount of atmosphere traversed from its upper edge in g/cm^2) is called the shower longitudinal profile. Most of the EAS energy is dissipated through the electromagnetic component. Therefore, the shower size increases until the average energy of the e in the EAS is about the critical energy of 81 MeV, when the rate of energy loss due to collisions and ionization begins to exceed that due to radiation. Photons have a similar attenuation length due to pair production. The slant depth at which the longitudinal profile of a shower reaches its maximum is called X_{max} and is one of the primary observables of the

fluorescence detector.

X_{max} and RMS(X_{max})

Fluorescence telescopes detect the fluorescence light emitted by Nitrogen molecules excited by the passage of an EAS. Most of the fluorescence light is emitted in the near ultraviolet, between 300 and 400 nm. Oxygen molecules do not emit a significant amount of fluorescence light in this range. The amount of fluorescence light emitted is proportional to the energy lost by the electromagnetic shower particles. The proportionality constant is called the fluorescence yield, which is measured by different experiments in the wavelength bands of interest for EAS experiments (Nagano M., 2004), (Ave M. for the Airfly Collaboration, 2007). The excited Nitrogen molecules rapidly de-excite such that the fluorescence light is emitted very close to the actual shower particles. The fluorescence light is emitted isotropically. The longitudinal profile is the number of particles of a shower as a function of the amount of matter crossed, and it is observed with the fluorescence telescopes. In order to measure the total thickness of air crossed by the shower, the atmospheric slant depth is used. The atmospheric slant depth at a given height z measured from the ground level, depends on the shower geometry and on the atmosphere density $\rho(z)$:

$$X(z) = \int_{z}^{\infty} \rho(z^{'}) \frac{dz^{'}}{cos\theta} \tag{2.16}$$

where θ is the zenith angle and the density dependence on the altitude is parametrized using atmospheric models. The general shape of the longitudinal profile is shown in Figure 2.7.

It grows up while the energy of the particles is high enough to produce more particles, it reaches a maximum and later decreases because the energy of the particles is too low to generate more and they are absorbed mainly by ionization. The longitudinal profile may be adequately parametrized by the Gaisser-Hillas function (Gaisser T. and Hillas A. M., 1977):

$$N(X) = N_{max}\Big(\frac{X - X_0}{X_{max} - X_0}\Big)^{\frac{X_{max}-X_0}{\lambda}} exp\Big(\frac{X_{max} - X_0}{\lambda}\Big) \tag{2.17}$$

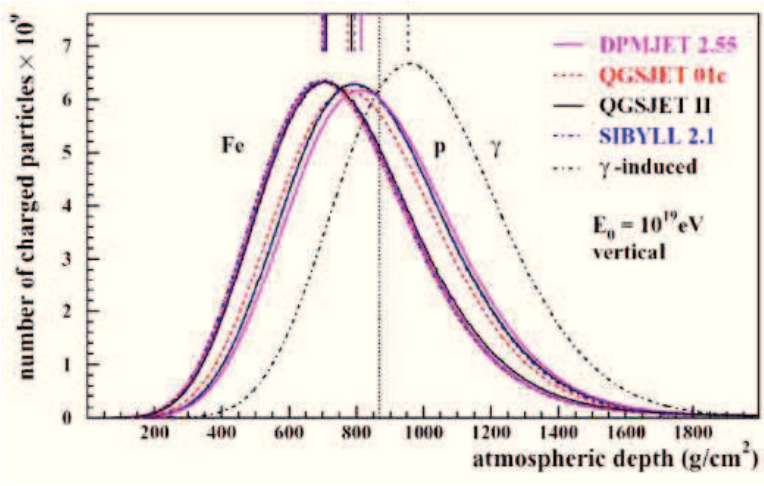

Figure 2.7: Simulated longitudinal profiles for proton, Iron and photon primaries with an initial energy of 10^{19} eV and arriving at a zenith angle $\theta = 0°$.

where $N(X)$ is the number of the shower charged particles (mainly electrons/positrons) at an atmospheric depth X, X_{max} is the atmospheric depth at which the number of particles of the shower reaches its maximum N_{max} , X_0 is the depth corresponding to the first interaction of the primary particle in the atmosphere and λ is the interaction length. $X_{max} - X_0$ depends on the energy and the nature of the primary and it is an indicator of the stage of evolution usually called the age of the shower. X_{max} increases logarithmically with energy: $X_{max} \simeq X_i + 55 \cdot log_{10}(E)\ gcm^{-2}$, where the value of X_i depends on the nature of the primary (an average value is 700 gcm^{-2}) (Abraham J., 2008). In practice, at a given energy, $X_{max}(Fe) - X_{max}(p) \simeq 100\ gcm^{-2}$. This is the essential feature allowing a discrimination between protons, light and heavy nuclei. In our energy range, X_{max} is of the order of 700 to 800 gcm^{-2}, that is less than the total vertical thickness of the atmosphere[1]. Then, at any zenith angle, the maximum of the shower is above the ground. Proton induced showers will have, on average, deeper X_{max} with larger fluctuations, with respect to iron primaries. The X_{max} can be measured directly by the FD looking at the longitudinal energy deposit profile on an event-by-event basis. The statistics is however limited at the highest

[1]atmospheric depth at sea level is around 1030 gcm^{-2}.

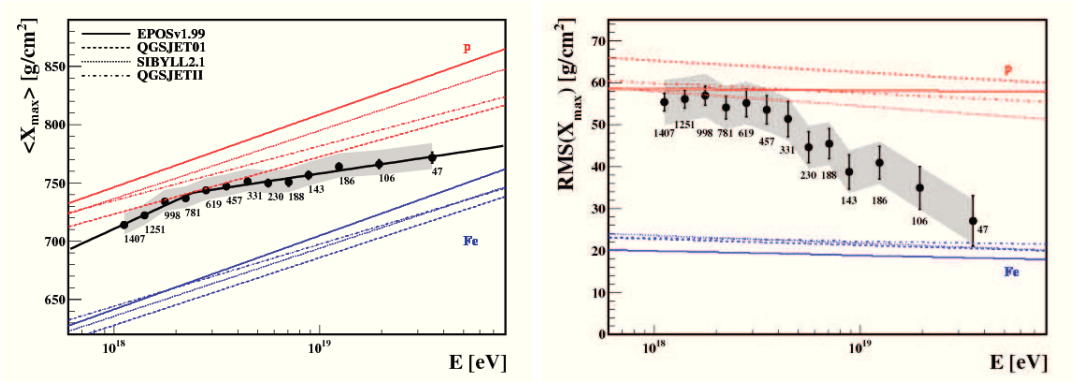

(a) (b)

Figure 2.8: (a): $< X_{max} >$ as a function of energy, compared with the predictions of air shower simulations using different hadronic interaction models. **(b):** $RMS(X_{max})$ as a function of energy, compared with the predictions of air shower simulations using different hadronic interaction models.

energies. The trend of X_{max} as a function of energy is called the elongation rate, as it is a very useful tool to study the composition of UHECRs. The average of the Xmax distribution as a function of energy measured by the FD, $< X_{max} >$, and the $RMS(X_{max})$ (Facal P. for the PAO Collaboration, 2011), are shown in Figure 2.8. The depth of shower maximum depends on the hadronic interactions that rule the shower development. Therefore, the predictions of different hadronic interaction models for these observables are shown, both for proton and iron induced showers. One can observe that there is a trend towards a heavier composition at the highest energies, even though the analysis of $< X_{max} >$ and $RMS(X_{max})$ suggests a complex mass composition scenario (Kampert K.H., 2013).

2.3.2 Parameters from the surface detectors

Surface detectors make a discrete sampling of the shower front at ground level, so that the main SD observables are related to the temporal and spatial distribution of particles. These are the signal risetime in the Cherenkov stations, the curvature of the shower front, the muon content, and the azimuthal signal asymmetry.

Risetime and curvature depend mainly on the depth of the shower development in the atmosphere, and thus on primary energy and mass. The muon content of a shower depends on the primary energy and the number of nucleons, while asymmetry about the shower core is due to geometric effects and attenuation, which are dependent on the primary mass.

Muon content

Most shower muons are the decay product of charged pions. Since they are charged leptonic massive particles theyll lose energy mainly through ionization allowing them to travel large distances while conserving most of their energy. Along with neutrinos, which rarely interact, muons constitute the penetrating component of the air shower reaching several meters underground. Few of them, the least energetic ones, decay into electrons and electron and muon neutrinos. Although there are still few studies about the development of the muonic component, it is expected that muons may play an important role on determining both the primary energy and composition. Muons may act as well as the best messengers of the hadronic shower development while helping to constrain the high energy hadronic models used on the Monte Carlo simulations of EAS. The muon number is the most promising parameter, essentially because the differences between iron and proton are predicted to be very significant. To evaluate quantitatively the relative difference in the muon production in heavy nucleus showers vs. protons showers, first note that the muon production in proton showers increases with energy as $E^{0.85}$ (Gaisser T. K., 1990). Considering a nucleus initiated shower of energy E as a superposition of A showers, each with energy E/A, the total number of muons is $N_\mu \approx A(E/A)^{0.85}$, or comparing to proton showers $N_\mu^A = A^{0.15} N_\mu^p$. Thus, it is expected that an iron shower (A=56) will produce about 80% more muons than a proton shower of the same energy. The muon content is easily determined from scintillators buried at ground or covered with a shield, so that absorbs the electromagnetic component is absorbed. However, it is not straightforward but not from water Cherenkov tanks which, additionally, are very sensitive to the photon component of the shower. Therefore, for the latter is more common to use the muon to electromagnetic ratio (Castellina A. and Navarra G., 2007) because both components are measured efficiently by

these detectors. However, several methods are now being tested (Billoir P. and Gouteraux B., 2006) to determine directly the number of muons too. AMIGA is designed to measure accurately the muon content of the EAS. In (Chou A., 2005) it is showed that most of the SD mass sensitive parameters depend strongly on X_{max} and N_μ.

The risetime of the signal

The signals in the 10 m^2 water Cherenkov detectors are characterised by $t_{1/2}$ (risetime of the signal), the time to rise from 10 to 50% of the integrated signal. The signals, up to 3 μs long, are recorded with a 25 ns FADC system. The spread of the arrival time of the shower particles at a fixed core distance increases for smaller production heights, so the rise time is expected to be smaller for heavy primaries that develop higher in the atmosphere. This is the geometrical reason that relates the rise time with the stage of the shower development, and hence, with X_{max}. For non vertical showers a slight dependence of the rise time on the internal azimuth angle of the stations within the shower plane is expected. The internal azimuth angle is defined as the clockwise angle between the projection of the shower axis on the ground and the line connecting the shower core and the station. The reason is that the shower has to traverses more atmosphere to reach the stations on the exterior side (or late part) of the shower compared to those on the interior side (or early part) of it. Thus, the observed rise time of each station is corrected depending on its internal azimuth angle and the zenith angle of the shower (Abraham J., 2008). The rise time at a fix distance from the shower axis (usually $r_0 = 1000$m), $t_{1/2}(r_0)$, is finally obtained by fitting the corrected rise time of each triggered station using the function $t_{1/2}(r) = (40 + ar + br^2)$ ns. Parameters a and b are free in the fit, and the function is anchored at 40 ns at $r = 0$ because this is the mean single particle response in the water Cherenkov detectors. Only stations in the range from 600 to 1500 m from the shower axis and signal greater than 10 VEM (Vertical Equivalent Muon, i.e. the signal deposited by one vertical muon in an Auger water tank) are included in the fit in order to avoid signals dominated by large fluctuations. At least three stations are needed in the fit. Great advance has been performed in the study of rise time. First, trace cleaning in FADC traces is applied. The water-Cherenkov tanks used in

the surface array are susceptible to the unavoidable background noise produced by isolated low energy cosmic rays. These can cause peaks in the FADC trace which are not deposited energy associated with the EAS. Trace cleaning is the term applied to the process of identifying and removing these parts of the signal. Tanks far from the shower core, and therefore with smaller signal sizes, are most susceptible to these background effects. Second, a deconvolution algorithm is performed. The time structure of the signal recorded when particles are detected in surface tanks is artificially lengthened due to detector effects. This is a consequence of the physical size of the tanks and the bandwidth limitations of the electronics which is corrected by the deconvolution algorithm. Some improvements have been also done in the asymmetry correction explained before and in order to consider temperature and pressure effects (Smith B., 2008). Currently, the tendency is try to measure X_{max} indirectly from water Cherenkov detectors, via the rise time (Watson A.A., 2006), (Smith B., 2007). The method consists on determining the average value of the rise time as a function of the core distance (r) and the zenith angle (θ) for a given reference energy (10^{19} eV), the so called *bench mark*. Then, for each selected detector in a given event, the deviation of the measured rise time from the benchmark function is calculated in units of measurement uncertainty and averaged for all detectors in the event as shown in Eq.2.18 and Figure 2.9, enabling a new observable, $< \Delta_i >$ to be introduced,

$$< \Delta_i >= \frac{1}{N} \sum_{i=1}^{N} \frac{t^i_{1/2} - t_{1/2}(r, \theta, E_{ref})}{\sigma^i_{1/2}(\theta, r, S)} \tag{2.18}$$

Lateral development

Whatever the physical process during the cascade development, the products generated have, in general, a moderate transverse momentum regardless their energy. Then, most high energy particles are colimated along the initial axis, constituting the *core* of the shower. The lateral extension of the core depends on the mean free path, so that it is proportional to the inverse of the density. It may be expressed in terms of the Moliere radius r_M , such that 90% of the energy is contained within a distance from the shower axis $r < r_M$ (in atmospheric showers $r_M \simeq 60 - 100\ m$). However, low energy photons and electrons, as well as muons, extend far away from core, constituting the *halo* which has a detectable

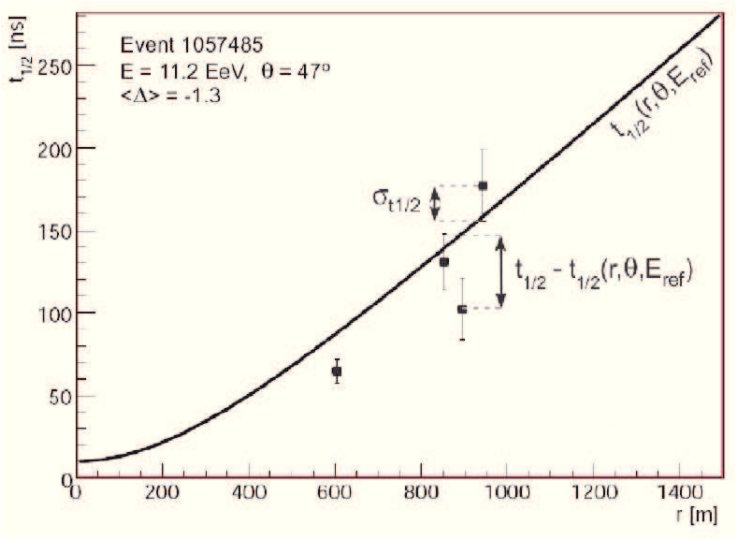

Figure 2.9: Rise time vs distance to the core. The curve is the benchmark rise time and the data points represent the measurements of rise time of each detector with uncertainties for this particular event (Wahlberg H., 2009).

density up to a few kilometers from the axis depending on the primary energy. The electromagnetic part of the halo increases with the depth, reaching its maximum at around $X_{max} + 100 g/cm^2$ and then decreasing rapidly (it is completely extinguished at $X_{max} + 1000 g/cm^2$). Most muons travel beyond the electromagnetic cascade, giving a *muonic tail*, with an increasing spread with core distance due to a simple straightforward propagation. After a long range, lower energy muons (with larger divergence) decay. Independently of the electromagnetic cascade, the muons generate an *electromagnetic tail* through their decay, $\delta - ray$ production and radiative processes (bremsstrahlung and pair production) which are important above few tens of GeV. $\delta - ray$ production is characterized by very fast electrons produced by energetic charged particles as the muons, knocking orbiting electrons out of atoms. Collectively, these electrons are defined as delta radiation when they have sufficient energy to ionize further atoms through subsequent interactions on their own. For high energetic events, the electromagnetic component dominates the region near the shower axis and the muonic component is more important in the far region. The density of particles for vertical showers with energies of 10 EeV and for different primaries is shown in Figure 2.10.

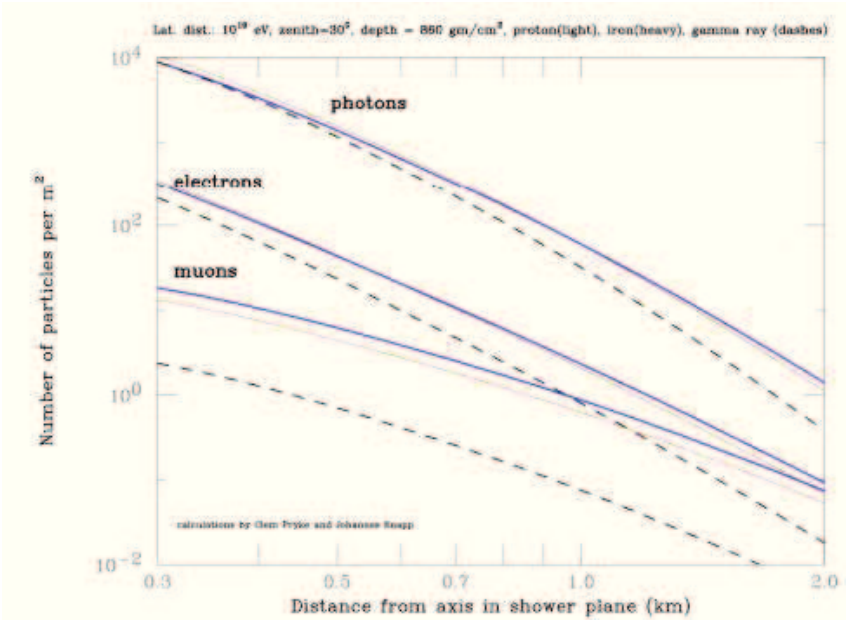

Figure 2.10: Simulation of the lateral distribution of shower particles. Curves are obtained averaging on many showers. The photon, electron and muon densities in the plane perpendicular to the shower axis are shown for shower induced by protons (red line), Iron nuclei (blue line) and gamma rays (dashed line) of energy 10^{19} eV.

The surface detector only samples the shower front of the air showers. The total number of particles reaching the ground has to be inferred by fitting the individual sampled densities to an assumed lateral distribution function. As the lateral distribution of particles is mainly determined by Coulomb scattering of the dominant electromagnetic component, it can be approximated by the Nishimura-Kamata-Greisen (NKG) function (Greisen K. , 1956), (Kamata K. and Nishimura J., 1958):

$$\rho(r) = \left(\frac{r}{r_M}\right)^{\beta}\left(1+\frac{r}{r_M}\right)^{-(\beta-\gamma)} \tag{2.19}$$

where β and γ are parameters determined experimentally and k is proportional to the shower size. Many other functions have been used instead of the NKG one (see for example (Pierre Auger Collaboration, 2005)). The lateral distribution is subject to fluctuations, from the detector response itself and from shower-to-shower. In addition, uncertainties in core location would significantly modify the

integral of this function and the signal measurements are poor at distances lower to the Moliere radius because the array size is usually larger and/or the detectors may saturate. Therefore, a procedure similar as the one used in the fluorescence technique may introduce huge uncertainties. Instead, Hillas proposed to use the density at a certain distance from the shower axis where these uncertainties minimized (Hillas A. M., 1970). In surface experiments, a transformation from the signal at this distance into the energy is usually done by Monte-Carlo (MC) air shower simulations. Unfortunately, the lateral distribution of particles obtained from simulations does not describe perfectly the data (Apel W. D., 2004), (Antoni T., 2001) and MC are based on hadronic interaction models that introduce important uncertainties.

Chapter 3

The Pierre Auger Observatory

The Pierre Auger Observatory (PAO) is an international observatory designed to detect ultra-high-energy cosmic rays (UHECRs): single sub-atomic particles (protons or atomic nuclei) with energies beyond 10^{18} eV. The PAO covers a wide area of $\sim$3000 km^2. Due to the rate of events in this energy range, which can be as low as 1 $particle/km^2 centuty$ the use of such large area is the only way to collect a high enough statistics in a reasonable time. It is built in the Argentinian Pampa Amarilla, near the small town of Malargue (35.2° latitude S, 69.5° longitude W) in the Department of Mendoza, in an uplands at an altitude between 1300 m and 1500 m above sea level. This corresponds to a vertical atmospheric depth of about 870 gcm^2, which is close to the depth of maximum development of the showers in this energy range. In order to match the shower footprint at ground, 1660 surface detectors (SD) are placed an a triangular grid, at mutual separation of 1.5 km. The longitudinal development of the EAS in atmoshere is measured by means of 24 fluorescence detectors (FD), hosted in 4 buildings overlooking the surface array. The PAO is a "hybrid detector", it measures EAS with complementary techniques thus performing cross-checks on the different observables by means of distinct techniques with different systematic uncertainties. In Figure 3.1 the layout is shown. The dots show the positions of the SDs, the green lines define the fields of view of the FDs.

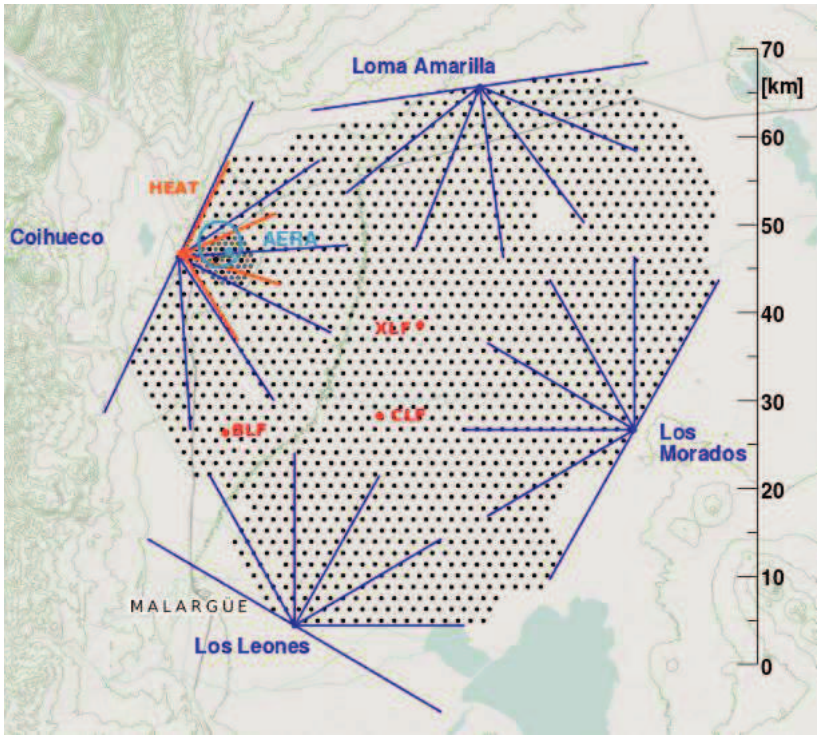

Figure 3.1: Layout of the Pierre Auger Observatory. The blue shaded area shows where detectors are already installed. The dots mark the positions of the surface detectors while the blue lines define the fields of view for the fluorescence telescopes.

3.1 The Surface Detector

The SD array of the PAO consists of 1660 water Cherenkov detectors, covering ∼3000 km^2 with a spacing of 1500 m on a triangular grid. A schematic view of a surface detector station is shown in Figure 3.2.

Each station is a polyethylene plastic tank of 10 m^2 area and 1.2 m height, hosting 12000 l of ultra purified water contained in a Tyvek reflective liner, which allows for a uniform reflection of the Cherenkov light generated by charged particles of the shower crossing the tank at a speed greater than the speed of light. This light is registered by three 9" Photonis XP1805 photomultiplier tubes. The signal is extracted both from the anode and the last dynode, the latter being amplified by nominal factor of 32. In this way, we obtain a wide dynamic range extending from a few to about 10^5 photoelectrons. The station electronics is made up of

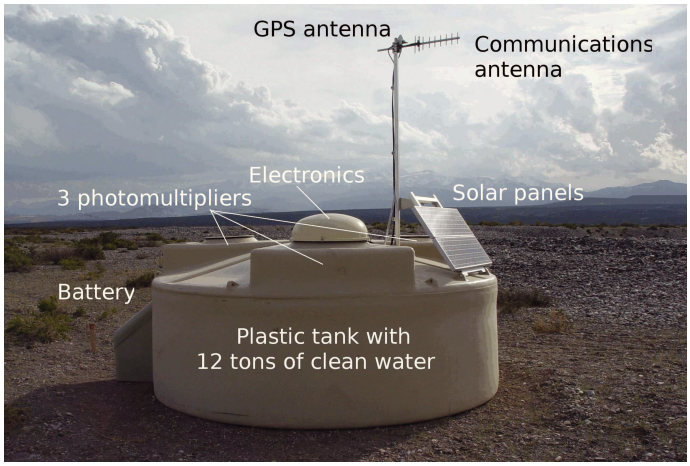

Figure 3.2: Schematic view of a surface detector station.

the front-end electronics (FE), a station controller composed of a microprocessor performing local software processing, a slow control module, a GPS receiver and a time tagging unit. On the FE-board, the PMT signals are filtered and digitized at 40 MHz using a 10-bit ADC: the signal recorded by the FADC is referred to in units of channels (ch), with a range of 0-1023, corresponding to an input range of 0-2 V. Each FADC bin corresponds to 25 ns. A programable logic device (PLD) is used to read the channels. Each detector operates autonomously with its own front-end electronics and communication system, while a solar energy unit and batteries provide the required 10 W electrical power. The timing is obtained by a GPS unit and the communications achieved via a wireless system. The GPS signal is used to syncronize a 100 MHz clock used to time-tag the trigger. A local PC microcontroller is used for local data acquisition. The SD can operate continuously, with a duty cycle of almost 100%.

3.1.1 Surface Detector Calibration

The calibration is designed to establish the signal sizes in each station, to set the high voltages of the PMTs, to give the amplification factor of the anode with respect to the last dynode and to set the trigger levels. The signal produced in a station depends on variable parameters like water quality, liner reflectivity, the

coupling of the PMT to the water, the gain of the PMT, the gain of the last dynode, the electronic gain of dynode and anode amplifiers. Thus the calibration has to be independent on the number of PMTs functioning and on differences from station to station. The basic physics calibration information needed by the SD is the average charge produced by a vertical and centrally through-going muon (Bertou X., 2006). The conversion to this unit, the vertical equivalent muon (VEM), is done to provide a common reference level between tanks. Therefore the calibration goal is to obtain the value of 1 VEM in electronic units for each individual station. The surface detector in its normal configuration cannot distinguish the vertical from the inclined atmospheric muons passing constantly through. However the distribution of light from atmospheric isotropic muons produces a peak which has to be related to the VEM. The sum of the PMTs is a measure of the total signal deposited in the tank, whereas the individual PMTs are sensitive only to a fraction of the signal, deposited in the proximity. Thus this peak is at ≈ 1.09 VEM for the first case and ≈ 1.03 VEM for individual PMTs. These values were measured in a reference tank (Aglietta M. for the PAO Collaboration, 2005), a special setup consisting of a station equipped with two centered scintillators, one on top and the other underneath the station, the trigger requiring coincidences within the two scintillators (see the charge and pulse height histogram in Figure 3.3). The calibration to VEM units includes three main steps and is done only on the peak produced by the omnidirectional muons:

- **The PMTs gains set up**: the PMTs voltage is set at the deployment time and it determines the dynamic range of each PMT. Each PMT can be recalibrated on request from the Central Data Aquisition System (CDAS). The initial value is chosen in such a way that a single vertical muon produces a peak of about 50 FADC counts, meaning a gain of 3.5×10^5 for 94 photoelectrons per VEM per muon. The gains of the three PMTs are set up by matching a point in the event distribution to a measured rate from the reference tank. The latter is calibrated by obtaining a charge histogram and adjusting the three PMTs until the peak of the histograms agree. The

gains of the PMTs are set such that the single rates at 150 channels above baseline are 100 Hz.

- **The online local calibration**: to maintain a uniform trigger condition of the array, the station must be able to get to a common trigger threshold. Therefore the online calibration has to compensate for possible drifts in the gain of the PMT. This allows a tank independent analysis of the array response. The trigger levels are set on a minute by minute basis and compensate the drifts of the peak for each detector. Detectors which have drifted significantly (>20 ch) from the nominal value of I_{VEM}^{peak} of 50 ch are reinizialized. For each station some quantities (charge for each PMT and for the sum of all 3 PMTs, pulse height for each PMT and baseline of each FADC channel) are collected every minute, stored in histograms and sent to the CDAS. During data analysis, the second peak of individual charge histogram is used to obtain the value of Q_{VEM} necessary to convert the integrated signals into units of VEM.

- **Dynode to anode ratio**: large shower signals are measured on the anode channel, when the dynode channel is saturated. However, the absolute energy scale using muons is determined from the dynode channel, as single muon signal on the anode is too small to be useful for calibration. Consequently, the relative gain between these two channels must be measured. One way to measure this relative gain is from moderately large signals of 20 to 50 VEM. These signals do not saturate the dynode channel, and at the same time they are well above the noise level on the anode channel. Comparing the signal in this overlap region allows us to extract the relative gain of the two channels.

3.1.2 SD Triggers

The trigger SD is composed of different subsets of trigger with a hierarchical structure. In general, there are two levels of local trigger (T1 and T2) and one central trigger (T3). Two more triggers (T4 and T5) are used to select physical

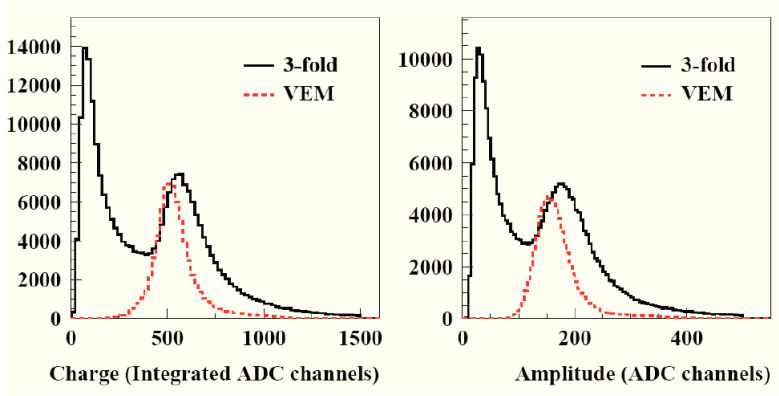

Figure 3.3: Charge and pulse height histograms from an SD station, triggered by a 3-fold coincidence between all 3 PMTs at a trigger level of 5 channels above baseline, with the signal from all PMTs summed. The dashed histogram is produced by an external muon telescope providing the trigger to select only vertical and central muons. The first peak in the black histogram is caused by the convolution of the trigger on a steeply falling distribution from low-energy particles. The second peak is due to vertical through-going atmospheric muons.

events at software level.

Local triggers (T1 - T2)

The T1 trigger, evaluated by the PLD (Programmable Logical Device), is used to find signals in a single station that could be part of an EAS. It includes: a threshold trigger (Thr) and a Time over Threshold trigger (ToT). In the Thr trigger, a coincidence between the signals from the three PMT of the tank above the threshold of 1.75 VEM is looked for. Its rate is about 100 Hz. The ToT trigger requires at least 13 bins in a 120 bin interval above a threshold of 0.2 I_{VEM} (pulse height) in coincidence with at least two of the tank's PMTs. Its rate is about 1.6 Hz. The second level trigger (T2) is processed by the local software. All triggers, and all threshold triggers above 3.2 VEM, are designated as T2. The local station controller provides the T2 trigger decision as well as the handling of the GPS timing board, of the slow control board and of the forwarding of T2 triggers to CDAS. The rate of T2 triggers is around 20 Hz.

Central trigger (T3)

It is used to find time coincidences among stations that can be associated to a real shower. It considers any of the following requests:

- a 3-fold condition, which requires a coincidence within a time interval depending on the distance of three tanks passing the ToT condition.
- a 4-fold coincidence which requires the coincidence within a time window depending on the tank distance among 4 tanks having passed any T2 condition, with 2 tanks inside 2 hexagonal crowns from a triggered tank and a further one within 4 crowns. A crown is formed by the stations at equal distance from the center one and are numbered depending on this separation.
- a 3-fold condition which requires the coincidence of three aligned tanks passing any T2 condition.
- an external condition generated by the fluorescence detector (FD).

The third level trigger drastically reduces the rate of events considered good ($\backsimeq$ 0.01 Hz). Any time T3 trigger is issued, all the stations of the array are requested to send their data if in coincidence with the central station.

Physical trigger (T4 - T5)

The first physics trigger (T4) was designed to distinguish air showers from random coincidences of single atmospheric muons and is also the first step to select reconstructible vertical events. It consists of:

- 3ToT trigger, which requires at least 3 stations with a ToT trigger in a non-aligned configuration. This simple compact trigger is not effective for events with large zenith angles due to the dominance in this case of the muonic component which gives origin to fast less spread signals. This requirement selects 99% of the events with zenith angle less than 60°.
- 4C1 trigger, which is passed only by events that have 4 tanks with a T2 trigger each, and a configuration of one station with 3 close neighbors.

In all cases of the T4 trigger, compatibility in time between stations part of the trigger is required. The difference in their start time has to be lower than the distance between them divided by the speed of light, allowing for a marginal limit of 200 ns.
The quality trigger (T5) is meant to exclude events that fall too close to the edge of the SD array. For this class of events, due to a possible missing signal, the reconstruction of the air shower variables may not be reliable. Another reason is that it is very hard to compute the acceptance which would take into account events that are highly energetic but far away from the array. In such cases the trigger probability for 4 tanks on the edge of the array depends on fluctuations which are very hard to simulate. This quality trigger is based on a criterion related to the core position: for the station with the largest signal it is required to have six nearest neighbors that were present and functioning (but not necessarily triggered) atthe time of the shower impact. This assures a good and unbiased reconstruction of the event.

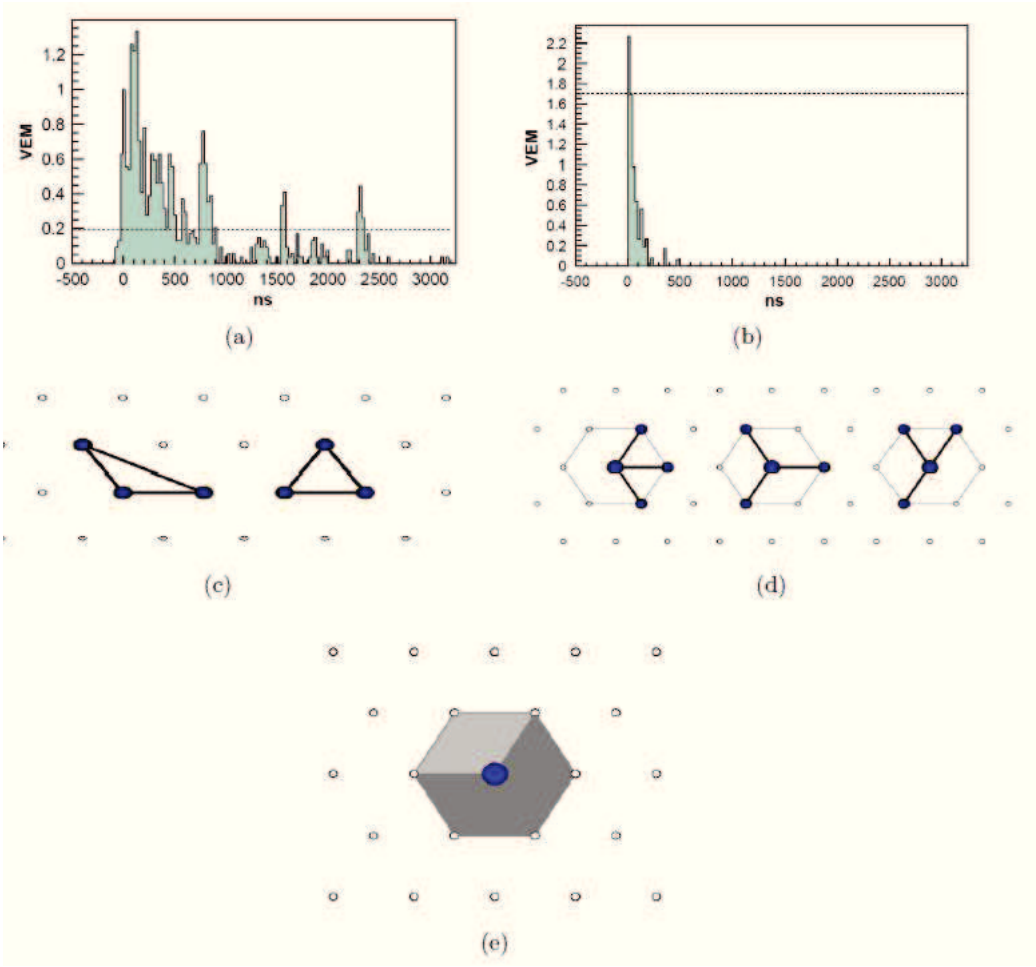

Figure 3.4: The SD trigger schema. 4.4(a): The first operation mode of the T1 trigger, requiring a 2-fold PMT coincidence with 13 bins in 120 bins window above 0.2 VEM. An example of a PMT trace is shown together with the 0.2 VEM threshold; 4.4(b): The second operation mode of the T1 trigger, requiring a 3-fold PMT coincidence in a single bin above 1.75 VEM. An example of a PMT trace is shown together with the 1.75 VEM threshold; 4.4(c): Two possible 3ToT compact configurations; 4.4(d): The three (minimal) 4C1 configurations; 4.4(e): The T5 configuration: the central station with the largest signal is surrounded by 6 functioning stations.

3.2 The Fluorescence Detector

The detection of ultra-high energy cosmic rays using nitrogen fluorescence emission induced by extensive air showers is a well established technique, used previously by the Fly's Eye and HiRes experiments (Sokolsky P., 2008). It is used also for the Telescope Array project (Kawai H., 2008), and it has been proposed for the satellite-based EUSO projects (Takahashi Y. for JEM-EUSO Collaboration, 2009). Charged particles generated during the development of extensive air showers excite atmospheric nitrogen molecules, which then emit fluorescence light in the $\backsim$ 300 - 430 nm range. The number of emitted fluorescence photons is proportional to the energy deposited in the atmosphere. By measuring the rate of fluorescence emission as a function of atmospheric slant depth **X**, an air fluorescence detector measures the *longitudinal development profile* $\frac{dE}{dX}(X)$ of the air shower. The integral of this profile gives the total energy dissipated electromagnetically, which is approximately 90% of the total energy of the primary cosmic ray. Of the remaining 10% about 90% are muons and the rest consists of hadrons. For any waveband, the fluorescence yield is defined as the number of photons emitted in that band per unit of energy loss by charged particles. The absolute fluorescence yield in air at 293 K and 1013 hPa from the 337 nm fluorescence band is 5.05 ± 0.71 photons/MeV of energy deposited, as measured in AIRFLY (Privitera P., 2005). The wavelength dependence of the yield has been described e.g. in (Ave M., 2007a). Since a typical cosmic ray shower spans over 10 km in altitude, it is important to stress that due to collisional quenching effects the fluorescence yield is also dependent on pressure, temperature and humidity of the air.

As opposed to the SD array, the FD may only operate during clear, moonless nights and its duty cycle is thus reduced to about 14%. Since the fluorescence emission, as well as the light scattering and attenuation, depends on atmospheric conditions, several systems monitor the weather conditions, the aerosol content and the cloud coverage. The fluorescence detector (FD) comprises four observation sites - Los Leones, Los Morados, Loma Amarilla, and Coihueco - located an small elevations on the perimeter of the SD array (Figure 3.5).

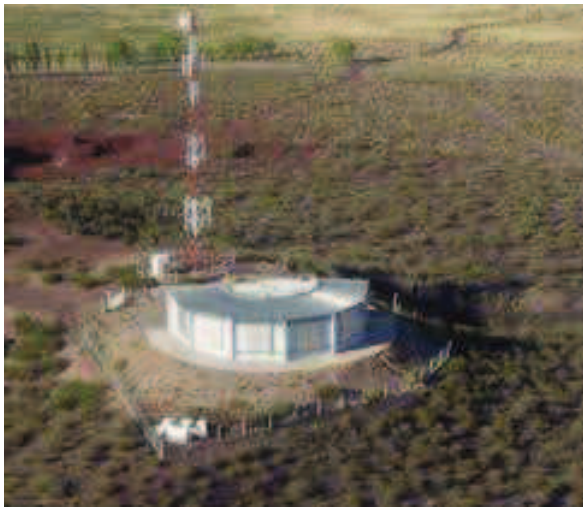

Figure 3.5: Aerial view of the fluorescence detector site Los Leones.

Six independent telescopes, each with field of view of 30° × 30°, are located in each FD site. The telescopes face towards the interior of the array so that the combination of the six telescopes provides 180° coverage in azimuth (Abraham J., 2009). Figure 3.6 shows the arrangement of the telescopes inside an observation site.

Figure 3.7 depicts an individual FD telescope. The telescope is housed in a clean climate-controlled building. Nitrogen fluorescence light enters through a large UV-passing filter window of $3.8m^2$ aperture and a Schmidt optics corrector ring. The light is focused by a $12m^2$ mirror with a curvature radius 3.4 m, onto a camera of 440 photomultipliers (Photonis XP 3062). Light pulses in the pixels are digitized every 100 nanoseconds and a hierarchy of trigger levels culminates in the detection and recording of cosmic ray air showers.

3.2.1 Fluorescence Detector Calibration

Necessary conditions for a precise measurement of the cosmic ray energy longitudinal distribution are: the knowledge of the FY (Fluorescence Yield), the telescope calibration and the atmospheric monitoring. While the first one is taken from a different experiment (Arciprete F., 2006), the end-to-end FD absolute calibration is performed using an absolutely calibrated light source providing light

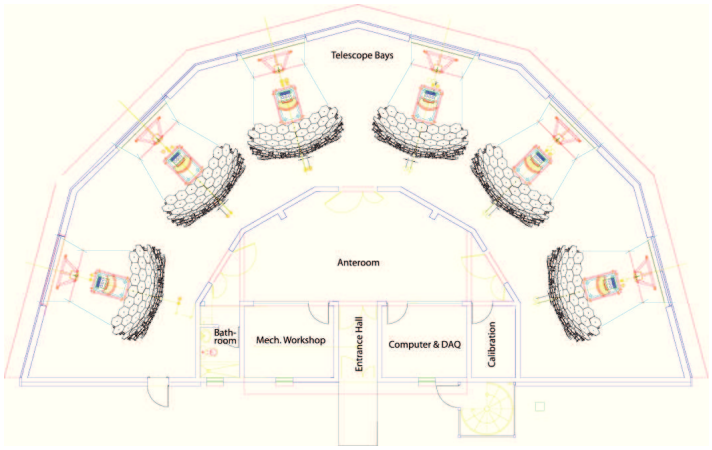

Figure 3.6: Schematic layout of the building with six fluorescence telescopes.

Figure 3.7: Individual FD telescope.

of the same wavelength and distribution as it is measured in cosmic ray showers. The light source injects uniformly distributed photons on the telescope aperture for any given direction with wavelengths between 300 and 400 nm. The absolute calibration is performed 3-4 times/yr and has currently an uncertainty of $\sim$ 12%. A relative calibration monitors the detector response and possible changes. It runs before and after each night of operation (Knapik R., 2007). The atmospheric monitoring is used to measure and parametrize the attenuation lenght due to Rayleigh and Mie scattering of the fluorescence light.

3.2.2 FD Trigger

The fluorescence detectors have a trigger organized at several levels:

- The first level trigger selects pixels with signal above a given threshold. It is continuously adjusted in such a way that the rate of events remains constant $\sim$100 Hz and independently of external conditions (e.g. greater illumination due to the presence of the Moon, or stars in the field of view of the pixel).

- The second level trigger is used to search for patterns consistent with a track segment, and to generate an internal trigger for data readout. It looks for a geometrical pattern of 4-5 pixels overlapping within 32 μsec and has a rate of $\sim$ 0.1 Hz/mirror.

- The third level trigger is a software algorithm optimized for the fast rejection of triggers caused by lightning, by muon impacting on the camera, and randomly triggered pixels. The rate lowers to 0.02 Hz/mirror.

- Surviving events are sent to the local DAQ. An event builder running on the eye PC merges coincident events from adjacent telescopes and a fourth level trigger T3 is used to calculate a preliminary shower direction and ground impact time with a simple online reconstruction. Once these data arrive at the central data acquisition, a request is sent to the SD for signals recorded close to the calculated impact time. For each T3 trigger, the SD stations nearest the FD building are read out co collect possible hybrid events.

3.3 The low-energy enhancements of the Pierre Auger Observatory: HEAT and AMIGA

In order to study the transition region where the onset of the extragalactic cosmic rays is appearing, the PAO Collaboration proposed in 2006 to build detector enhancements. With these enhancements, the PAO will provide full efficiency detection of cosmic rays down to 10^{17} eV and a direct measurement of the muonic component of the extensive air showers.
The first of these enhancements is given by HEAT (High Elevation Auger Telescopes). They extend the energy range of the regular FD to energies between 10^{17} eV and $10^{18.5}$ eV. An extensive air shower initiated by a primary particle with an energy lower than 10^{18} eV emits less fluorescence light than showers with higher energy. Therefore, such a shower can only be detected if it is close to a fluorescence telescope. Showers detected by the fluorescence telescopes will only be used for physics analyses if the reconstructed shower maximum X_{max} is in the field of view of the telescopes. In order to detect the shower maximum of showers close to the telescopes, they must have a field of view that extends to higher elevations. This is realized by the additional field of view of HEAT from 30° to 60° in elevation. Figure 3.9a shows a schematic illustration of the shower detection method by a standard fluorescence telescope in combination with two HEAT telescopes. The shower maximum X_{max} of the indicated shower is seen in the field of view of oneof the HEAT telescopes. A shower with such a geometry would not pass the selection criteria for physics analyses if it was detected by the standard fluorescence telescope only.
HEAT consists of three standard Auger FD telescopes (180 m from Choihueco FD), which can be tilted by 30° upwards (Figure 3.8).

For installation, calibration and also for comparison with data taken by Coihueco, HEAT can be operated in untilted mode as well. Inclination sensors at mirror, camera and aperture box and distance sensors between camera and mirror system are used to monitor the camera position in the optical aperture of the telescopes in a tilted position in order to guarantee the stability of the camera position. For more information on the HEAT design see (Kleifges M. for the PAO Collaboration, 2009). In Figure 3.9b a recorded shower with a similar geometry like

Figure 3.8: Photo of the three HEAT buildings in tilted mode.

that in Figure 3.9a is shown in the event display of two HEAT cameras and one Coihueco camera. The position of the shower maximum lies in the field of view of the telescope 1 of HEAT and, therefore, this shower would not pass the selection criteria for physics analyses without the HEAT measurement.

The second of these enhancements is given by AMIGA (Auger Muons and Infill for the Ground Array). It is the SD complement to HEAT. The AMIGA enhancement of the Auger Surface Detector consists of a 23.5 km^2 infilled area where the shower particles are sampled by 61 pairs of water Cherenkov detectors at mutual distance of 750 m (half of the standard one), accompanied by 30 m^2 of scintillator counters, buried 2.3 m underground. The layer of soil above the muons detectors is used as a shielding against the electromagnetic component of the shower. The modules are placed ∼5 m away from the surface detector to reduce any angular dependence due to a possible "shading" and to avoid the removal of the surface detector to excavate the pits for the muon detector modules.

The muon detectors comprise highly segmented scintillators with optical fibres ending on multi-anode phototubes. The AMIGA complex is centred 6.0 km away from the fluorescence detector installation at Coihueco and is overlooked by the HEAT telescopes (Etchegoyen A., 2007).

As shown in Figure 3.10, the enhancement will allow the complete inclusion of the ankle and the second knee inside the observation range of Auger.

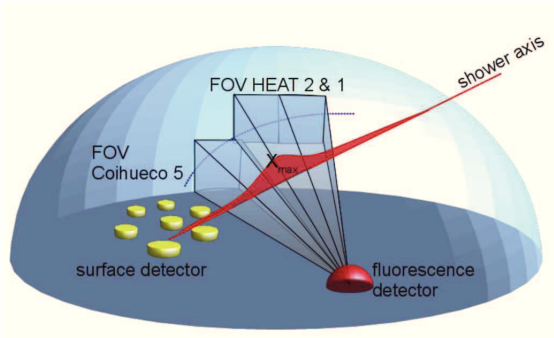

(a)

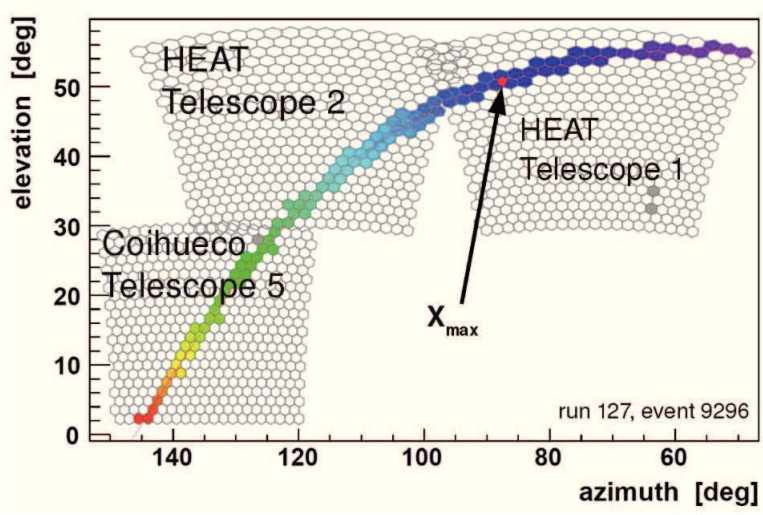

(b)

Figure 3.9: (a): Schematic illustration of the shower detection method by a standard fluorescence telescope in combination with two HEAT telescopes. The field of view (FOV) of a standard fluorescence telescope (Coihueco 5) and two HEAT telescopes (HEAT 2 & 1) are depicted. **(b):** Event display of two HEAT and one Coihueco cameras. The photomultiplier pixels record the fluorescence light of an extensive air shower starting from the upper right corner to the lower left. The position of the shower maximum X_{max} is seen by telescope 1 of HEAT.

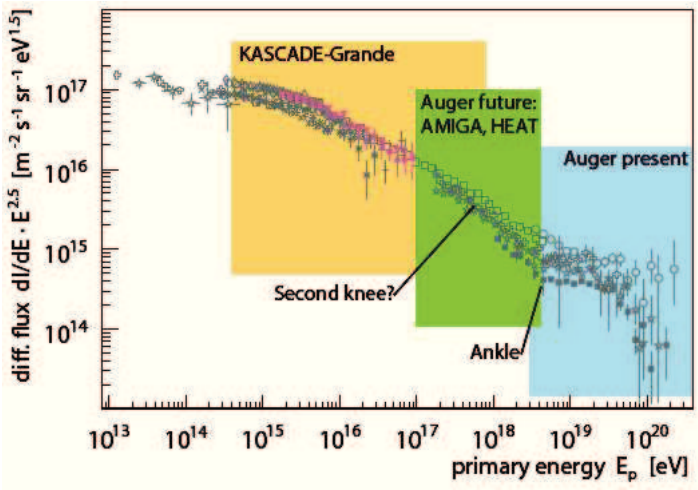

Figure 3.10: Comparison of the energy ranges of the spectrum of primary cosmic rays covered by KASCADE-Grande, the present Auger detector systems and the future Auger enhancements AMIGA and HEAT.

3.4 The muon detector of AMIGA as a tool for composition studies

High energy cosmic rays are indirectly characterized by measuring the extensive air shower cascades that they trigger in the Earth atmosphere. At ground level, and at distances greater than a few tens of meters from the axis, the shower is dominated by just two components: electromagnetic (electrons, positrons and photons) and muonic. The relative weight of these two components can give invaluable information about the nature of the primary cosmic ray and of the high energy hadronic processes taking place at high altitude during the first interactions. Unfortunately Water Cherenkov Detectors used by the Pierre Auger Observatory measure the energy deposition of all charged particles inside their volume and are not well suited for discriminating between electromagnetic and muonic components. Therefore, as part of the Auger surface low energy extension AMIGA (Platino M. for the PAO Collaboration, 2009), buried muon scintillators are added to the regular surface stations of an infill region of the array. Provided enough shielding is ensured, these counters allow the measurement of the muonic component of the particle cascade and, in combination with their Cherenov tank

companions, the estimate of the electromagnetic component. It is therefore of great importance to correctly ascertain the type of primary particle from the recorded shower data. Many different observables can be explored by the PAO to study the primary composition, each of them reflecting the differencies in the interaction of the primary nuclei and in the subsequent cascade propagation. Several parameters obtained from the surface and fluorescence detectors are used for the identification of the primary. The difference between parameters corresponding to different primaries is due to the fact that showers initiated by heavier primaries develop earlier and faster in the atmosphere and also have a larger muon content. For this purpose, some parameters can be employed, for example the position of the shower maximum X_{max}, which is used by most analyses so far, or the interpolated signal strength measured by the surface detectors at 600 m distance from the shower core S_{600}. However, reconstructing the type of the primary particle from different parameters leads to partly conflicting results. The AMIGA muon counters buried deep underground provides an additional possibility to determine the type of the primary particle by measuring the number of muons inside an extensive air shower. From these measurements, the number of muons on ground at a distance of 600 m from the shower core $N_\mu(600)$ can be reconstructed. $N_\mu(600)$ is nearly linearly dependent on energy; therefore, its use as a composition estimator requires, ideally, an independent determination of the shower energy. The simulation results for $N_\mu(600)$ shown in Figure 3.11 suggest that a differentiation between proton and iron primaries is possible (Design Report AMIGA, 2006).

Exploting the measured muon lateral distribution function ρ_μ(r) by the AMIGA counters, the number of muons at 600 m from the core can be obtained for each individual event by fitting the muon lateral distribution function(MLDF) with a modified version of the Greisen function (Buren J., 2005);

$$\rho_\mu(r) = N_\mu\Big(\frac{r}{r_0}\Big)^{-\alpha}\Big(1+\frac{r}{r_0}\Big)^{-\beta}\Big[1+\Big(\frac{r}{10r_0}\Big)\Big]^{-\gamma} \tag{3.1}$$

where r is the distance to the shower axis, N_μ, r_0, α, β, and γ are parameters which define the shape and size of the MLDF. In Figure 3.12, the lateral distribution of muons at 2.5 m underground for showers at three different energies and initiated by either protons or iron nuclei are shown.

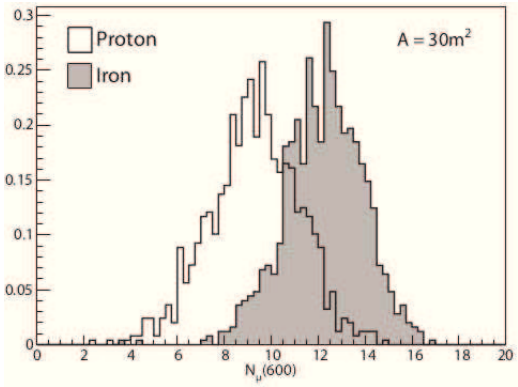

Figure 3.11: Distribution of the simulated and reconstructed number of muons at a distance of 600 m from the shower core for proton and iron primaries and a 30 m^2 muon detector (Design Report AMIGA, 2006).

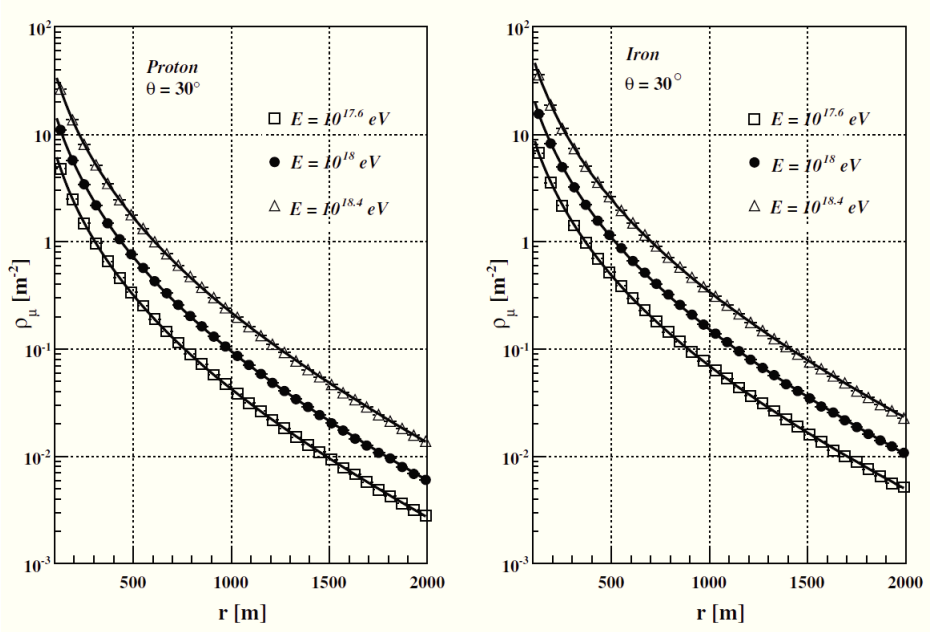

Figure 3.12: Lateral distribution functions of muons at 2.5 m underground for showers initiated by protons and iron nuclei of $\theta = 30°$ and primary energies of $10^{17.6}$, 10^{18}, and $10^{18.4}$ eV. To generate the air showers it was used Aires 2.8.2 with QGSJET-II. The solid lines correspond to fits with the KASCADE-Grande MLDF (Buren J., 2005).

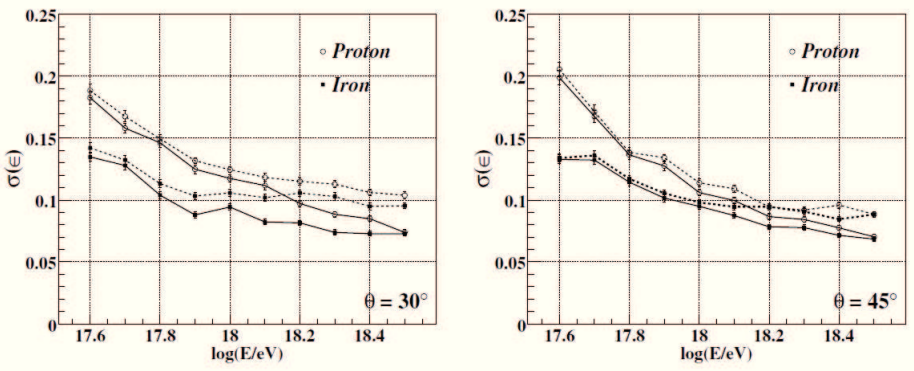

Figure 3.13: Relative error of N_μ^{Rec} as a function of the logarithm of the energy for protons and iron nuclei of N_μ^{Rec} (left panel) and N_μ^{Rec} (right panel). We considered muon detectors of 30 m^2 of area and 192 segments. We assumed a time resolution of 20 ns (solid lines) and a value much greater than the width of the time distribution of muons (dashed lines) which corresponds to the most unfavorable case.

The $N_\mu(600)$ is evaluated with an uncertainty that depends on the statistical fluctuations, the error in the muon counting, the uncertainty in the reconstruction of the lateral distribution. The relative error of $N_\mu(600)$ as a funtion of energy is shown in Figure 3.13, where we define

$$\varepsilon = \frac{N_\mu^{Rec}(600)}{N_\mu^{Real}(600)} - 1 \tag{3.2}$$

where N_μ^{Rec} is the reconstructed number of muons from a MLDF fit and N_μ^{Real} is the expected average number of muons from sampling muons in a 40 m wide ring (in the shower plane), both at 600 m from the shower axis. The relative error decreases with energy, since the muon number is quasi linearly growing with energy and the total uncertainty is dominated by statistical fluctuations. As one can see in the figure (dashed lines), a change in the time resolution from 20 ns to a value greater than the muon time distribution does not cause a change in the relative error within few percent. The uncertainty in the muon number at 600 m from the core is $\lesssim 20\%$ in the energy range of interest and decreases with energy. Since the error in the reconstructed energy is around 20%, this uncertainty is dominating in the definition of N_μ^{Rec} .

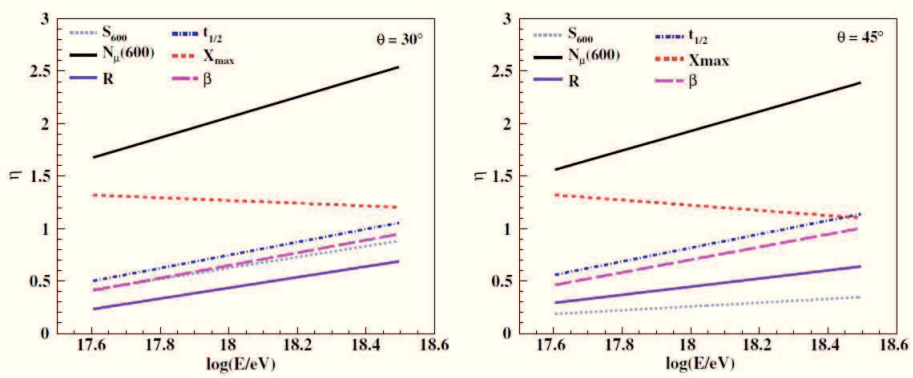

Figure 3.14: Comparison of the discrimination power η as a function of the primary energy for different parameters and showers with zenith angles of 30° and 45° (Supanitsky A.D., 2008).

Besides the muon content of the shower and the depth of the maximum there are other parameters that are used for composition analysis (Supanitsky A.D., 2005). These are the structure of the shower front (in particular the rise-time of the signals in the surface detectors $t_{1/2}$), the radius of curvature R, and the slope β of the lateral distribution function of the total signal deposited in the water Cherenkov detectors S_{600}. To compare the discrimination power of the different parameters considered ($q = N_\mu(600)$, X_{max}, β, R, S_{600}) we define,

$$\eta(q) = \frac{|\langle q_{proton}\rangle| - |\langle q_{Fe}\rangle|}{\sqrt{\sigma^2(q_{proton}) + \sigma^2(q_{Fe})}} \tag{3.3}$$

where $\langle q_{proton}\rangle$ and $\langle q_{Fe}\rangle$ are the mean values of the parameter q for proton and iron primaries and $\sigma(q_{proton})$ and $\sigma(q_{Fe})$ are the standard deviations of these parameters (Supanitsky A.D., 2008). The higher $\eta(q)$, the better q is suited to distinguish between proton and iron primaries.

Figure 3.14 shows the linear fits of η as a function of the logarithm of the energy for $\theta = 30°$ and $\theta = 45°$ and for the different parameters considered. From Figure 3.14 we see that the parameter which better separates protons from iron nuclei appears to be $N_\mu(600)$, followed by X_{max}. We can also see that, except for X_{max}, η increases with the primary energy. This happens because, as the energy increases, the number of triggered stations also increases, which reduces

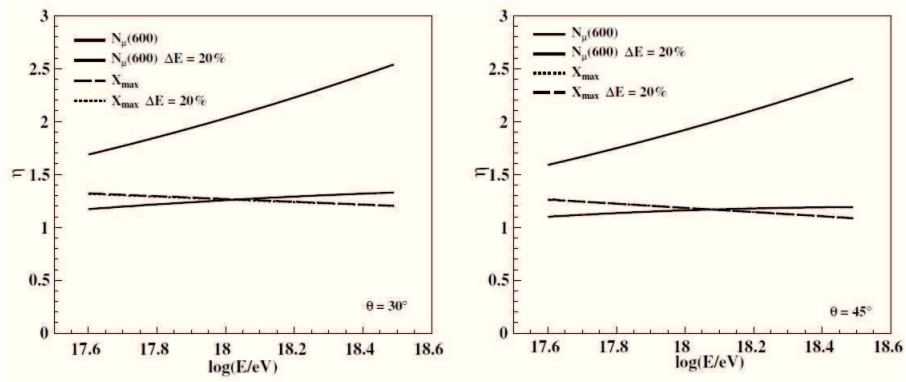

Figure 3.15: η as a function of log(E/eV) for the parameters X_{max} and $N_\mu(600)$ for $\theta = 30°$ and $\theta = 45°$, assuming a power law spectrum of spectral index c = 2.7 and a Gaussian uncertainty of 20% of relative error and without including the effects of the energy uncertainty (Supanitsky A.D., 2008). The differences between the curves corresponding to X_{max} with and without including the energy uncertainty are so small that cannot be seen in both plots.

the reconstruction errors. The number of particles in the detectors also increases with the energy and therefore reduces fluctuations. Although the reconstruction error of X_{max} decreases with primary energy, η slowly decreases. This happens because the mean values of X_{max} corresponding to protons and iron nuclei get closer as the energy increases for the hadronic model considered (however, this is not the case for the hadronic model EPOS, (Unger M. for the PAO Collaboration, 2007)). If the energy uncertainty is negligible, $N_\mu(600)$ is the best parameter for mass discrimination analysis. However, as opposed to the other parameters which depend on the energy logarithmically, the number of muons is almost proportional to the primary energy. Therefore, the energy uncertainty will affect more the discrimination power of $N_\mu(600)$ than that of the other parameters. Figure 3.15 shows g as a function of the energy assuming a 20% energy uncertainty for the parameters $N_\mu(600)$ and X_{max} (Supanitsky A.D., 2008). We see that the discrimination power of $N_\mu(600)$ decreases in such a way that it is of the order of the corresponding to X_{max}. From Figure 3.15 we also see that the discrimination power of X_{max} remains approximately the same when the energy uncertainty is included, which is due to its logarithmic dependence on the primary energy.

3.5 The accuracy in the measure of N_μ

3.5.1 The twin test

This section is focused on the measurement of the accuracy in the muon counting by the segmented muon detectors (Castellina A., 2012). Such accuracy is a basic element in the reconstruction procedure, and has to be determined experimentally using real events measured by the detector. Shower fluctuations are extremely difficult to simulate, due to the large number of particles of the cascades ($> 10^{11}$) and the uncertainties in the numbers of muons, electrons and gamma-rays, which depend on the hadron interactions and on the primary cosmic ray particle type. Moreover, the measurements in the field include environmental and instrumental effects (e.g. background from soil radioactivity and residual punch-through particles, PMT gain fluctuations and other noise effects) difficult to be correctly estimated in the simulation.

To test the baseline design, an engineering array also called Unitary Cell (UC) is being built at 7 of the 61 surface detector stations accompanied by 30 m^2 scintillator counter, forming an hexagon around the "Phil Collins" central SD. In this array (UC), each MC is composed of 4 modules rather than 3 since a module is halved into two with 200 cm long scintillator strips, providing 256 independent channels in order to assess muon pile-up close to the airshower core (see Figure 3.16). Finally, the rest of the 54 muon detectors will be deployed in the production phase.

In order to directly measure the accuracy in the muon counting, the Torino group has proposed to double the muon counters at two nominal positions, e.g. in the center of the Unitary Cell (covering an area of 1.46 km^2) and close to a station in the crown (Figure 3.17a). Then, they are deployed in an "L" layout in an effort to reduce the counting uncertainty produced by inclined muons that could cross two scintillators instead of one (clipping corners).

Each counter consists of two 10 m^2 plus two 5 m^2 modules, as sketched in Figure 3.17b, where the 5 m^2 ones provide better segmentation of the detector to make it suitable to measure particle showers closer to the core where the number

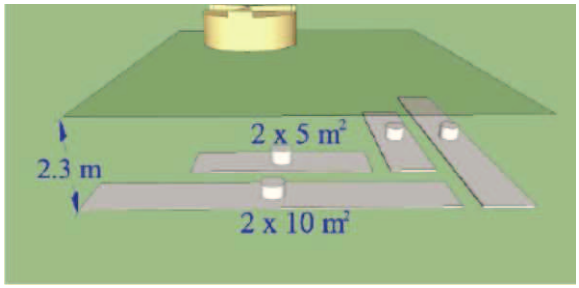

Figure 3.16: Layout of an AMIGA detector pair with the muon counter (bottom) buried alongside a regular SD station (top); in the layout shown here, one muon counter module is replaced by two smaller modules with half the size so that the muon counter consists of four independent modules instead of three.

of muons is higher, thus reducing the so called pile-up of muons. In each of these positions, they will be separated by about 10 m from each other. As the shower footprint is of the order of several square kilometers, these counters will virtually measure the same spot of the shower. The accuracy depends on the measured muon number (N_μ) but it is also possible to expect differences due to other factors including core distance, shower zenith angle, or cosmic ray particle type. The relative fluctuation in the number of muons can be defined as

$$\Delta = \sqrt{2} \times \frac{N_1 - N_2}{N_1 + N_2} \tag{3.4}$$

where N_i corresponds to the muons measured in the i-th detector of the pair. The $\sqrt{2}$ factor was added to take into account that Δ is defined as the relative signal fluctuation between two counters. The relative accuracy of a single counter is then given by the width of the Δ distribution, $\delta\Delta = \sigma/N$ where σ is the single counter accuracy (Ave M., 2007b). In order to obtain this expression it has to be assumed that $N_1 \simeq N_2$ and that $\sigma_1 \simeq \sigma_2$; quality cuts will be used to ensure the counters measure real EAS events, and the detectors are in principle identical, therefore their accuracies should be similar. For a perfect poissonian counter, the relative deviation $\delta\Delta = \sigma/N$ as a funtion of the N shoud should scale as $\sqrt{N}$. From the variance of $(\sigma/N)^2$ one can derive the error on the normalized single

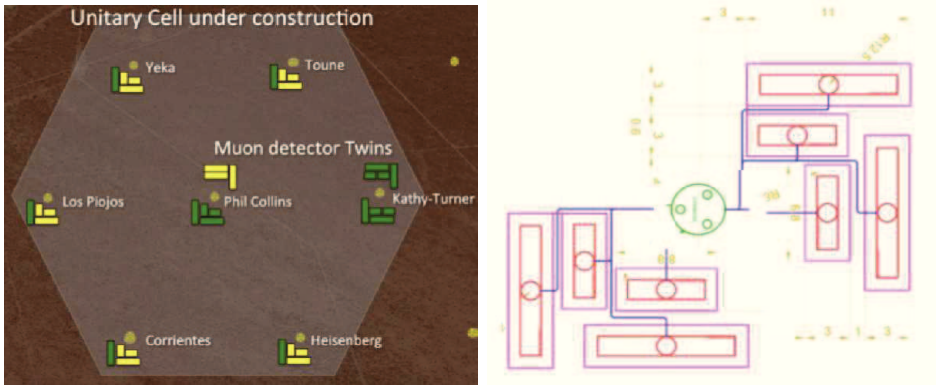

(a) (b)

Figure 3.17: (a): Layout of the AMIGA Unitary Cell. The muon detectors already installed are represented in green, and those to be deployed in near future are shown in yellow. The twin muon detectors at Kathy-Turner are operating and those next to Phil Collins are still under construction. The twin detector at Phil Collins consists of three modules (10 m^2 each) instead of four to validate a three modules design for production. **(b):** Schematics of the twin modules at the side of one surface detector station.

detector accuracy

$$V\left[\left(\frac{\sigma}{M}\right)^2\right] = \frac{1}{N}\left(m_4 - \frac{N-3}{N-1}m_2^2\right) \tag{3.5}$$

The accuracy must be measured at core distances $\geq$ 200 m (corresponding roughly to muon densities of the order of 3 m^{-2}), since for closer ones the pile-up effects spoil the muon counting. Figure 3.18 shows the accuracy computed for the corrected and randomized counts for two twin modules, for a uniform EAS distribution with 1 year of observation (Castellina A., 2012). Fitting the obtained accuracy using the expression

$$\frac{\sigma}{N} = \frac{p_0}{\sqrt{N}} \tag{3.6}$$

we get, as expected, a value of p_0 compatible with 1, with an error below 10%. Despite the quite low statistics, in one year we can measure the poissonian behaviour of the counters for a number of muons between 3 and 90, which corresponds to distances between 200 and 700 m from the shower core.

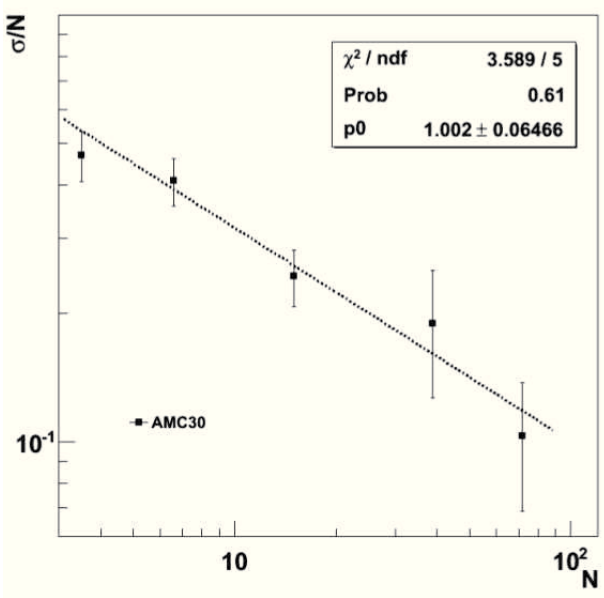

Figure 3.18: Randomized counts accuracy for the two twins, one year observation.

3.5.2 Additional systematics

Environmental effects like ground radioactivity, humidity, or electronic noise are examples of different additional systematic effects. Another well known problem is that of muons hitting the detector at an angle, thus producing a signal in two, or more, neighbouring strips. Figure 3.19 shows the measured counts N_c for particles hitting at $\theta = 30°$ and $\theta = 60°$, directly compared with the counts for vertical muons, for the 30 m^2 counters. The effect is evaluated for the worst case of $\phi = 90°$, that is, for orthogonal incidence at the strips and without including a threshold on the signal level (overestimating the effect). The counts can be larger than the incoming muons at low counts, when the pile-up effect is sub-dominant, and become similar to the counts for vertical muons at very large counts. As expected, this effect is larger for more inclined angles.

In principle, the relative counts variation with incident angle could be analitically corrected using pile-up correction formulae properly accounting for the incoming angle. It was checked the azimuthal dependence of this effect on an 30 m^2 module, in which 3 identical 10 m^2 counters are placed in an L-shape, with one module along an axis ($\phi = 0°$) and the other two orthogonal to it ($\phi = 90°$).

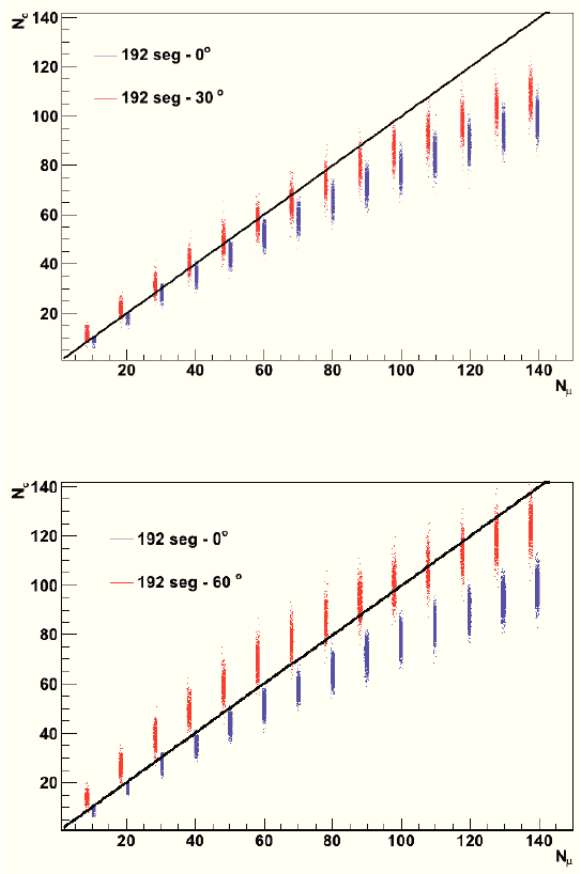

Figure 3.19: Measured counts from AMC30 for particles hitting at $\theta = 30°$ and $\theta = 60°$ and $\phi = 90°$ (red) compared to the vertical ones (blue).

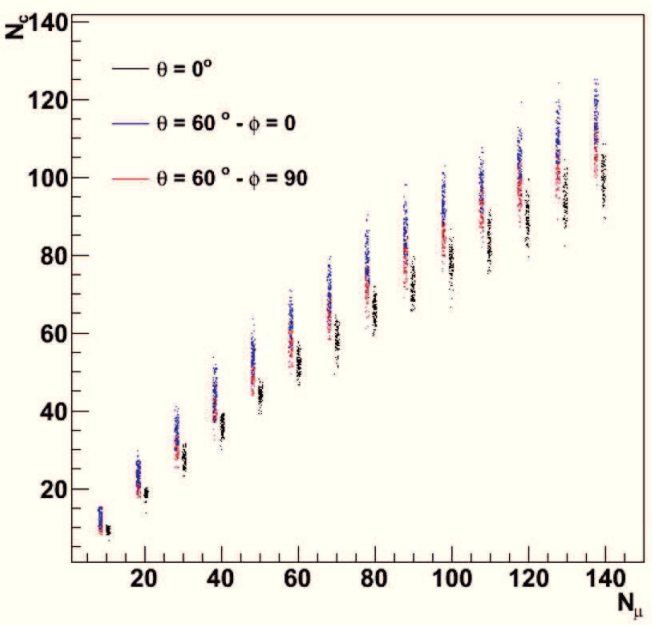

Figure 3.20: Pile-up effect for particles entering at 0° and 60° for an 30 m^2 counter with submodules of 10 m^2 type oriented in an L shape, for different azimuthal angles.

Figure 3.20 shows this effect for muons incoming at $\theta = 60°$, with $\phi = 0°$ and $\phi = 90°$ respectively.

As expected, the size of the effect is bracketed by the case of vertical muons (the blue points in in this figure) and the case shown by the red points in the bottom left panel of Figure 3.19 (all bars parallel). This observation supports the idea of performing an accuracy test with full-size 30 m^2 counters with symmetrically positioned modules, where the angle dependence is naturally mitigated due to different orientation of the 10 m^2 modules in the set. In order to study the sensitivity of the twin test, a generic source of systematic error proportional to the measured counts Nc it was simulated. These additional counts were added equally to both counters of the twin and the total was then randomized (Castellina A., 2012). To study the behaviour of the counters, it was performed a scan using a single 30 m^2 twin. The evolution of the fit parameter (eq.3.6) with increasing systematic error is shown in Figure 3.21(left). The high event statistics associated to this distribution ensures that this specific realization of the counts is a good representation of the average behavior of the accuracy. The result of the

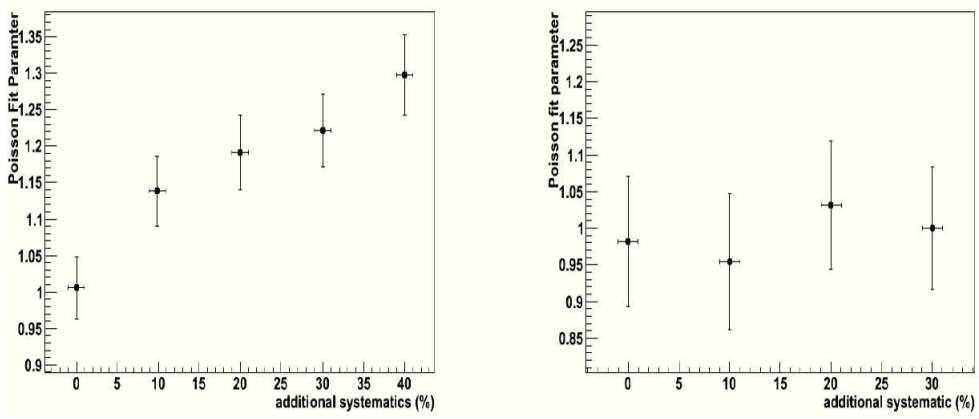

Figure 3.21: Left: Accuracy fit parameter for one 30 m^2 twin versus the added systematic uncertianty (%) for a distribution of EAS from 100m to 750m in steps of 0.1m. **Right**: Accuracy fit parameter for two 30 m^2 twins versus the added systematic uncertianty (%), for a uniform distribution of EAS in 1 year of observation.

same procedure applied to the real situation (two 30 m^2 twins, EAS uniformely distributed on the UC area) is shown in Figure 3.21(right) for 1 year observation. This result strengthens the proposal to use full size 30 m^2 counters for the accuracy study, taking into account an azimuthally symmetric geometry of the modules of each counter.

Chapter 4

The Muon Counters

4.1 Overview: scintillators, optical fibers, PMT

The AMIGA muon counter consists of segmented scintillators with optical fibers ending on 64-pixel multi-anode photomultiplier tubes (PMT). The scintillator strips are equal to those used for the MINOS experiment (Adamson P. for the MINOS Collaboration, 1998) and manufactured by Fermi National Accelerator Laboratory, FNAL. The current baseline design calls for 400 cm long × 4.1 cm wide × 1.0 cm thick strips of extruded polystyrene doped with fluors, POP (1%) and POPOP (0.03%), and co-extruded with TiO_2 reflecting coating. To extract the scintillation light, a wavelength shifting fiber is glued into a grove which is machined along one face of the scintillator strip. The groove is covered with a reflective aluminum tape to seal the reflective properties of the scintillator. The attenuation length of the extruded scintillator bars is $\sim 55 \pm 5mm$ (with the TiO_2 layer), therefore the light pulses must be transported to a photomultiplier tube (PMT) using an optical fiber (see Figure 4.1).

The fibers chosen for the scintillator modules are 1.2 mm rounded Saint-Gobain BCF-99-29AMC multi-clad fibers. These fibers have maximum light absorption and emission at 410 nm and 485 nm, respectively, while the scintillators emit light at ∼400 nm.

The scintillator strips are organized into two groups of 32 at each side of a central dome (Figure 4.2), where a 64 multi-pixels Hamamatsu H8804-200MOD photo-multiplier tube and the module electronics are placed. The H8804-200MOD

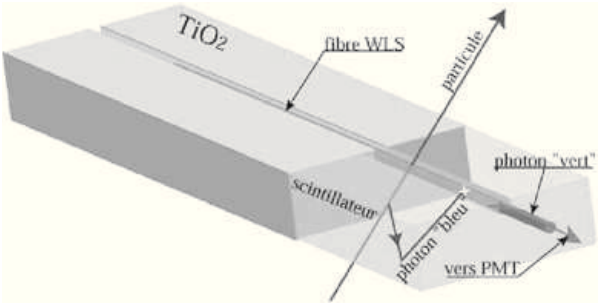

Figure 4.1: Scheme of a scintillator bar being excited by a particle.

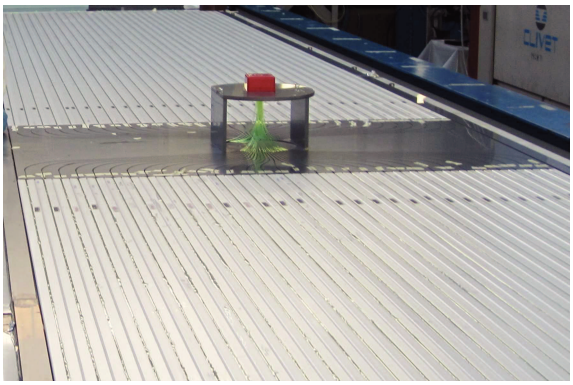

Figure 4.2: The fiber router and the optical connector. The protective dome has been removed.

is head-on photomultiplier, with a 30 mm^2 ultra-bialkali photocathode, 8 × 8 multi-anode, each pixel with dimensions of 2 mm × 2 mm, 12 stage, high speed response and low capacitive cross-talk. The ultra-bialkali photocathode quantum efficiency peaks at 350 nm with an efficiency still 20% at ≥ 480 nm (Figure 4.3). The high voltage divider chain is provided by Hamamatsu together with the PMT..

The basic unit of each module is lodged in a waterproof PVC casing built with thin PVC panels. Its structural stability is provided by four PVC U-bars placed along the module at both sides of the central dome. Each fiber termination is smoothed by means of a diamond polishing tool mounted in a fly cutter. An alignment system is used to obtain the correct coupling of the PMT with respect to the optical connector as shown in Figure 4.4.

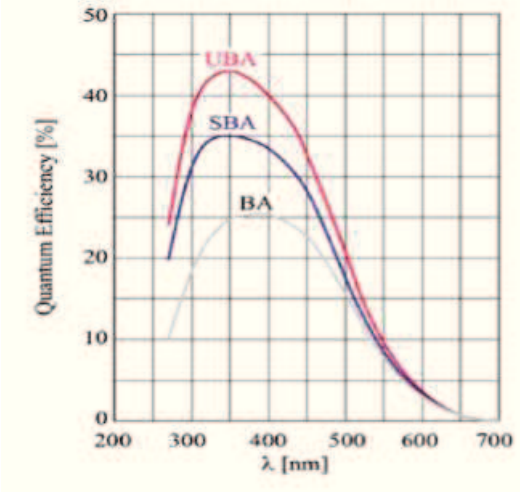

Figure 4.3: Quantum efficiency spectrum of the Ultra-Bialkali photo-catode (UBA, red) compared with Bialkali (grey) and Superbialkali (blue) ones

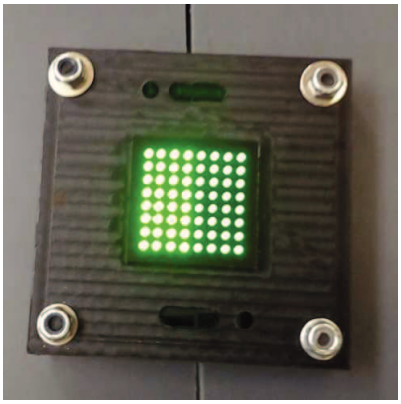

Figure 4.4: Before gluing on the scintillator strips, the fibers must be glued on a support (kuki) which allows the coupling with the phototube. Once glue is dry, the tip of the fibers are milled, like shown in the picture.

Each muon counter consists of three of these 64-channel modules, totalling 192 independent channels covering an effective area of 30 m^2. These muon counters will be buried alongside a water Cherenkov tank.

4.2 Muon Module Electronics

The AMIGA module electronics and its related software implement a purely digital readout just counting pulses above a given threshold, without a detailed study of signal structure or peak intensity. Besides strongly reducing the information to be sent to the Auger central data acquisition system (CDAS) from individual tanks, this method is almost independent of the PMT gain and its fluctuations and of the muon hitting position along the scintillator strip. On the other hand, a detailed knowledge of the scintillation efficiency for each strip and a continuous monitoring of the residual background due to natural radioactivity is mandatory to choose the discrimination threshold and to define the best algorithm to recognize genuine muon signals.

Each station has the following components: one or more detection modules acquiring and sending data to a storage system, a trigger source synchronizing data acquisition, a communications system connecting the modules with the storage system, and a power source powering all the electronics within the station. The electronics for each module consist of three stages: *Front-End*, *Acquisition*, and *Control and Communication* (Almela A., 2013). The *Front-End* stage acts as an interface between the particle detector and the Acquisition stage. The *Acquisition* stage continuously samples the output of the Front-End, and temporarily stores the sampled data when a trigger condition is found. Only a small number of these data points are required for further study. The *Acquisition* stage was implemented using a Field Programmable Gate Array (FPGA). Finally, the *Control and Communication* stage is in charge of the environment monitoring, module configuration, data requests and data transfer of monitoring information and event data to the storage server. The system allows stations with an arbitrary number of modules, and does not impose restrictions on the module type. Each station has a communications system which consists of a router that incorporates an Ethernet switch connecting the modules and a radio used for communications

with the central server. The *Control and Communication* stage uses a microcontroller running an operating system and applications used for data transmission and module control.

AMIGA modules were designed to use an external trigger in order to acquire event data during a possible particle shower. This trigger and the data request system are provided by the SD of the corresponding station. The SD trigger briefly works in the following way (Abraham J., 2010) : Each SD has a self-trigger (T1) with an average rate of ∼100Hz. When a T1 happens, a signal is sent to the acquisition electronics. Upon reception of this signal, the acquisition electronics stores the event data in memory with a GPS timestamp (GTS), used to identify the event. Once per second, the SD sends a list with the GTS that corresponds to possible events to the Central Data Acquisition System (CDAS) . Upon reception of a data request (T3) from CDAS, the SD sends the event data corresponding to the GTS received in the request. The SDs belonging to AMIGA were upgraded with the ability to output a signal each time a T1 is produced, and additional electronics called Trigger and Data Request (TDR). When a T1 trigger occurs, the SD sends a signal to the AMIGA modules containing a Local Timestamp (LTS), which is a 24 bit number generated by a free running counter. Taking into account the average T1 rate, each LTS value is guaranteed to be unique for ∼26.8 s, enough time to ensure that requested events won't have data collision with newer events. After the T1 has a GTS associated, a signal containing the LTS and a reduced version of the GTS (48 bits total) is sent using a SPI protocol to the TDR, which stores this pair in a buffer capable of holding 2048 pairs. The TDR also has a sniffer that detects T3 requests aimed at the station. When a T3 is found, the TDR looks for the received GTS in the table. If the GTS is found, its corresponding LTS is broadcasted to all the modules via UDP. Otherwise, a "LTS not found" message is broadcasted to the modules. The TDR also provides access to the SD serial console via SSH or TELNET protocols.

The AMIGA *Front-End* conditions and digitalizes the signals coming from the PMT. It consists of a Mother Board, providing the power supply (Hamamatsu

C4900-1) and the socket for the multi-channel PM, and distributing the PM signals to eight Daughter Boards, handling eight PM channels each. Once inside the Daughter Board, each signal is amplified using a current feedback transimpedance amplifier and digitalized by a comparator with a configurable voltage threshold (Buchholz P. for the PAO Collaboration, 2009). The comparator outputs a digital '0' if the signal is above the configured voltage threshold, or a digital '1' otherwise. The threshold is meant to be configured in order to filter noise signals generated by the PM. The *Acquisition* stage is done by a Digital Board using a FPGA, which continuously samples the output from the Front-End at 320 Msps. The Digital Board also drives the DACs used to set the threshold level of the discriminators used in the Daughter Boards. *Control and Communication* services are provided by the Control Board, which is the only new hardware part of the new module design. This board uses a microcontroller running an operating system in order to provide the necessary services. The services provided by the microcontroller could be provided by a soft-core running on the FPGA which would have lowered the power consumption of each module, but time constraints and a requirement to integrate with existing hardware made the external microcontroller a better option.
The current FPGA implementation is divided into six main blocks, as shown in Figure 4.5.

4.3 Counter Segmentation and Pile-up correction

The AMIGA counter electronics just counts pulses above a given threshold, without a detailed study of signal structure or peak intensity. This one-bit electronics design relies on a fine counter segmentation to prevent undercounting due to simultaneous muon arrivals. The optimum segmentation of the muon counters depends on the number of muons arriving in the time given by the system time resolution. Since the MLDF decreases very rapidly with the distance to the shower axis we need to determine the average position of the closest station, where pile-up is more significant. The position of the first station depends on the

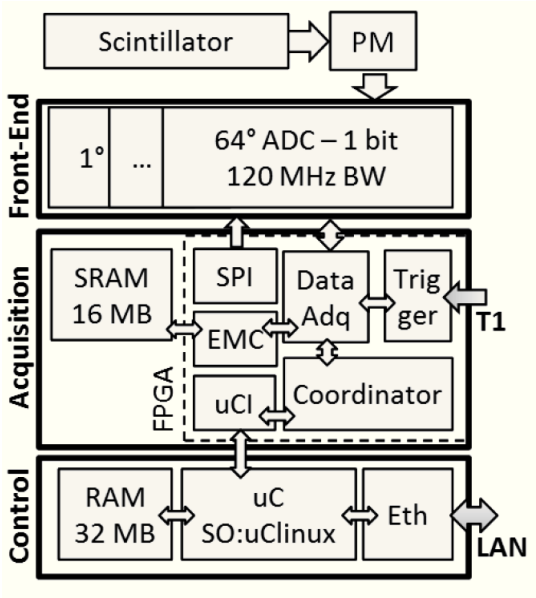

Figure 4.5: Block diagram of the AMIGA module electronics.

geometry of the array and the angular distribution of cosmic rays. A simulation was performed distributing showers on an area according to $cos(\theta)sin(\theta)$ in θ, linearly in r, and uniformly in ϕ. The distribution of the closest distance to the core is shown in Figure 4.6, the mean value resulting to be ∼230 m (Supanitsky A.D., 2008). Therefore, we will base our subsequent studies on the number of muons found at a characteristic distance of 200 m.

The mean time distribution of muons at 200 m from the core (and 2.3 m underground) is shown in Figure 4.7; the maximum number of muons in the first 20 ns is $\simeq$ 90 (Castellina A., 2012).

Because of the finite number of scintillating strips of each counter, and of the digital readout electronics that only counts signals above threshold, whenever two or more muons hit the same scintillator strip in the same time bin, these multiple muons will be counted as one, and therefore the total number of counted muons, N_μ^C, is lower than the incoming number of particles N_μ. Following (Supanitsky A.D., 2008), this pile-up effect can be analitically computed using the following

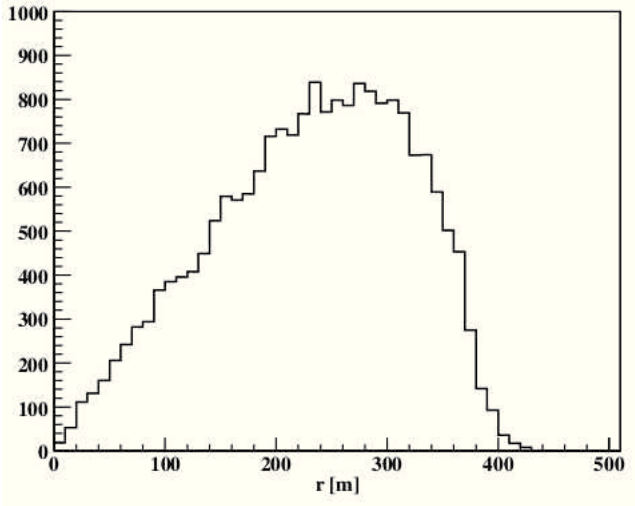

Figure 4.6: Distribution of shower axis to closest station distance for a 750 m-array for an isotropic incident flux of cosmic rays with $\theta \leq 60°$ (Supanitsky A.D., 2008).

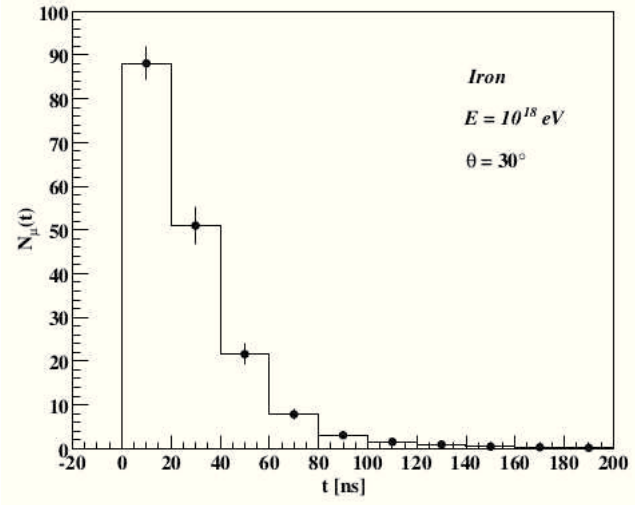

Figure 4.7: Time distribution of muons at 2.5 m underground and at 200 m from the shower axis in an area of $30 \times cos(30°)m^2$. The showers were initiated by iron nuclei of E $= 10^{18}$ eV and $\theta = 30°$.

equation

$$N_\mu^C = N_{seg}\left[1 - \left(1 - \frac{1}{N_{seg}}\right)^{N_\mu}\right] \tag{4.1}$$

where N_{seg} is the number of segments. The variance on the number of counted muons N_μ^C can also be analitically computed and is equal to:

$$\begin{aligned} Var(N_\mu^C) = N_{seg}\left(1 - \frac{1}{N_{seg}}\right)^{N_\mu}\left[1 + (N_{seg}-1)\left(1 - \frac{1}{(N_{seg}-1)}\right)^{N_\mu}\right. \\ \left. - N_{seg}\left(1 - \frac{1}{N_{seg}}\right)^{N_\mu}\right] \end{aligned} \tag{4.2}$$

Figure 4.8 shows the number of counted muons as a function of the incident muons for a muon counter with 192 segments. To correct the effect of segmentation we can invert Eq. 4.1,

$$N_\mu^{corr} = \frac{ln\left(1 - \frac{N_\mu^C}{N_{seg}}\right)}{ln\left(1 - \frac{1}{N_{seg}}\right)} \tag{4.3}$$

The total number of counted muons N_μ^C is thus equal to the incident one N_μ only for infinite segmentation.

This correction has an error $\sigma_\pm$ whose magnitude strongly depends on the number of segments of the modules and is asymmetric with respect to the central value N_μ^{corr}. This error can be estimated by solving for a given N_μ^{corr} the following equations,

$$N_\mu^{corr}(N_\mu^C + \sigma_+) = N_\mu^{corr}(N_\mu^C) + \sqrt{Var(N_\mu^C)} \tag{4.4}$$

$$N_\mu^{corr}(N_\mu^C - \sigma_-) = N_\mu^{corr}(N_\mu^C) - \sqrt{Var(N_\mu^C)} \tag{4.5}$$

The total error for $\Delta N_\mu^\pm$ will be the quadratic sum of $\sigma_\pm$ and the Poisson fluctuation on N_μ^{corr}, $\sigma_{Poiss} = \sqrt{N_\mu^{corr}}$

$$\Delta N_\mu^\pm = \sqrt{\sigma_\pm^2 + \sigma_{Poiss}^2} \tag{4.6}$$

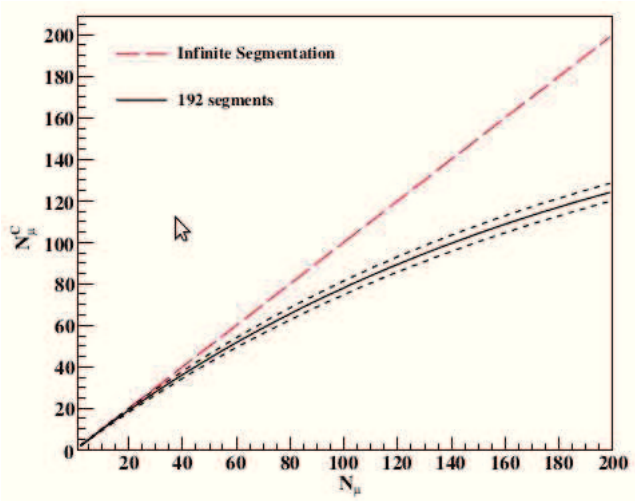

Figure 4.8: Mean value and one sigma region of the number of muons counted as a function of the incidents for 192 segments (three PMTs with 64 pixels each). In the ideal case of infinite segmentation $N_\mu^C = N_\mu$.

Figure 4.9 shows the ratio between the total error and the Poissonian one as a function of the number of muons obtained after correction for the case of 192 segments. From this figure we see that for 90 incident muons the total error is greater than the Poissonian by less than 14%, and as such there is no need to further segment the detector. Note that the individual uncertainty in each muon counter will not directly translate to the $N_\mu(600)$ and it will be further reduced when a number of counters are used to fit the MLDF (Supanitsky A.D., 2008).

4.4 Punch-through

Extensive air showers if not very inclined, are mainly composed of γ, $e^\pm$ and $\mu^\pm$. Figure 4.10 shows the energy distributions for each of these particles at 200m from the core of a proton shower at $\theta = 30°$, 1 EeV primary energy.

γ's and $e^\pm$'s are the most abundant particles while $\mu^\pm$'s have, by far, the highest energies. The distributions of the electromagnetic component peaks below 100 MeV while the muon maximum is close to 10 GeV (Design Report AMIGA, 2006). Although the electromagnetic component of the shower is much less penetrating

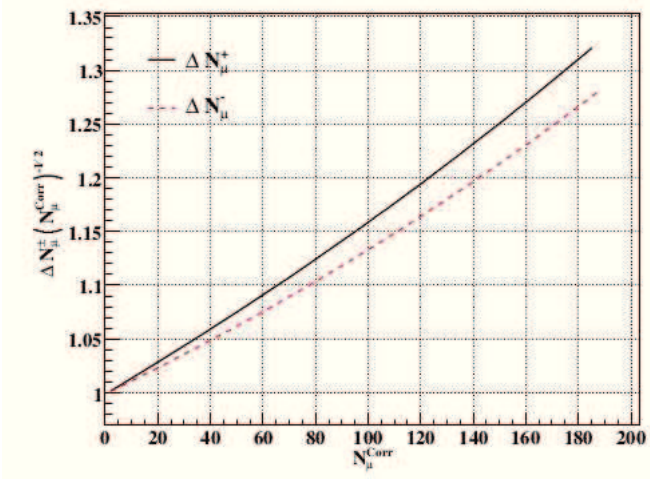

Figure 4.9: Ratio between the total error and the Poissonian error as a function of the corrected number of muons, for a counter with 192 segments. The two curves show explicitly the asymmetry of the errors.

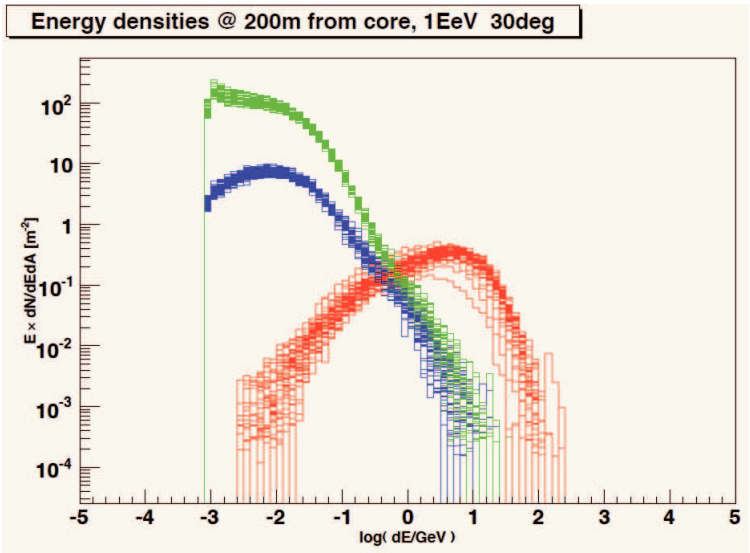

Figure 4.10: γ, $e^{\pm}$ and $\mu^{\pm}$ energy density distributions at 200m from the shower core. Fifty proton induced showers with zenith angle 30° are superimposed (Design Report AMIGA, 2006).

than the muons, it can, which, if the energy is high enough, may then reach the buried muon detectors and produce a signal that is indistinguishable from the one left by muons. The fraction of the electromagnetic component able to reach the scintillator is called *punch-through*. It depends on the minimum energy E_{dep}^{min} deposited in the scintillator. When a charged particle enters the scintillator, it leaves a wake of excited molecules. The light yield inside a scintillator is proportional to the energy deposited by the particle. Typical values for a standard plastic scintillator are 8-10 photons per deposited keV (Knoll G. F., 2000). It was experimentally estimated that for the AMIGA scintillators, an energy deposition of at least ∼100 keV is approximately required to produce a single photoelectron. The required shielding, that is the depth at which the scintillator detectors should be buried to effectively reduce the punch through effect, was determined by means of simulations. The distribution of total energy deposited per event inside the scintillator, $n = dN/d(log(E_{dep}))$, for the particular case of 1GeV γ's and μ's injected 1.5 m above the detector is shown in Figure 4.11 (Design Report AMIGA, 2006). In the figure, the open dashed and solid line histograms represent the energy deposited by 5000 γ's and 5000 μ's, respectively, thus assuming a 1:1 ratio between the particle densities of the two components. Nevertheless, when a real shower hits the ground there are much more 1GeV μ's than γ's. In the case of a 10^{18} eV proton shower, the ratio γ/μ is ~ 0.26 (see Figure 4.10). Weighting with this ratio, the energy deposition histogram of γ events decreases as indicated by the shaded area in Figure 4.11. As shown in the Figure, the punch through of 1GeV γ injected at 1.5 m is $\sim 13\%$. Nevertheless, if we consider that the minimum amount of energy (E_{dep}^{min}) to produce at least a single photoelectron is 100 keV (indicated by the vertical line in Figure 4.11), the punch through is reduced, in this particular case, to $\sim 9\%$.

We define the total punch through at a given depth D as,

$$PT(D) = \frac{\int_A \int_E S^{\gamma,e^{\pm}}(E) P^{\gamma,e^{\pm}}(E,D) dE dA}{\int_A \int_E S^{\mu^{\pm}}(E) P^{\mu^{\pm}}(E,D) dE dA} \tag{4.7}$$

where $P^i(E,D)$ is the probability of a injected primary of type i to deposit in the scintillator at least E_{dep}^{min}, and $S^i(E) = \frac{dN}{dEdA}$ is the spectrum at ground level.

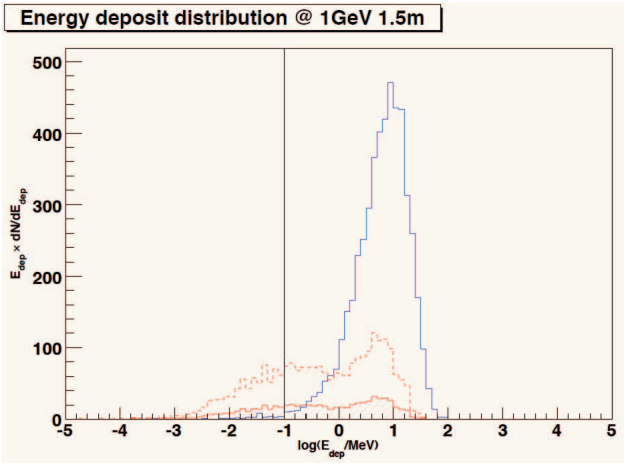

Figure 4.11: Total energy deposit distribution in a scintillator by 5000 γ's and 5000 μ^+'s of 1GeV injected 1.5 m above the detector. The open dashed and the solid line histograms indicate the situation if the injected particle densities were in a 1:1 relation. Full histogram is properly weighted with the ratio $(\gamma/\mu)_{1GeV} \sim 0.26$ given by the ground energy spectrum. Vertical line is the $E_{dep} = 100$ keV limit (Design Report AMIGA, 2006).

The functions $P^i(E, D)$ were calculated from distributions obtained with Geant4 simulations.

The punch-through has been studied by means of extensive simulations based on Geant4 (Design Report AMIGA, 2006). Figure 4.12 shows the fractional contribution with respect to the muon signal for fifty $10^{17.6}$ eV proton showers. It can be seen that below 2.5 m of soil the punch-through falls below 5%. Such a shielding sets a threshold on impinging muons of $E_{thr} \sim 0.9/cos(\theta)$ GeV.

The punch-through strongly depends on the chemical composition of the soil in which the detector is buried. Therefore, it is extremely important to perform detailed geological characterization of surface sediment samples of the Infill region. The studied samples are gravels (scales ¿ 2 mm) and pebbly sands (scales $<$ 2 mm) deposited in the alluvial plain of Cuenca Amarilla in Malarge. The sands and the sandy matrix of the gravels are coarse, lithic, feldspar-rich and quartz-poor sands. Most pebbles correspond to fragments of granite. The grain size follow, a bimodal asymmetric distribution corresponding to sand with medium to coarse pebbles. The granules are mostly angular. These sands are mostly composed by plagioclase, followed by quartz and, in subordinate amounts, cal-

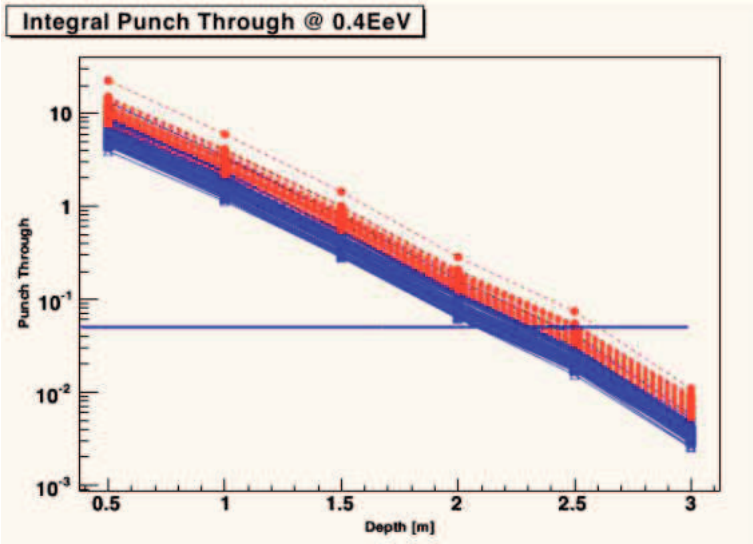

Figure 4.12: Punch through, PT(D), as a function of depth for showers of $10^{17.6}$ eV. The horizontal thick line indicates the limit of 5%. Each line correspond to a different air shower. The cases $E_{dep}^{min} = 0$ keV (red, full circles joined by dashed lines) and $E_{dep}^{min} = 100$ keV (blue, open triangles joined by solid lines) are shown.

cite, augite and clay minerals. Chemically, the sand is very homogeneous, and its composition will be described in the Section 8.1. The mineralogical (low quartz/feldspar ratio) and chemical composition, and the grain size distribution and shape indicate that these are immature sediments deposited very close from the source area rocks (Canet C., 2008).

Chapter 5

Laboratory measurements

5.1 Construction of the modules

In this section the basic properties of the muon detectors as measured during the construction of six modules (two 10 m^2 and four 5 m^2 units) in the mechanical workshop of INFN-Torino (Italy) will be discussed. These modules have been built in order to complete the Unitary Cell with two twin detectors, to study the muon counting accuracy (as discussed in Section 1.3).

For the mounting of the modules have been followed the following steps:

- the preparation of a workbench to allow the construction of the modules of 10 m^2 (Figure 5.1a).

- the preparation of a container in PVC where the 64 scintillator strips are arranged (Figure 5.1b).

- the positioning of the 64 scintillator strips into the container in PVC.

- finally, the mounting for the scintillator-fiber-PMT system.

  A groove at the center of each strip, not covered with TiO_2, hosts the optical fiber drowned in the groove with a special optical cement (made by glue and epoxies) able to match the refractive indices. This cement must

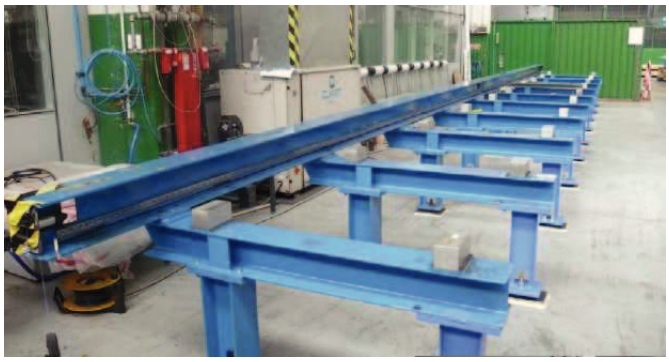

(a)

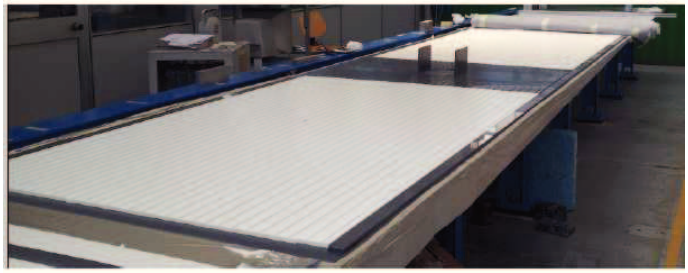

(b)

Figure 5.1: Construction phase. **(a):** The workbench preparation. **(b):** Inside a container in PVC where the 64 scintillator strips are arranged. 32 fibers from each side of the module are routed to a central optical channels connector matched and aligned to a 64 multi-pixels photo-multiplier tube.

be carefully mixed to avoid inhomogeneity and formation of air bubbles. Subsequently, the groove is covered with a reflective aluminum tape so as to permanently seal the reflective properties of the scintillator material (Figure 5.2a). This step is extremely critical because it is important to keep the fiber as deep as possible inside the groove to allow the maximum photon collection. The optical connection between PMT and fibers is obtained by means of a support in polyoxymethylene holding the 64 fibers end directly connected to the PMT in the central dome (Figure 5.2b). Note that, the opposite free edge of the fiber must be black painted in order to avoid reflections which would lead to an over estimation of the attenuation length.

After assembly, each module was subjected to vacuum test to avoid the air

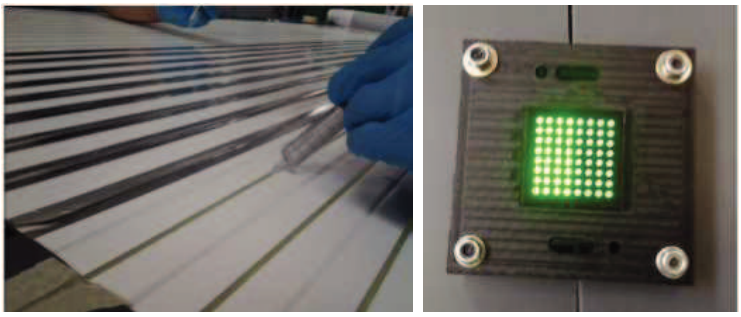

(a) (b)

Figure 5.2: (a): Gluing the fibers and integration with scintillator. **(b):** Support that allows the connection with the PMT.

presence (see Figure 5.3).

5.2 Fiber attenuation measurements

In order to calibrate the system, a measure of the number of single photoelectrons/μ is required, as a function of the distance between the impinging particle and the PMT.

The measurement is performed during the construction of the modules, using both atmospheric muons and a radioactive source.

To study the response of the modules to the passage of atmospheric muons two small detectors were used. Each of these detectors consists of a bar of scintillator (10 cm long $\times$ 4 cm wide $\times$ 2 cm high) and a photomultiplier, and they are placed one above and one below a given strip. Their coincidence generates a trigger for the FADC (1 GHz sampling rate, 10 bits), which reads the PMT signals from the module. An acquisition time of about one day allows a good measurement of the charge spectrum of the acquired signal. To increase the statistics, larger trigger scintillators (10×80 cm^2) were also used, allowing more strips to be measured at the same time. Several measurements on different modules, strips and at different distances from the PMT (computed along the optical fiber) have been performed. The muon traces so obtained as a function of the distance to the PMT were also memorized in a library, in order to be used in the Monte Carlo simulation of the

Figure 5.3: Complete module and vacuum test.

detector response, as will be described in Chapter 8. A complete calibration of each scintillator strip with a cosmic-ray hodoscope needs about one day of exposure for each point, which makes difficult to test the module directly with the distribution of the muons.
To speed up the process, a reliable and fast calibration system for the module production had been implemented, based on the use of the source scanner. In this way, accelerating the construction phase, each module can be tested in 5-6 hours.

Therefore, after the assembly, each module has been exposed to a 0.84 mCi ^{90}Sr β radioactive source, placed at a distance of about 10 cm above it, which moves at a constant speed (order of centimeters per second) through a X-Y positioning system controlled by a robotic arm (Figure 5.4).

The workbench is supported by a rail that allows the passage of the robotic arm, taking data at fixed locations. The movement is granted along X-axis and Y-axis with a step of 20 cm, while it is forbidden along Z. The arm is software controlled via a PC.

The decay scheme of the ^{90}Sr includes a first β^- decay into ^{90}Y which in turn undergoes β^- decay into ^{90}Zr. It therefore has a dual emission of electrons, at approximately 550 keV and 2.3 MeV respectively. Since the PVC cover layer has

Figure 5.4: Mechanical arm that carries the source during the scan.

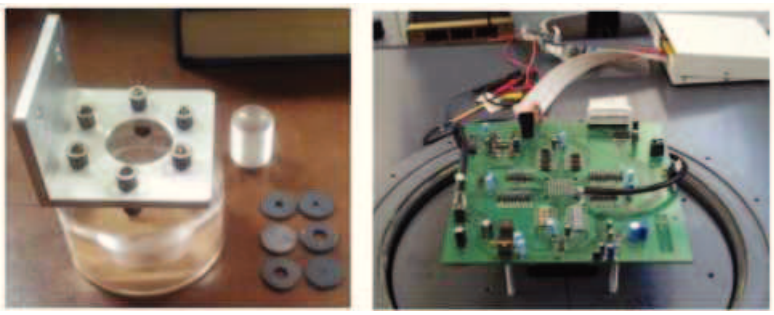

Figure 5.5: **Left**: Source container in plexiglass. **Right**: MPX board mounted on the PMT

a thickness of 2 mm, and considering minimum ionizing particles of $2 \sim \frac{MeV}{g/cm^2}$, the first electron will be stopped, while in the second emission electrons with energy of about 1.7 MeV will reach the scintillator. During the scan, the source is inserted in a cylindrical container in plexiglass (Figure 5.5 left). Inside the cavity there is space to place PVC discs. The cavity and the use of discs allows to collimate the outgoing radiation from the source. Due to the cylindrical shape and the material chosen it is possible to attenuate the radiation source and reduce the risks for operators. The thickness of PVC is chosen so as to have a current not more than 500 nA in the pixel tested when the PMT is powered by 950 V.

The signals acquisition is performed with a board multiplexer (MPX) (Figure 5.5 right). During the measurements the distances between the support where the fibers are connected to the PMT and the beginning of the strips were taken

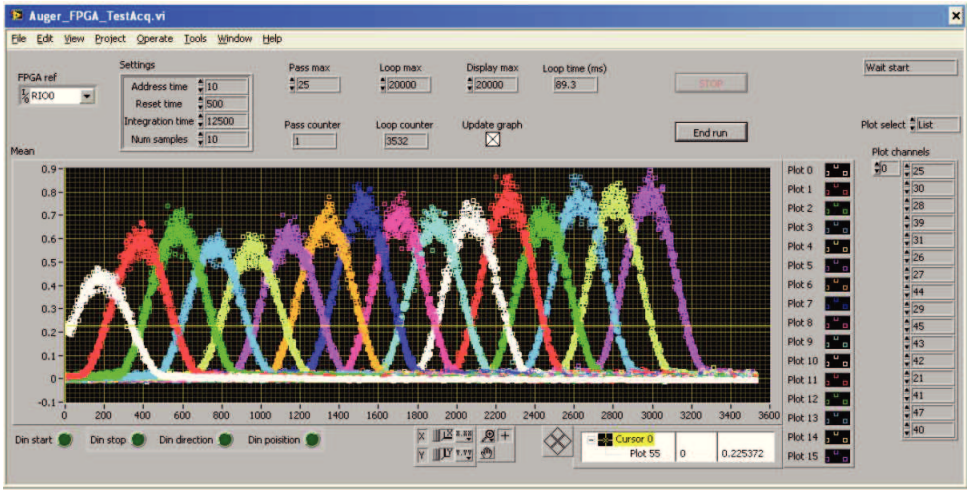

Figure 5.6: Multi channel signal as a function of time, each color corresponding to the different (subsequent) fiber under exam.

into account.

A readout board multiplexes the signals from each pixel of the PMT to a charge amplifier and a dedicated data acquisition system. The 64 channels are read out within 100 ms, allowing continuous monitoring of all the scintillator strips. The source is moved along the direction perpendicular to the strip length at a fixed distance from the central module. The signal of each pixel increases as the source is approaching, reaches a maximum value and then decreases (Figure 5.6).

The shown curves in Figure 5.6 were analyzed to extract the voltage values read by the board multiplexer. As we will show later, once obtained the voltage, it will be possible to derive the charge by means of a conversion ratio.

The test is performed for each fixed distance, producing 32 voltage profiles (similar to Figure 5.6). Each profile during the analysis data is cut in voltage (y-axis) to 300 mV (Figure 5.7a).

This cut is necessary to eliminate the undesirable effects of electrical noise. Each profile is then fitted with a Gaussian function, which normalization constant gives us the voltage value. This analysis is repeated for each strip and for all points. As a result of such *transversal scans*, the light attenuation profile (Figure 5.7b)(Maldera S. for the PAO Collaboration, 2013) is obtained for each

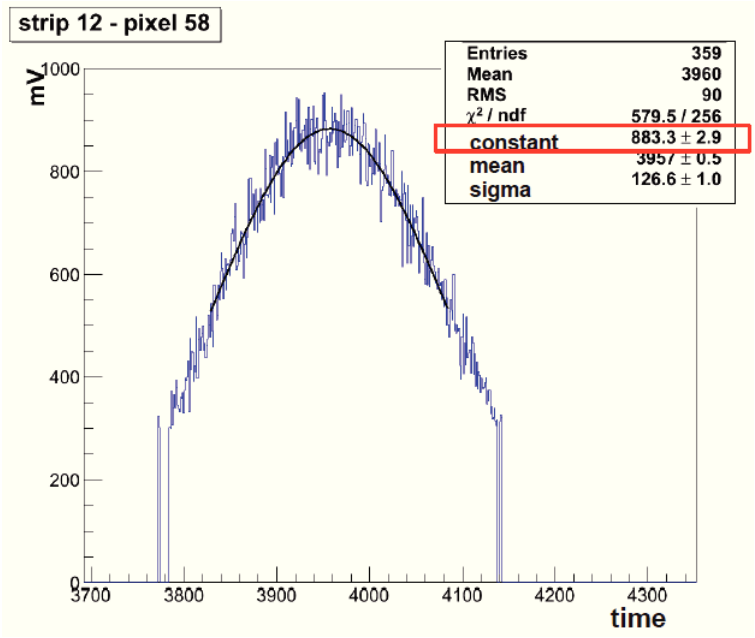

(a)

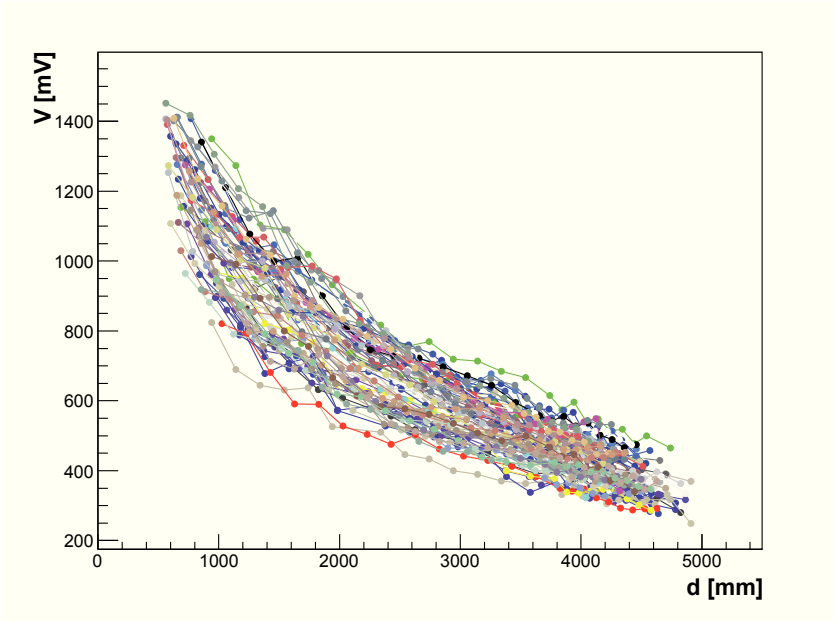

(b)

Figure 5.7: (a): PMT signals read through a multiplexer and a charge amplifier. The profile obtained is cut to 300 mV to eliminate the undesirable effects of electrical noise and then fitted to a Gaussian distribution. **(b):** Results of the scan with the 0.84 mCi ^{90}Sr radioactive source for one 10 m^2 module. The signal from each of the 64 scintillator strips is shown as a function of the distance from the PMT.

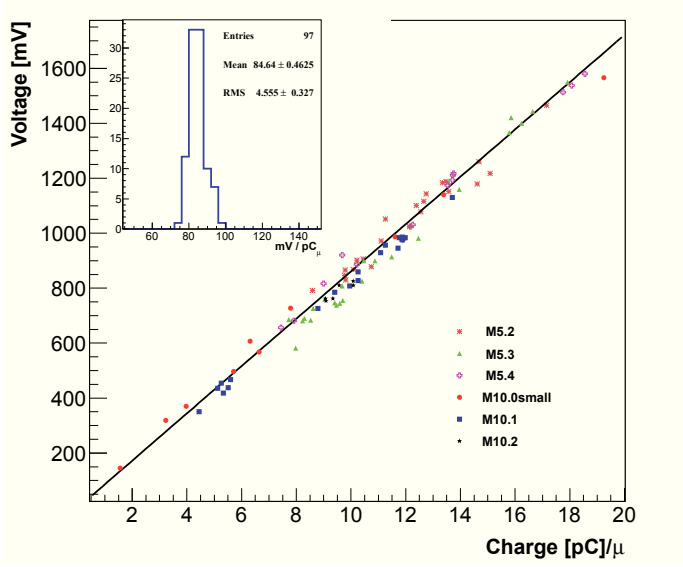

Figure 5.8: Normalization of the signal measured with the radioactive source to the average charge collected per muon crossing the detector vertically. The histogram of the ratios among all the measurements is shown in the top left corner. The width of this histogram gives the uncertainty in the normalization value.

fiber.

Summing, the multiplexer board extracts voltage signals. Therefore, it is necessary to derive a relation that allows us to convert the voltage value associated with the passage of the source above the strip, in the deposited charge by a muon. The measurements performed on the modules, have allowed to normalize the results obtained with this radioactive source to the mean collected charge when a muon crosses the detector vertically.

In fact

$$\left\langle \frac{V_{scan}}{Q_\mu} \right\rangle = (84.64 \pm 0.25) \left[\frac{mV}{pC} \right] \tag{5.1}$$

where Q_μ is the average charge deposited per muon crossing the detector vertically and V_{scan} is the signal generated by the radioactive source read out through the charge amplifier.

The error on the conversion factor $\left\langle \frac{V_{scan}}{Q_\mu} \right\rangle$ is calculated as the $RMS/\sqrt{Entries}$, which expresses the variation of one mean value. Considering the single measure-

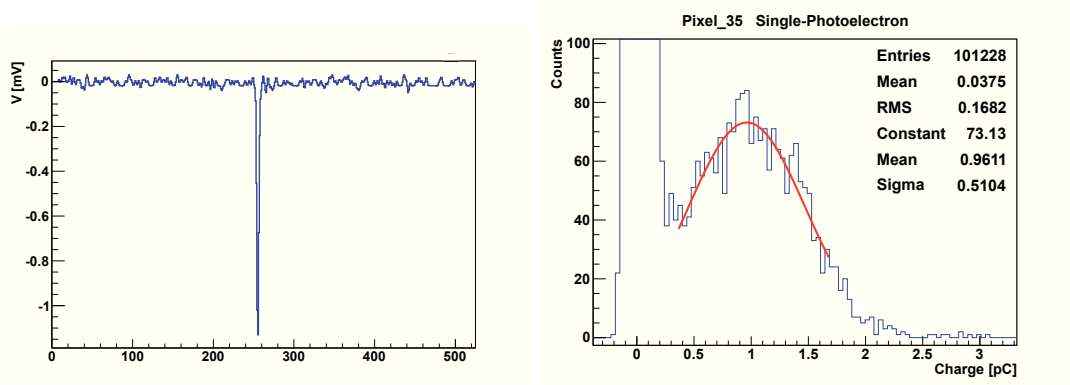

(a) (b)

Figure 5.9: (a): Single photoelectron signal. **(b)**: Figure shows both the distribution of null events and the single photoelectron.

ment, it is appropriate to use the RMS value as an error, which returns an error about 5%.

The gain of the PMT is an important key to determining the amount of light detected. To calculate the gain is necessary to make measurements of single photoelectron. This measurement needs a light source. In this case has been used an LED that emits blue light, illuminating a part of the fiber. A signal of single photoelectron is shown in Figure 5.9a.

The value of the charge is calculated as the area subtended the signal. It is possible to acquire many signals of this type, so as to derive the distribution of the values obtained. Acquiring a Poisson distribution with mean value of 0.05, about 95% of the events will be null. In Figure 5.9b one can see both the distribution of null events and the single photoelectron. The curve obtained is then fitted with a Gaussian function, which mean value gives us the value of the charge of the single photoelectron. The gain G of a photomultiplier is defined as the ratio of the anode current to the cathode current. The spectrum of single photoelectron previously obtained allows to obtain the current at the anode, while current at the cathode is given by the charge of the photoelectron emitted from the photocathode. Then,

the gain is defined as

$$G_{pixel} = \frac{SPE}{q_{e^-}} \tag{5.2}$$

where SPE indicates the charge of the single photoelectron (in pC) and q_{e^-} is the electron charge. The gain of the PMT supplied at 950V is of the order of 10^6.

Finally, the number of photoelectrons/μ ($N_{pe/\mu}$) produced at the PMT photocathode by a through-going muon can be derived as:

$$N_{pe/\mu} = \frac{Q_\mu}{G_{pixel}\, e} = \frac{V_{scan}}{R}\, \frac{1}{G_{pixel}\, e} \tag{5.3}$$

where e is the elementary charge, G_{pixel} is the gain of the specific pixel of the PMT, and R is the normalization factor (given by the ratio shown in Figure 5.8). In Figure 5.10a we show the result of the conversion of the measurements with the radioactive source to the number of photoelectrons, according to the formula above, for the 10 m^2 module. The uncertainty in the measured *n.p.e.* is about 12%, and has been derived from the combination of the uncertainties in the peak voltage obtained with the source (about 2%), in the normalization factor (8%), and the pixel gain (8%). The obtained attenuation curve shows that vertical muons crossing the detector produce between 5 and 15 photoelectron depending on the distance to the PMT. These results could be optimized by improving the fiber-scintillator-PMT coupling system. Figure 5.10b shows the attenuation curves for the six modules built in Turin (four 5 m^2 modules and two 10 m^2, labeled as M5 and M10 respectively). As discussed in Section 1.3, a module is halved into two with 200 cm long scintillator strips. As you can see from the figure, the 400 cm strips have a production of photoelectrons lower than strips of 200 cm. This result may be due to the length of the strip, which may cause light dispersion.

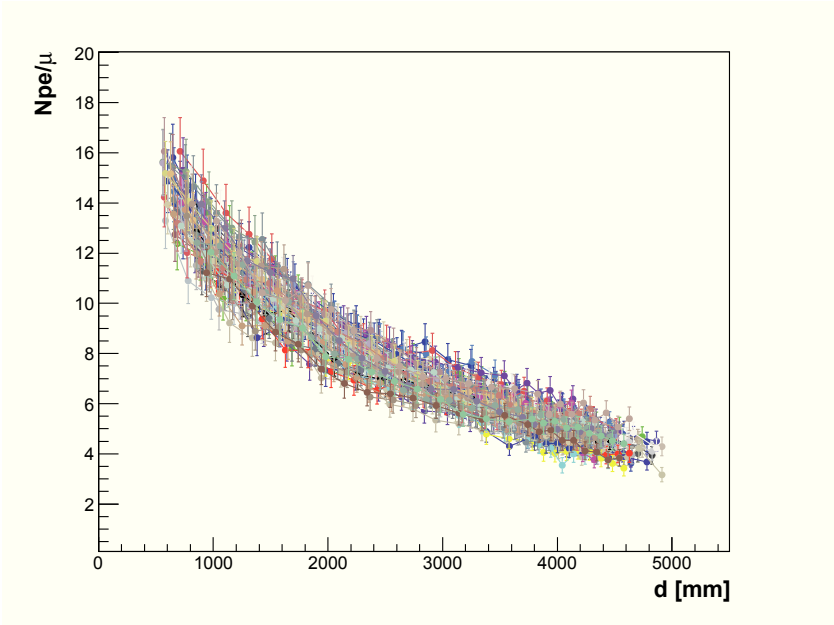

(a)

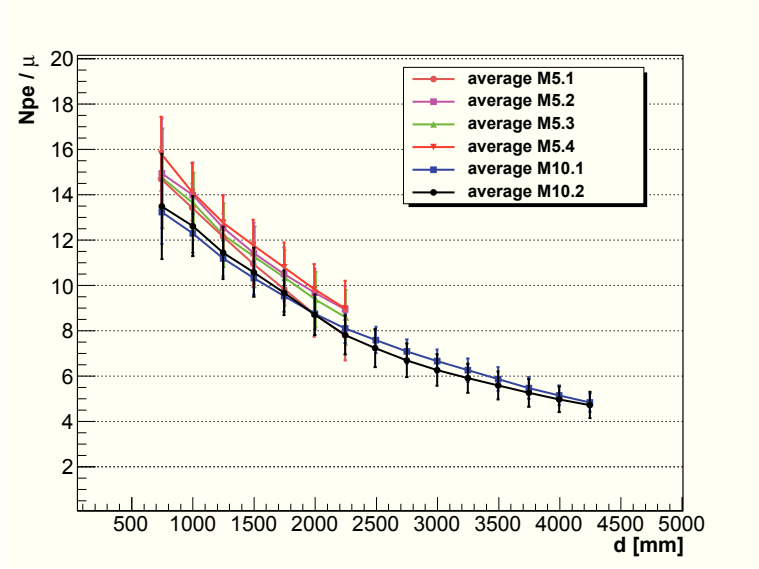

(b)

Figure 5.10: (a): Number of photoelectrons per muon crossing the detector vertically for the 64 strips of one module, obtained from the measurements made with the radioactive source. **(b)**: Number of photoelectrons produced by vertically crossing muons, at different distances from the PMT, for the six modules built in Torino (four 5 m^2 modules and two 10 m^2, labeled as M5 and M10 respectively). Each point represents the average of the 64 strips of the module, errorbars correspond to the RMS of their distribution.

Chapter 6

Simulation of the detector response

Our aim is to study the detector response. To do this, a library of muon traces, each of them filtered and resampled according to the experiment electronic readout will be built in order to be used in the simulation. As described in Section 5.2, muon signals have been recorded by means of an oscilloscope, using a sampling frequency higher than the one that will be employed in the real experiment. A low-pass filter has been considered, ie, an electronic filter that passes low-frequency signals and attenuates with frequencies higher than the cutoff frequency. To match the conditions of the readout electronics chosen for the muon module, such traces are convolved with the digital filter with a cutoff frequency of 140 MHz (while the bandwidth of the digitizer used in the laboratory is 500 MHz) and down-sampled to 320 MHz with a simple decimation algorithm. Each trace will be digitized according to a discrimination threshold, producing a digital data stream similar to the one expected from the real detectors.

6.1 Construction of a digital low-pass filter

Sampling is the first step of the process of analog-digital conversion of a signal. It involves taking samples from an analog signal in time intervals of Δt seconds. The value Δt is called sampling interval, while $f_s = \frac{1}{\Delta t}$ is the sampling frequency. The result is an analog signal in discrete time, which is then quantized, coded and

made accessible to any digital computer. The sampling is of course properly done only if the original analog signal can be exactly reconstructed from the sampled one. On the contrary, a bad sampling results in a distorsion of the original signal (aliasing).

The *Nyquist-Shannon sampling theorem* plays a crucial role in modern digital signal processing. The theorem states that, in an analog-digital conversion, the minimum sampling frequency necessary to avoid ambiguity and loss of information in the reconstruction of the original analog signal (ie in the digital-analog conversion) with finite bandwidth is equal to twice its maximum frequency,

$$f_s > 2 \cdot f_{max} \tag{6.1}$$

where f_{max} is the maximum frequency of the spectrum of the signal to be sampled. To avoid aliasing it is necessary to:

- Adopt an adequate sampling frequency, so as not to miss the information contained in the high frequency components of the analog signal acquired.
- Adopt an anti-aliasing filtering (low-pass filter), to eliminate the frequencies contained in the analog signal above the Nyquist frequency of the sampler, defined as $f_N = f_s/2$.

6.1.1 Digital Filters

Digital filters are used for two general purposes: (1) *separation* of signals that have been combined, when a signal has been contaminated with interference, noise, or other signals; and (2) *restoration* of signals that have been distorted in some way. As shown in Figure 6.1, every linear filter has an **impulse response**, a **step response** and a **frequency response**. Each of these responses contains complete information about the filter, but in a different form. If one of the three is specified, the other two are fixed and can be directly calculated. All three of these representations are important, because they describe how the filter will react under different circumstances (Smith Steven W., 1998).

The most straightforward way to implement a digital filter is by *convolving* the input signal with the digital filter's *impulse response*. When the impulse response

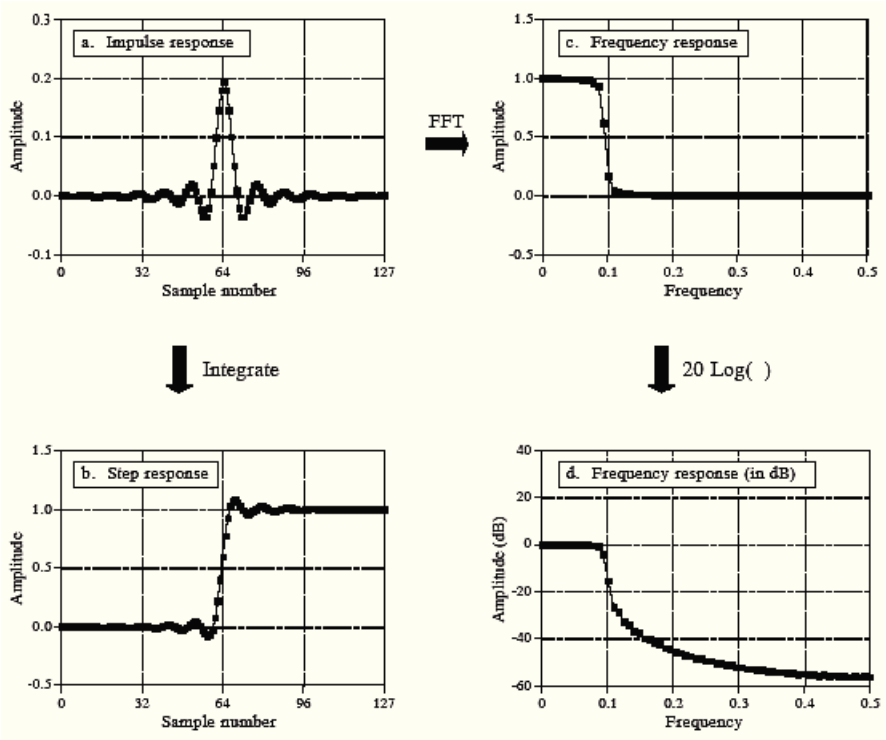

Figure 6.1: Filter parameters. Every linear filter has an impulse response, a step response, and a frequency response. The step response,**(b)**, can be found by discrete integration of the impulse response, **(a)**. The frequency response can be found from the impulse response by using the Fast Fourier Transform (FFT), and can be displayed either on a linear scale, **(c)**, or in decibels, **(d)** (Smith Steven W., 1998).

is used in this way, filter designers give it a special name: the filter *kernel*. There is also another way to make digital filters, called **recursion**. When a filter is implemented by convolution, each sample in the output is calculated by weighting the samples in the input, and adding them together. Recursive filters are an extension of this, using previously calculated values from the output, besides points from the input. Instead of using a filter kernel, recursive filters are defined by a set of **recursion coefficients**. To find the impulse response of a recursive filter, simply feed in an impulse, and see what comes out. The impulse responses of recursive filters are composed of sinusoids that exponentially decay in amplitude. In principle, this makes their impulse responses infinitely long. However, the amplitude eventually drops below the round-off noise of the system, and the

remaining samples can be ignored. Because of this characteristic, recursive filters are also called **Infinite Impulse Response** or **IIR** filters. In comparison, filters carried out by convolution are called **Finite Impulse Response** or **FIR** filters (Smith Steven W., 1998). One very important step in the digital signal processing is understanding how information is contained in the signals you are working with. There are only two ways that are common for information to be represented in naturally occurring signals: information represented in the time domain, and information represented in the frequency domain. Given the use that we will do our filter should dwell more on the characteristic parameters of the frequency domain. We will consider low pass filters, which purpose is that of allowing frequencies below a given threshold to pass unaltered. The **passband** refers to those frequencies that are passed, while the **stopband** contains those frequencies that are blocked. The region in between is called the **transition band**: if it is narrow, the **roll-off** will be fast. In analog filter design, the cutoff frequency is usually defined to be where the signal amplitude is reduced to 0.707 (-3dB).

6.1.2 Construction of a Windowed-Sinc Filter

Recalling that the electronics of AMIGA samples at 320 MHz, while in our laboratory we can acquire samples at 1GHz, to use the signals it is necessary to filter them. On the basis what said above, we will describe the construction of a FIR filter windowed-sinc. The choice of this filter type has been made for reasons of simplification. The windowed sinc filter uses the Inverse Fourier Transform of the frequency response of an ideal low-pass filter, that is a step function for which the transition band is infinitely small, and it is given by the cardinal sine $sinc = (sinx/x)$. The Inverse Fourier Transform of the required frequency response is taken and used as a kernel normal filter. To design a windowed-sinc, two parameters must be selected: the cutoff frequency, F_c, and the length of the filter kernel, M. The cutoff frequency is expressed as a fraction of the sampling rate, and therefore must be between 0 and 0.5. After F_c and M has been selected,

the filter kernel is calculated from the relation:

$$H[i] = K\frac{sin(2\pi F_c(i-\frac{M}{2}))}{i-\frac{M}{2}}\left[0.42 - 0.5cos\left(\frac{2\pi i}{M}\right) + 0.08cos\left(\frac{4\pi i}{M}\right)\right] \tag{6.2}$$

where the constant K must be chosen so that the sum of all the samples is equal to one; the length of the filter kernel M must be an even integer; and the sample number i is an integer that runs from 0 to M.

The term in square parentheses in the second member is called *Blackman window* and the values of the constants are obtained from

$$w[i] = \left[a_0 - a_1cos\left(\frac{2\pi i}{M}\right) + a_2cos\left(\frac{4\pi i}{M}\right)\right] \tag{6.3}$$

$$a_0 = \tfrac{1-\alpha}{2};\quad a_1 = \tfrac{1}{2};\quad a_2 = \tfrac{\alpha}{2}\ . \tag{6.4}$$

where $\alpha = 0.16$ (Harris J. Fredric, 1978).

As explained in Section 4.2, the PMT signals of the AMIGA modules are read by a modular readout system.

This filter has been implemented in the simulation code with parameters M and Fc settable, in order to reproduce the experimental results on the electronics amplifier of AMIGA obtained in Siegen, as shown in Figure 6.2a (Frohlich Uwe, 2009).

At this point it was possible to compare the plot of the bandwidth obtained in Siegen with the processed signal in Turin. To ensure a similar result, the parameters M and F_c were selected as those that best interpolate the plot. We will then use a filter taking care of the choice of parameters. The values obtained in order to build a cutoff at 134 MHz of -3dB appear to be M = 8 and F_c = 70 MHz (Figure 6.2b). The apparent change of slope is given by the different scales used along the X axis. The agreement is quite good, thus validating the filter implementation.

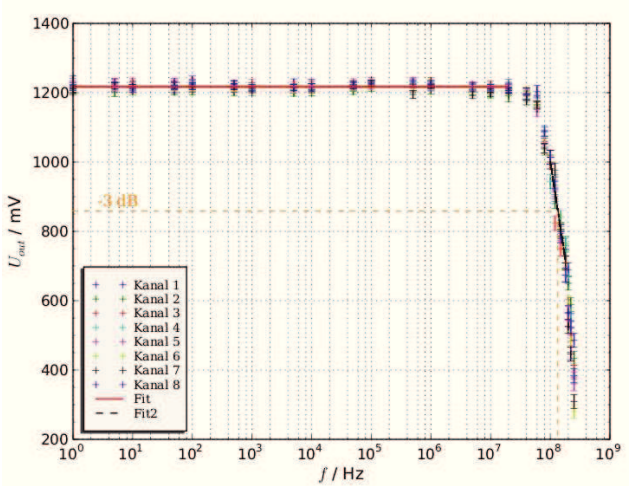

(a)

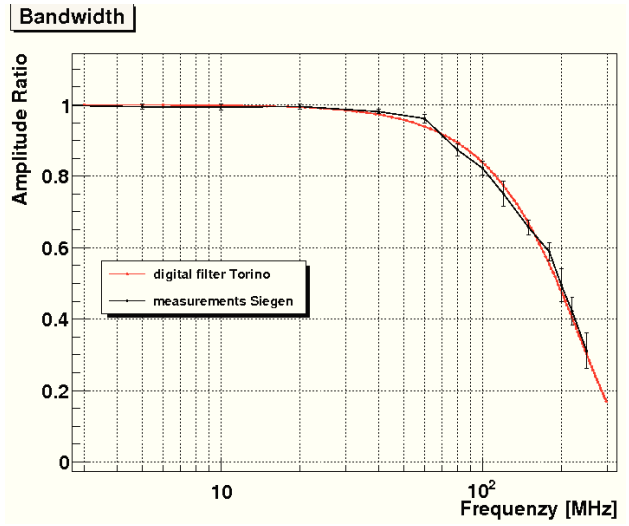

(b)

Figure 6.2: (a): Bandwidth measurement of a DB measured in Siegen. The bandwidth of the DB has been measured as (134 ± 5) MHz; **(b):** Comparison between the measurement made in Siegen and the one made in Turin. The good agreement validates our digital filter.

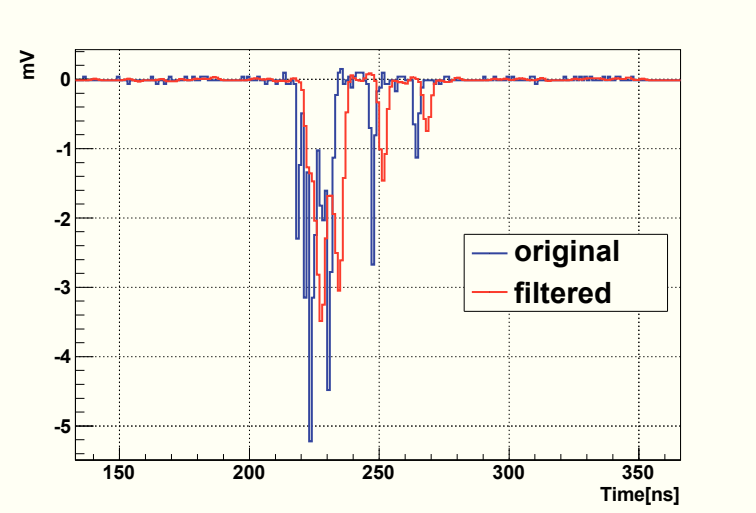

Figure 6.3: Filtered muon traces. Original trace (blue line) and filtered trace (red line)

6.2 Production of a muon traces library

A database of muon traces was then produced following different steps. First, all the muon traces measured in the Torino Laboratory, as describted in Section 5.2 have been filtered using the procedure explained above. In Figure 6.3, an example of a filtered muon trace is shown, superimposed to the original one. As one can see, the signal is reproduced at different sampling frequency without aliasing. All traces are divided according to the distance along the strip and the signal charge (14 bins in photoelectron units).

After filtering, all the traces have been normalized to the single photoelectron (SPE) mean amplitude and undersampled at 320 MHz (selecting 1 bin every 3.125 ns) with a simple decimation algorithm. In order to do this it was necessary to calculate the single photoelectron mean amplitude for each pixel. It can be seen that, after the subtraction of thebaseline, the distribution is fitted with a Gaussian function, which normalization constant gives us the amplitude value (Figure 6.4). This was done using two digitizers (DTA and DTB) each to four channels, and connecting each channel with a different strip, corresponding to the pixel relative. Table 6.1 shows the gains and the single photoelectron amplitudes for each pixel.

Finally, the traces are digitized according to a discrimination threshold, asso-

Strip	Pixel	Gain [x10^6]	SpePeak [mV]		Strip	Pixel	Gain [x10^6]	SpePeak [mV]
1	32	6.06766	16.7244		33	40	6.74671	15.9297
2	24	6.57464	16.1606		34	48	6.76606	17.6840
3	16	6.41299	15.9506		35	56	7.42291	18.3588
4	8	5.37494	14.0303		36	64	5.89032	14.9719
5	31	7.84068	19.4012		37	39	8.37092	19.5746
6	23	7.52940	18.8958		38	47	8.16422	20.3359
7	15	7.5993	19.4055		39	55	7.91427	21.0166
8	7	6.01582	19.4055		40	63	6.77629	16.5274
9	30	6.83922	16.8248		41	38	6.95672	17.5403
10	22	6.95323	18.2170		42	46	7.08157	18.0754
11	14	7.64260	19.0141		43	54	7.65347	18.5755
12	6	5.77796	15.4846		44	62	6.69707	17.5053
13	29	7.07384	16.7917		45	37	6.80156	16.8116
14	21	6.59562	17.1466		46	45	7.14665	18.1586
15	13	7.20532	18.2128		47	53	7.26145	19.0103
16	5	6.24276	15.5311		48	61	6.93718	17.0016
17	4	6.36188	15.6246		49	60	7.41903	17.8209
18	12	6.72027	17.5469		50	52	7.09488	17.4903
19	20	6.50573	17.1349		51	44	7.14665	16.1596
20	28	6.12428	16.1237		52	36	6.16918	15.5687
21	3	6.29896	16.0184		53	59	7.34108	18.5199
22	11	5.53749	13.8946		54	51	6.56389	16.5405
23	19	5.35721	13.5730		55	43	6.46876	15.9814
24	27	5.92972	15.2157		56	35	6.06383	15.1901
25	2	6.26853	15.3780		57	58	7.32426	17.8082
26	10	6.88424	17.8017		58	50	6.65033	17.0280
27	18	6.06696	16.0700		59	42	6.04724	15.3534
28	26	5.88012	15.1303		60	34	5.83918	15.0878
29	1	6.06766	15.3792		61	57	5.60396	15.3120
30	9	6.4427	17.0960		62	49	6.53329	16.9792
31	17	6.1165	15.9720		63	41	6.00381	15.3353
32	25	5.95449	14.8400		64	33	5.39205	14.5820

Table 6.1: Gains and single photoelectron amplitudes for each pixel.

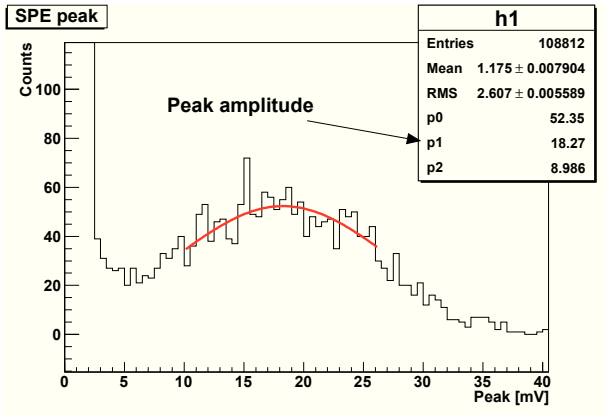

Figure 6.4: Typical single photoelectron mean amplitude. The curve is fitted with a Gaussian from which it is extracted one constant which gives the peak value.

ciating the passage of a muon to a sequence of signals above threshold (bit =1). After the discrimination, each signal will present a series of 1 and 0 spaced by 3.125 ns (1 bin), depending on the signal being above or below an adjustable threshold (e.g., 30% of the mean heigth of the single photoelectron). In Figure 6.5, an example of a muon trace is shown, before (top) and after (bottom) the discrimination and digitalization. If the threshold is too high, many signals do not go beyond the threshold and the rate is underestimate. One way to avoid the overcounting problem is to inhibit the second or subsequent peaks by means of a time veto window *timew* (in our case, it has been set to 30 ns). In this way, once a pulse is detected, subsequent pulses are ignored during a time *timew*.

6.3 Simulation of the detector response

The simulation of the detector responce is now feasible using the measurements and results describted in Sections 5.2 and 6.2. The aim is that of converting the energy deposited by a muon in the scintillator into an electronic signal. The total PMT signal depends on the number of photoelectrons extracted from the photo-cathode by the scintillation light. The total number of photoelectrons depends, in turn, on both the distance d from the PMT at which the light was produced and on the energy deposited inside the scintillator by the impinging

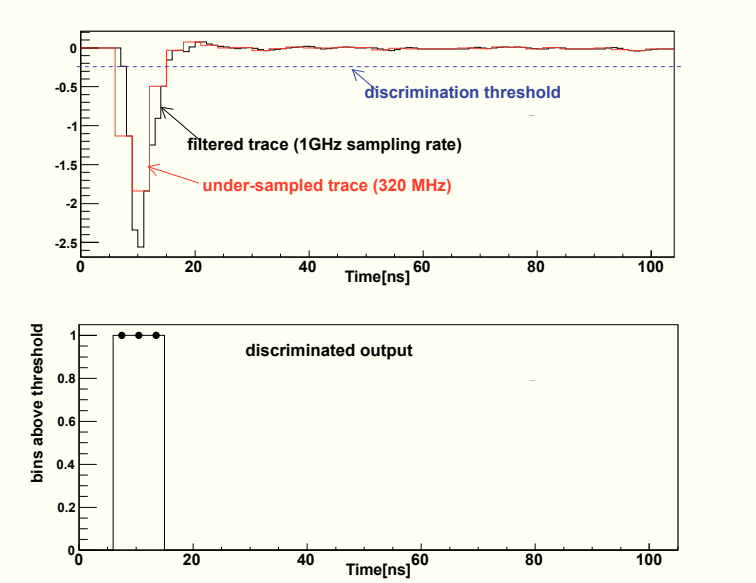

Figure 6.5: Top: Muon trace normalized to the mean amplitude of a single photoelectron and undersampled at 320 MHz. Bottom: Discriminated trace. Just the signals that exceed the threshold are represented by the bins.

particle. A GEANT4 simulation was perfomed to simulate almost vertical muons of energy 4 GeV with angular distribution $\propto cos^2\theta$, crossing one AMIGA strip located between two other scintillator bars, as shown in Figure 6.6. The choice of almost vertical events allow us to avoid energy losses related to geometrical effects. From the simulation, we obtain for each muon the entering position along the strip (thus the distance to the PMT) and the deposited energy E_{dep}.

A coincidence in the upper and lower scintillators allows to estimate the deposited energy on the central bar (see Figure 6.6).

The distribution of the mean deposited energy E_{dep} is shown in Figure 6.7. Clipping corner muons traversing the scintillator strip are responsible for the low energy tail of the E_{dep} distribution.

The energy deposited by a muon in the buried scintillator strip at a distance d from the PMT can then be converted to a mean number of photoelectrons at

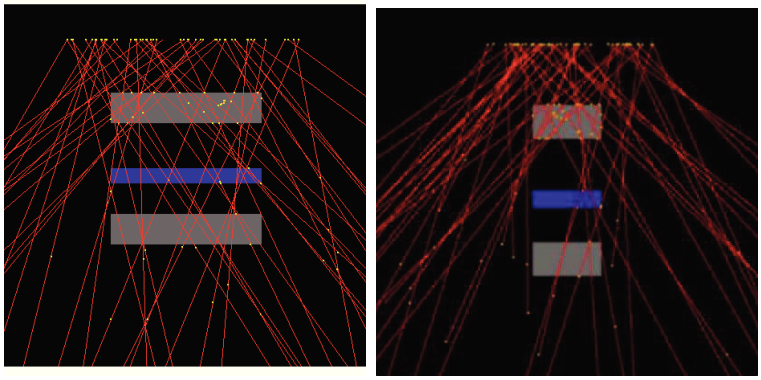

(a) (b)

Figure 6.6: Trigger system to select the muons. **(a):** Front view; **(b):** Top view. The deposited energy on the strip concerned (blue) is the one released by muons passing simultaneously through the two scintillators (in gray), used as triggers, and the strip (blue) in the middle. With this criterion atmospheric muons with a direction approximately vertical are selected.

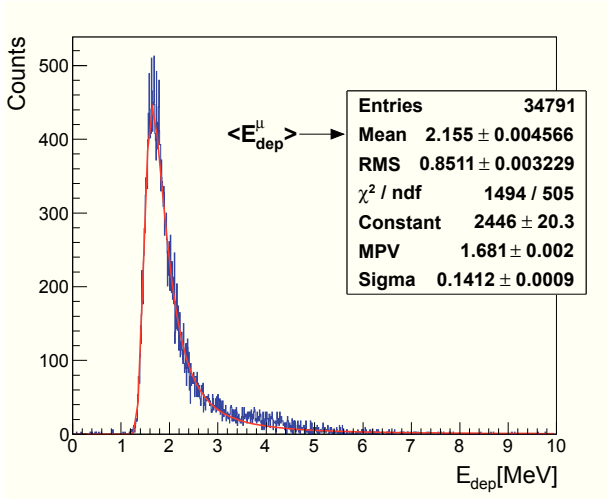

Figure 6.7: Energy deposit by the simulated muons in 1 cm thick scintillator bar (simulated by means of Geant4); a Landau function fit is superimposed.

the PMT by:

$$npe/_{\mu} = \frac{E_{dep}}{< E^{\mu}_{dep} >} N_{pe/\mu}(d) \tag{6.5}$$

In this formula, $N_{pe/\mu}(d)$ is the measured average number of photoelectrons per vertically crossing muon extracted from the attenuation curve previously obtained (see Section 5.2 and Figure 5.10).

To reproduce the measured distribution, the number of phoelectrons per muon is finally fluctuated according to a Poissonian distribution.

In Figure 6.8a, the signal muon spectrum in photoelectrons is shown, its resolution is of about 40%. The main contributions to it come from the fluctuations in the energy deposited in the strip and in the number of produced photoelectrons. A minor contribution comes from the different distances at which the muon crossed the strip and from the different responces of the various strip.

To confirm the validity of the conversion of the deposited energy in number of photoelectrons, the muon spectrum derived by simulation has been compared with a real one as measured in the laboratory by means of a muon telescope. The agreement is quite good, thus validating the simulation. (Figure 6.8b).

Finally, each strip is divided into 23 bins of distance to the PMT, and for each distance a corresponding value of *Npe* is extracted from the fiber attenuation curve obtained by the radioactive source. Once the distance and the number of photoelectrons are given, a trace can be extracted from the library of muons and it will be used later to calculate the detector efficiency.

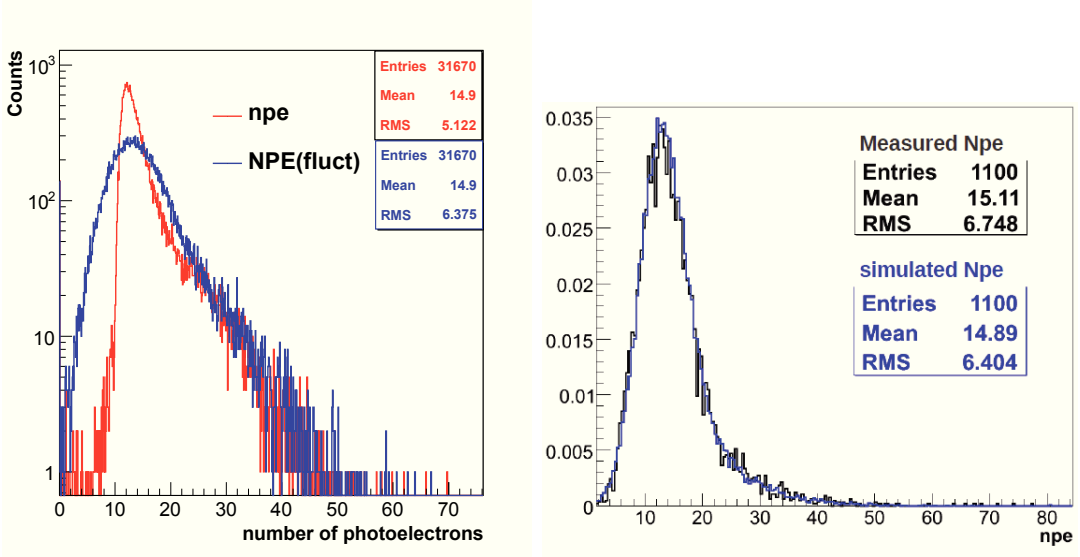

(a) (b)

Figure 6.8: (a): Distribution of npe/μ (red) and *Npe* (blue). *Npe* was extracted from a Poissonian distribution with *mean value* $= npe/\mu$. **(b):** Comparison between a measured *Npe* muon spectrum and a simulated one (normalized).

Chapter 7

Simulations

7.1 Overview on the simulation toolkit

The aim of this work is to evaluate, through simulations, the performances of the muon counters. As a first step, simulations of single particles entering the muon counters have been performed by means of the**Geant4** (**GE**ometry **AN**d **T**racking **4**) toolkit. It is a full $C++$ Monte Carlo code, originally designed to study calorimeter responses, simulating the hadronic and electromagnetic interactions of particles with matter. The energy range of validity depends on the physics and particles considered and extends roughly from 250 eV to 10 TeV. The Geamt4 toolkit includes all fundamental particles and ions. It can calculate the trajectories and determines the interactions for different physical processes, allow the access to all the information about each interaction and describe the outcome of the detectors. General features of Geant4 are the wide variety of physics descriptions through abstract interfaces, the uniform treatment of the electromagnetic and hadronic processes and the possibility to use different models to describe a physics process (Agostinelli S., 2003), (Allison J., 2006). Finally, Geant4 provides a graphical user interface which allows the user to access an interactive visualization and check the detector's geometry or the particle's tracks and interactions as it propagates on the detector. The general structure of Geant4 is constituted of a main part, which reads an input file with the settings for a particular simulation run, three mandatory parts (detector construction, physics list and primary generator action), and three optional parts (run action, event

action, tracking action), whose purpose is to allow the execution of specific actions like saving data to output files at pre-defined points in the program flow. The code was in our case specially tuned for the particle propagation through soil and to study the scintillator response when crossed by muons. Effects of the secondary particles, which may be generated both by the decay of the primary particle and the interaction of the primary particle with the surrounding medium are also considered.
As a second step, **CORSIKA** (**CO**smic **R**ay **SI**mulations for **KA**scade) (Heck D., 1998) was used to perform a detailed simulation of the particle cascade development in the atmosphere down to the ground level. At this stage information about the shower particles (particle type, energy, momentum and number of secondary particles generated for a given energy threshold), the zenithal and azimuthal angle and the shower core position are available. In the following phase, the shower particles have to be first resampled to take into account the "thinning" procedure applied in the shower simulation phase and then injected into a detector layout. These steps have been implemented in modules fully integrated in the official Auger $\overline{Offline}$ tool used for event simulation and reconstruction. Both for the simulation with single particles and simulation in showers, the data have been analyzed using the **ROOT** toolkit, an object-oriented, $C++$ based framework for data analysis.

7.1.1 The CORSIKA simulation program

The study of Extensive Air Showers, either with the aim of planning new experiments or to analyze data, requires a detailed theoretical modelling of the cascade which develops when a high energy primary particle enters the atmosphere. This can only be achieved by detailed Monte Carlo calculations taking into account all of high and low energy strong and electromagnetic interactions. CORSIKA is a detailed Monte Carlo program to study the evolution in the atmosphere of Extensive Air Showers initiated by photons, protons, nuclei, or neutrons up to 10^{20} eV. The particle transport takes into account both the energy deposited in the atmosphere and particle decay. Secondary particles are tracked explicitely

along their trajectories and their parameters are stored when reaching an observation level. This allows a detailed analysis of all features of simulated showers. When dealing with EAS simulations, the most serious problem (and the main source of systematic uncertainty in the Monte Carlo predictions) comes from our limited knowledge of hadronic interactions at high energy. Hadronic multiparticle production has to be simulated at energies exceeding by far those accessible at man-made accelerators and in phase space regions not covered in collider experiments. Five different hadronic interaction models are available in CORSIKA to simulate the hadronic interactions at high energies: the **Venus** (Werner K., 1993), **Qgsjet** (Kalmykov N.N., Ostapchenko S.S., 1993), and **Dpmjet** (Ranft J., 1995) models are based on the Gribov-Regge theory, while **Sibyll** (Fletcher R.S., 1994) (Engel J., 1992) is a minijet model. The **NeXus** (Werner K., 2001) model extends far above a simple combination of Qgsjet and Venus routines. The most recent **Epos** (Werner K., 2008) model is based on the NeXus framework but with important improvements concerning hard interactions and nuclear and high-density effect. **Hdpm** (Heck D., 1998)is inspired by findings of the Dual Parton Model (Capdevielle J.N., 1989) and tries to reproduce relevant kinematical distributions being measured at colliders. Hadronic interactions at lower energies are described either by the more sophisticated **GHEISHA** (Fesefeldt H., 1985)interaction routines, by a link to **Fluka** (Battistoni G., 2007), or the rather simple **ISOBAR** model. The **GHEISHA** model suffers from deficiencies in handling the reaction kinematics properly leading to, e.g. a notably flatter lateral distribution than the **Fluka** model. In particle decays all decay branches down to the 1% level are taken into account. For electromagnetic processes the shower program **EGS4** (Nelson W.R., 1985) or the analytical NKG (Greisen K., 1966) (Kamata K. and Nishimura J., 1958) formula may be used. It is also possible to explicitly simulate Cerenkov light on the atmosphere and to handle both electronic and muonic neutrinos and anti-neutrinos. This Monte Carlo simulation implies a 3D tracking of particles in an atmosphere with changing density and in the magnetic field of the Earth as well as a detailed implementation of particle decays and interactions over up to 14 orders of magnitude in energy. Since the number of shower particles grows proportionally to the energy, (e.g. a proton EAS with primary energy 10^{20} eV produces $\sim 10^{11}$ particles at the maximum of

its development), only a small fraction of particles can be tracked and the whole shower is reconstructed from a sample. This method, which drastically reduces comptution demand, is called *thinning* (Hillas A.M., 1985). By this technique all particles with energy E below an adjustable fraction of the primary energy E_0 (called *thinning level* $E_{th} = E/E_0$) which emerge from an interaction are treated by the thinning algorithm. Only one of these particles is followed and an appropriate weight is given to it, while the other particles below the thinning level are dropped. At extreme particle densities (several 1000 - 10000 per m^2), it is very efficient to track only few high weighted particles instead of all the individual particles. The thinning algorithm keeps the few relevant particles and removes the very abundant particles that are predicted not to give an important contribution to the total extensive air shower. By using a typical weight limitation of 100-10000 the computation demands are reduced almost correspondingly. An important drawback of the thinning technique has to be taken into account: since the number of particles at ground is reduced, the Poissonian statistical fluctuations are artificially enhanced, especially in the regions not too close to the core where few particles are present. To overcome this problem, the so-called *unthinning technique* is used (Billoir P., 2008). The idea is that of using all shower particles on an area $A_{sampling}$ much larger than the detector one A_{det}, assigning them a weight reduced by a factor $A_{det}/A_{sampling}$.

7.1.2 The Offline Framework

The $\overline{Offline}$ software framework of the Pierre Auger Observatory provides an infrastructure to support a variety of distinct computational tasks necessary to analyze data gathered by the observatory (Argiro' S., 2007). The software must support simulation and reconstruction of events using surface, fluorescence and hybrid methods, as well as simulation of calibration techniques and other ancillary tasks such as data preprocessing. The $\overline{Offline}$ framework must also handle a number of data formats in order to deal with event and monitoring information from a variety of instruments, as well as the output of air shower simulation codes. It has been written entirely in C++. The $\overline{Offline}$ framework comprises three principal parts: a series of *modules* (C++ classes), responsible for the simulation

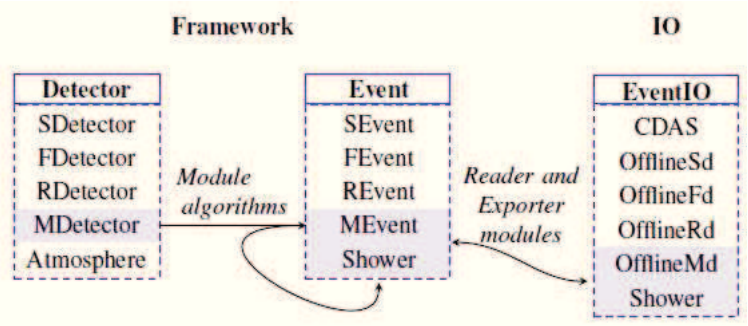

Figure 7.1: General structure of the $\overline{Offline}$ framework. Simulation and reconstruction tasks are broken down into modules. Each module is able to read information from the detector description and/or the event, process the information, and write the results back into the event.

and reconstruction tasks, which can be assembled and sequenced through instructions provided in a XML file. Each of these modules is able to read information from the detector description and/or the event; an *event* structure through which modules can relay data to one another and which accumulates all simulation and reconstruction information. It contains all raw, calibrated, reconstructed and Monte Carlo data. A series of utilities supports the multi-format reading and writing; a *detector* structure describing the configuration and performance of the observatory as well as atmospheric conditions as a function of time.

These ingredients are depicted in Figure 7.1.

The simulation of events observed by the Auger detectors typically involves the creation of a shower using a Monte Carlo generator (Corsika, Aires, Conex and Seneca are supported), the simulation of the response and triggering of the surface tanks hit by the particles arriving at ground level, and the simulation of the response and triggering of the fuorescence telescopes hit by the light emitted along the shower track. Finally, event building and export to various formats can be performed. Detector simulations can be broken down into a sequence of steps, each of which is generally encapsulated within a separate module. All these steps are executed sequentially as listed in a so-called *Module Sequence*. Run-time control over the module sequence is afforded through a *run controller* which invokes the various processing steps within the modules according to a set

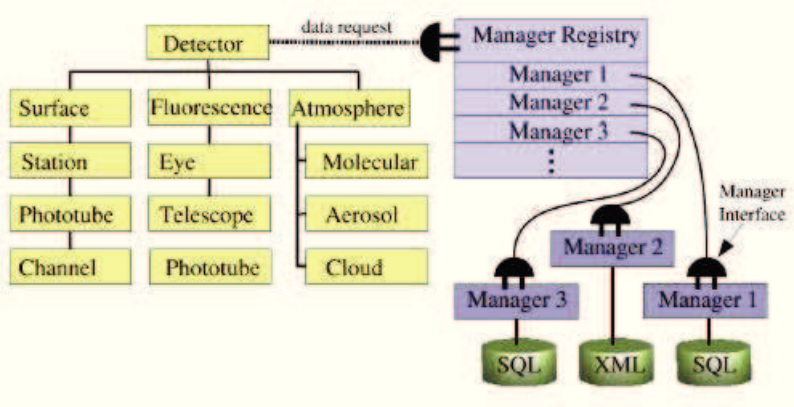

Figure 7.2: Schematic design of the $\overline{Offline}$ detector interface.

of externally provided instructions. The detector interface is organized following the natural hierarchy of the Auger detectors, as depicted in Figure 7.2. It allows to retrieve information about the detector configuration and performance at a particular time. These data are typically stored in XML files for static detector information, and in MySQL databases for time-varying info, such as monitoring and calibration data. The data queries are passed by this interface to a registry of so-called *managers*, each of which is capable of extracting a particular sort of information from a particular data source. The detector interface is also equipped to support a set of plug-in functions, called *models*, which can be used for additional processing of data retrieved through the detector. These are used primarily to interpret atmospheric monitoring data. The $\overline{Offline}$ is provided with a collection of utilities (some of them are external tools, others are developed inside the Auger collaboration), including a Xerces-based XML parser, an error logger, various mathematics and physics services, testing utilities, a geometry package and a set of foundation classes to represent objects such as signal traces, tabulated functions and particles.

7.1.3 A module to simulate the AMIGA detector

In this section, we will illustrate a *Module Sequence* for simulating the AMIGA detector. To this aim, we developed a module (implemented in the C++ class

```
<sequenceFile>

   <enableTiming/>

   <moduleControl>
     <loop numTimes="unbounded" pushEventToStack="yes">

       <module> EventFileReaderOG </module>

       <loop numTimes="1" pushEventToStack="yes">

         <module> EventGeneratorOG </module>
         <module> ShowerRegeneratorAG </module>
         <module> GroundPropagatorTO </module>
         <module> MdEdepSimTO </module>


       </loop>
     </loop>
   </moduleControl>
 </sequenceFile>
```

Figure 7.3: ModuleSequence.xml for AMIGA (Infill+Md) simulation.

MdEdepSimTO) to estimate the mean number of photoelectrons generated by the PMT for a particle that deposits a specific amount of energy at a given distance. Furthermore, the implementation of different counting strategies (see Section 8.1.4) at the level of each individual strip was considered.

The *Module Sequence* to simulate the AMIGA detector is listed in Figure 7.3.

The first step to start simulating event is to read a shower from the CORSIKA outputs using the (*EventFileReaderOG* module) and locate its impact point within the array by means of the (*EventGeneratorOG* module). Several possibilities are left to the user for the choice of the event core, that can be assigned close to a particular tank, randomly distributed over all the array size, in the eye/telescope field of view (suited for FD and hybrid simulations). In our case, the shower core will be always associated to the infill Water-Cherenkov detector labelled as "734". The *ShowerRegeneratorAG* module performs the shower unthinning. A statistical procedure is applied to resample particles over a specified detector area: shower particles outside this area are not simulated. In the cor-

```
<?xml version="1.0" encoding="iso-8859-1"?>

 <!-- Configuration of Module ShowerRegenerator -->


<MdShowerRegenerator xmlns:xsi="http://www.w3.org/2001/XMLSchema-instance"
xsi:noNamespaceSchemaLocation='/home/maldera/DPA/trunk_verison/offline/share/auger-offline/config/MdShowerRegenerator.xsd'>


<DistanceCuts>
 <InnerRadiusCut unit="m"  use="no">  50.0 </InnerRadiusCut>
 <OuterRadiusCut unit="km" use="yes"> 100.0 </OuterRadiusCut>
</DistanceCuts>

<!-- Particle energy cuts -->
<EnergyCuts>
 <ElectronEnergyCut unit="GeV"> 0.1  </ElectronEnergyCut>
 <MuonEnergyCut     unit="GeV"> 0.1 </MuonEnergyCut>
 <PhotonEnergyCut   unit="GeV"> 0.1  </PhotonEnergyCut>
 <HadronEnergyCut   unit="GeV"> 1000 </HadronEnergyCut>
 <MesonEnergyCut    unit="GeV"> 1000 </MesonEnergyCut>
</EnergyCuts>

<!-- Algorithm parameters -->
<AlgorithmParameters>
 <DeltaROverR> 0.1 </DeltaROverR> <!-- dimensionless (dR/R) -->
 <DeltaPhi unit="radian"> 0.15 </DeltaPhi>
 <HorizontalParticleCut> 1e-3 </HorizontalParticleCut>
 </AlgorithmParameters>

<!-- Scale the number of muons by some arbitrary factor -->
<MuonWeightScale> 1 </MuonWeightScale>

<!-- inject only muons into the ground -->
<OnlyMuons> 1 </OnlyMuons>

</MdShowerRegenerator>
```

Figure 7.4: Xml configuration file of the module *ShowerRegeneratorAG*.

responding xml configuration file, the user may set the values of the position of the sampling area and the kind of particles that are allowed to be propagated through the soil (using <DeltaROverR>, <DeltaPhi>, and <OnlyMuons> tags (see Figure 7.4)).

The muons can also be scaled by a configurable factor with <MuonWeightScale>. Once each station has its associated list of particles on-ground, they are propagated using Geant4 through the soil by *GroundPropagatorTO* module. The energy deposited in the scintillator by the particle can be evaluated in two different ways: (i) an algorithm using the track length of the particle crossing the strip, or (ii) a full Geant4 calculation. We have used the second method.
Given the amount of energy deposited and the crossing point along the strip, the number of photoelectrons arriving to the PMT can be estimated.
A signal shape corresponding to the input can finally be extracted from the muon trace library. An example of the superposition of signals generated by an impinging particle, is shown in Figure 7.5. As a final step, each trace will be

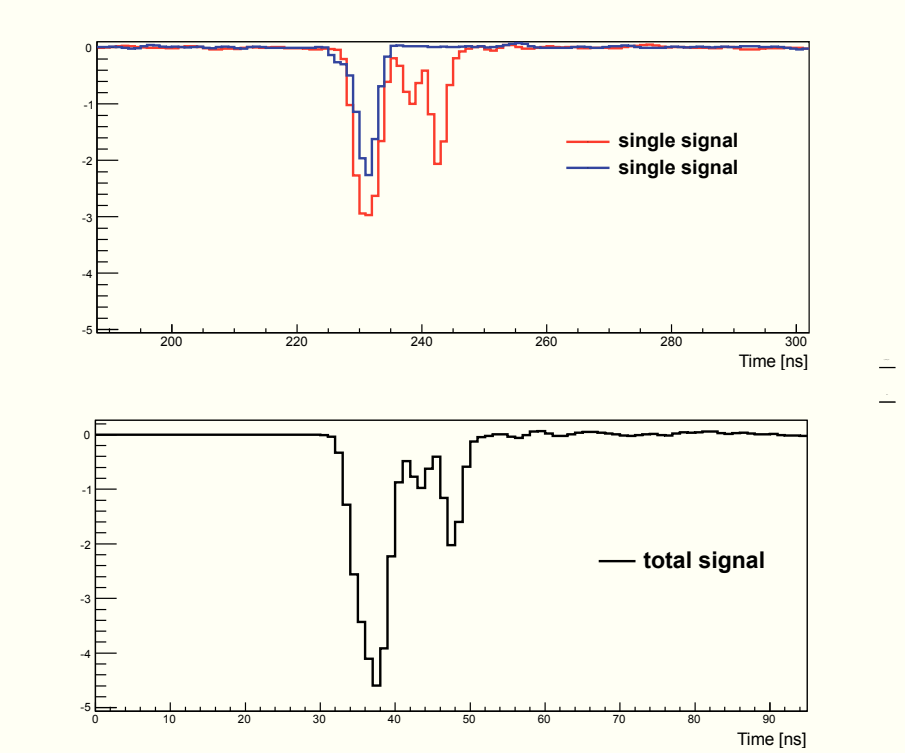

Figure 7.5: Construction of simulated pulses. The total pulse (bottom) is obtained as superposition of single signals (top) generated by particles which hit the same scintillator strip.

discriminated and digitized, as explained in Section 6.2. In the following, the simulation will be used to study and discuss the different strategies to be applied for the muon counting.

Chapter 8

Results of the simulations

The main part of this thesis is dedicated to the simulation studies that have been performed to check the performances of the AMIGA muon counters. The simulations are based on the Geant4 and the CORSIKA toolkits. This chapter is divided into two sections. The first section will be dedicated to the simulation of single particle beams of muons, electrons and gamma. The second section will be dedicated to the simulations with EAS.

8.1 Simulations with single particle beam

Using the Geant4 package, already described in Section 7.1, individual particles, muons, electrons and photons, are propagated into the soil down the scintillator slab. This simulation will allow us to derive the detection probability, to evaluate the punch-through, that is the amount of electromagnetic component surviving to such depth and finally to obtain the efficiency of muon detection of the AMIGA scintillator. Following the project design, a 10 m^2 scintillator counter was included in the simulation, at a depth of 2.3 m underground. A complete study was performed in order to derive the soil composition at the experiment site (Canet C., 2008): the average values are shown in Table 8.1; from these investigation, an average value of 2.38 gcm^{-3} was derived for the soil density.

Among the different physical processes available in Geant4 to describe the interactions of particles with matter, the following were considered: for photons the Compton scattering, gamma conversion and photoelectric effect; for electrons

Material	Percentage [%]
SiO_2	64.37
Al_2O_3	12.06
Fe_2O_3	5.62
TiO_2	0.5
CaO	4.91
MgO	2.52
K_2O	1.93
Na_2O	4.27
H_2O	3.82

Table 8.1: Table of the minerals in Malargue soil used in the simulation.

and positrons, the processes of ionization, bremsstrahlung and multiple scattering. Finally, for the muons, ionization, bremsstrahlung, pair production, decay processes and multiple scattering were considered. For a complete description of these processes in the Geant4 framework, see (Geant4 Collaboration, 2010).

Figure 8.1 shows the penetration depth of vertical muons of 1GeV for different density values ρ. The value of 2.65 g/cm^3 is equivalent to the density of the standard rock (Z = 11, A = 22) while 1.38 g/cm^3 is equivalent to one with the atomic number Z = 11 and the mean ratio A/Z = 0.5. As can be seen, increasing the soil density value, the probability for the muons to reach the detector decreases, going from 99% to almost 0% for ρ going from 1.8 to 2.65 g/cm^3.

It is not the purpose of this work to simulate in detail all the elements forming the module and their relevant physical processes. Our aim is to study the detector response starting with the energy deposited by particles into the scintillator strips. For this aim, a module with 32 strips of dimensions 800 × 4.1 × 1 cm was used (Figure 8.2). The same results were obtained using an ideal detector formed by 250 strips (to avoid border effects). The particle type, energy, zenith angle θ and azimuth, and the location of the emission point are set in an input file. The position of primary particle is extracted randomly on a box of 82 × 82 mm centered on the module. We use this configuration because we want to simulate a uniform distribution of impact points on the strips.

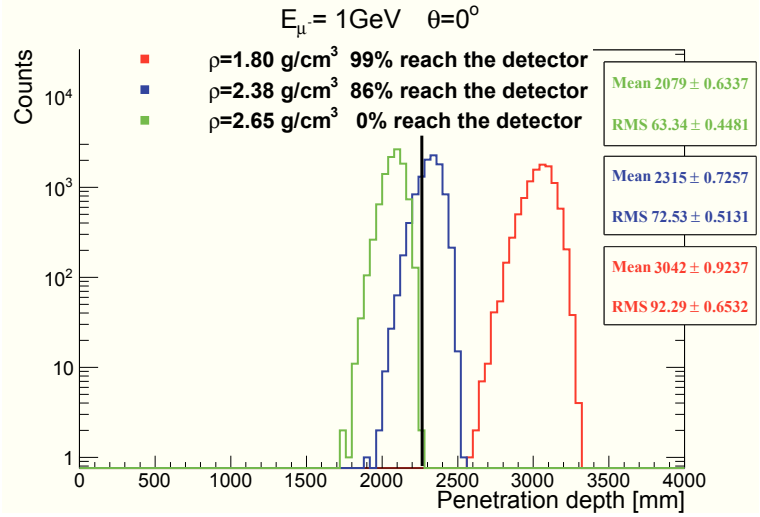

Figure 8.1: Penetration depth of muons for different values of the soil density. The black line indicates the position of the scintillator module. The percentages of muons reaching the detector are also shown.

For each event in a simulation run, an output file is generated, to store the simulation results. In particular, for each simulated particle, its type, the hit strip number, the kinetic energy, the secondary particles type, the time, the direction cosines and the coordinates of the impact point, as well as the deposited energy into the strip, are stored in the output file.

To start, we simulated 100000 vertical muons with kinetic energies of 1 and 10 GeV. When a charged particle enters the scintillator, it leaves a wake of excited molecules. The light yield inside a scintillator is proportional to the energy deposited by the particle. Typical values for a standard plastic scintillator are 8-10 photons per deposited keV (Eidelman P. S, 2004). Figure 8.3 shows the histograms of the energy deposited on the scintillator strips, either by primary muons or by the secondary particles generated by muons. Approximately 90% of the 1 GeV muons reaches the detector, while all 10 GeV muons, reach the strips, with a slight over-counting due to the possibility that some muons cross two adjacent strips. As can be seen, the strips crossed by a muon present higher values of energy deposited. The muons leave about 2.6 and 1.9 MeV respectively, while the secondary particles tend to deposit less energy (about 0.6 MeV), and

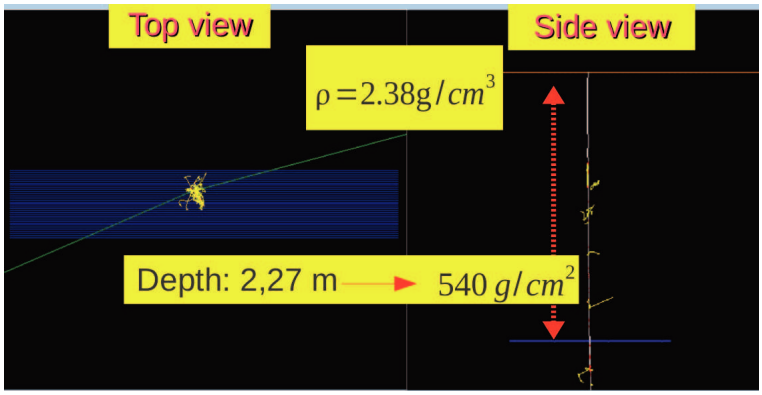

(a)

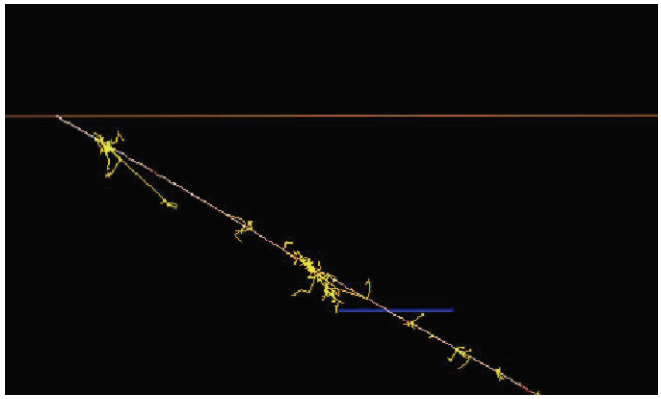

(b)

Figure 8.2: (a): Top and side view of vertical muons; **(b):** Inclined particle beams ($\theta = 60°$). For inclined particles, the emission point is shifted in the y-direction to ensure that the particle traverses the scintillator plane always in the center. The module (blue color) is buried at a depth of ∼2.3 m corresponding to 540 gcm^{-2} with soil density of 2.38 gcm^{-3}.

both peaks are clearly distinguishable.

The distribution of the particles on the XY-plane of the module is shown. Limiting ourselves to the case of vertical muons with kinetic energy of 1 GeV, one can observe the distributions of primary muons (Figure 8.4a) and secondary particles generated by muons (Figure 8.5a) in the XY-plane at a depth of 2.3 m. In both cases, there is a symmetry in the plane, and furthermore, the distribution appears to be centered along the incident direction of the primary particle in the center of the module.

As can be seen, the distribution of muons turns out to be narrower than that of the secondary particles, due to the fact that the muons travel in an almost straight direction, and therefore are very close to the direction of their emission point. On the contrary, secondary particles, undergo many scattering processes, therefore their trajectory is deflected relative to the direction of the emission point and for this reason the distribution is wider. In Figure 8.4(b,c) and Figure 8.5(b,c), the projections onto the x-axis and y-axis are shown.
An analysis on the type of secondary particles generated by the primary muon has been performed. In general, during the propagation through the soil, a muon can decay or interact with the protons of the nucleus according to the weak reaction ($\mu^- + p \rightarrow \nu_\mu + n$). The neutron can be absorbed and as a result protons, alpha particles, etc. will be emitted. From the collisions of protons with nuclei π^+ and π^- are obtained which decay in μ^+ and μ^-. Since antimuons decay into positrons, these positrons may annihilate in the soil and thus produce photons with an energy in the order of magnitude of 100 keV, which is approximately the minimum energy needed to produce a single photoelectron in the cathode of the PMT. The presence of neutral particles does not affect the analysis since they do not produce any signal on the scintillator strips. The gamma is quickly converted to an electron-positron pair which, in turn, produces new gammas by bremsstrahlung, which then starts an electromagnetic shower. Among these particles, there are also neutrinos and antineutrinos produced by the decay of muons and antimuons, into electrons and positrons. In Figure 8.6 the particles produced by vertical primary muons of 1 and 10 GeV are shown abundances of the secondary.

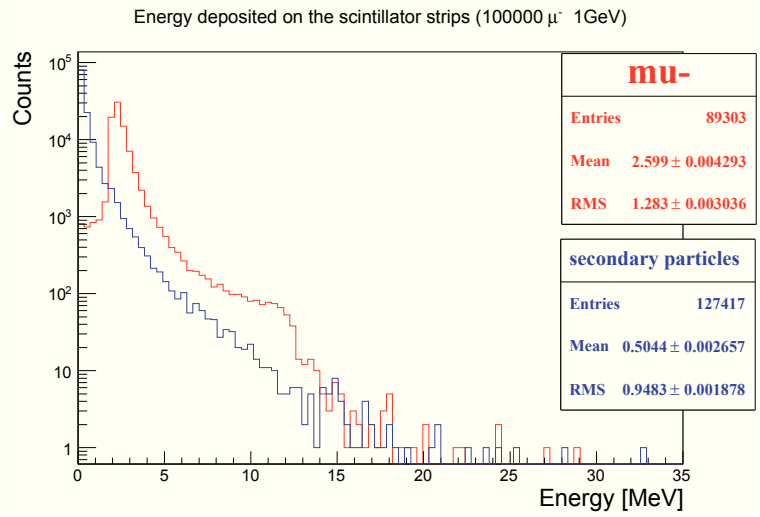

(a)

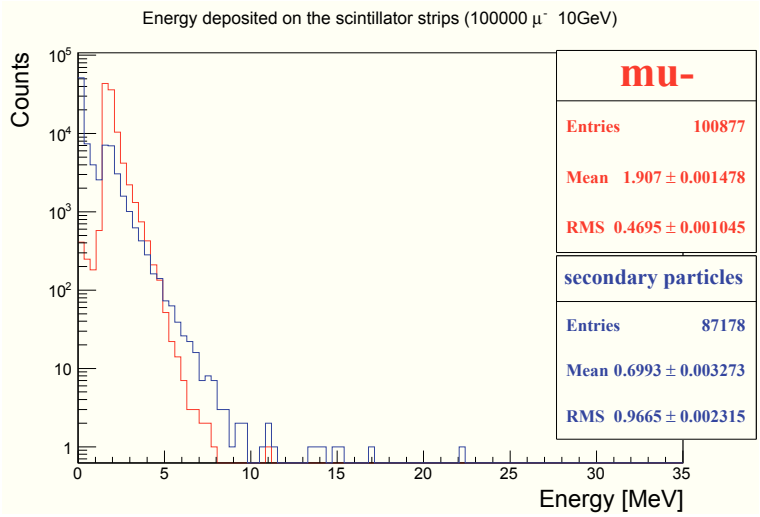

(b)

Figure 8.3: Total energy deposited (E_{dep}) on the scintillator strips. In red the E_{dep} by muons and in blue the E_{dep} by the secondary particles. **(a):** Primary vertical muons of 1 GeV; **(b):** Primary vertical muons of 10 GeV.

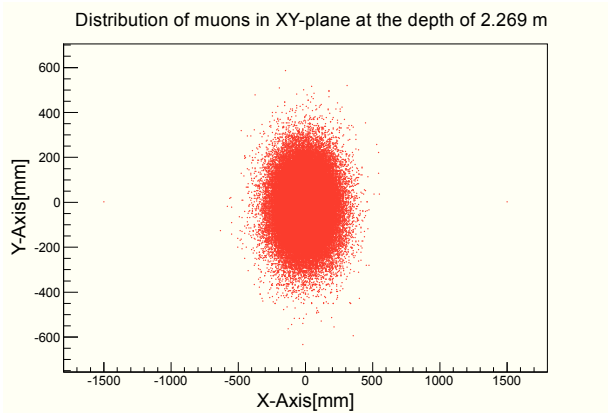

(a)

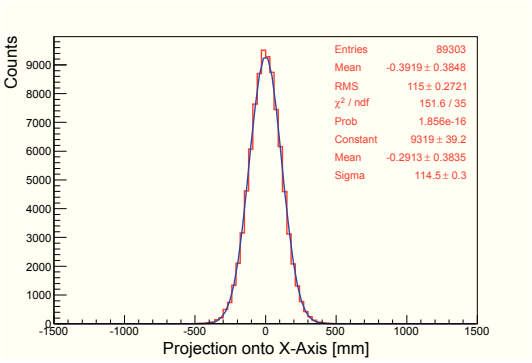

(b)

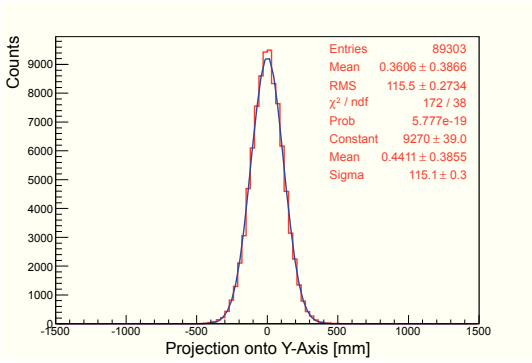

(c)

Figure 8.4: (a): Distribution of the primary muons in the XY-plane of the module; **(b):** Projection onto the X-Axis; **(c):** Projection onto the Y-Axis.

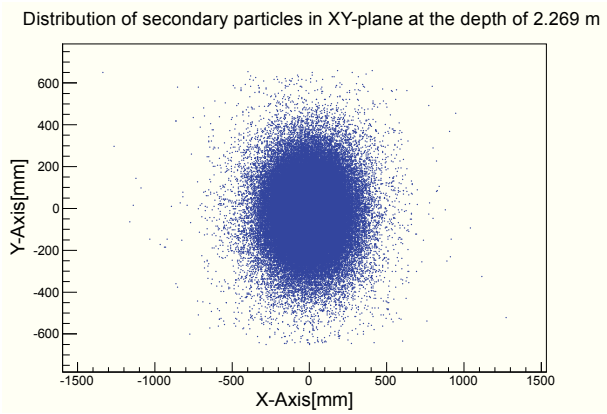

(a)

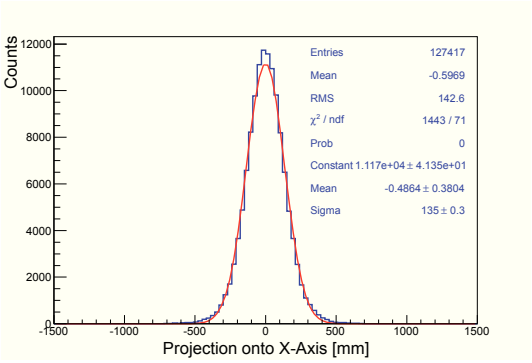

(b)

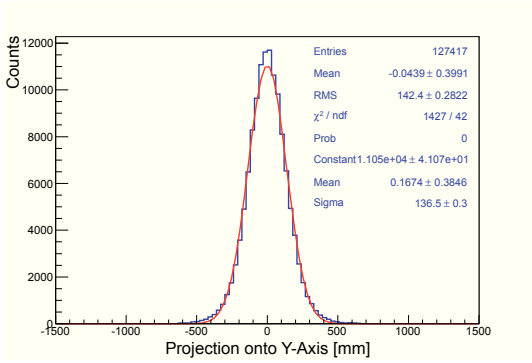

(c)

Figure 8.5: (a): Distribution of the secondary particles in the XY-plane of the module; **(b):** Projection onto the X-Axis; **(c):** Projection onto the Y-Axis.

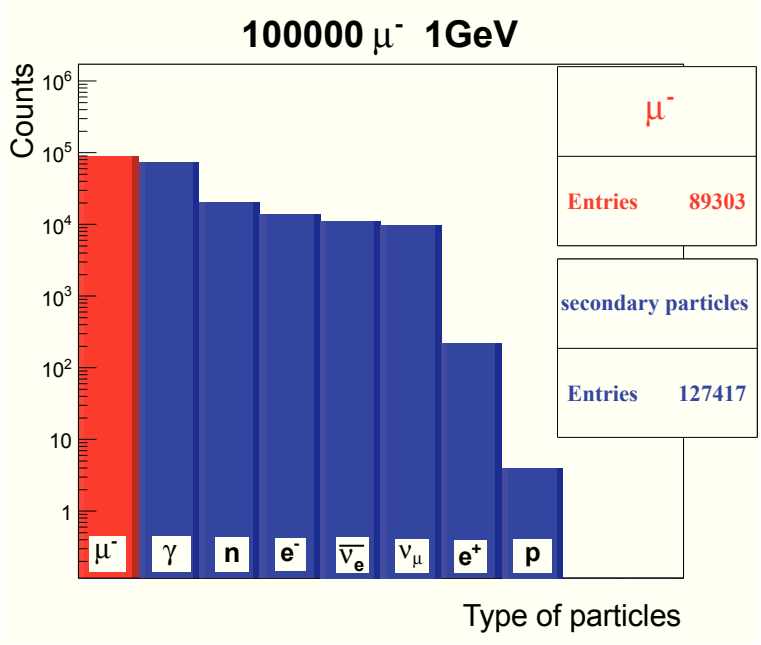

(a)

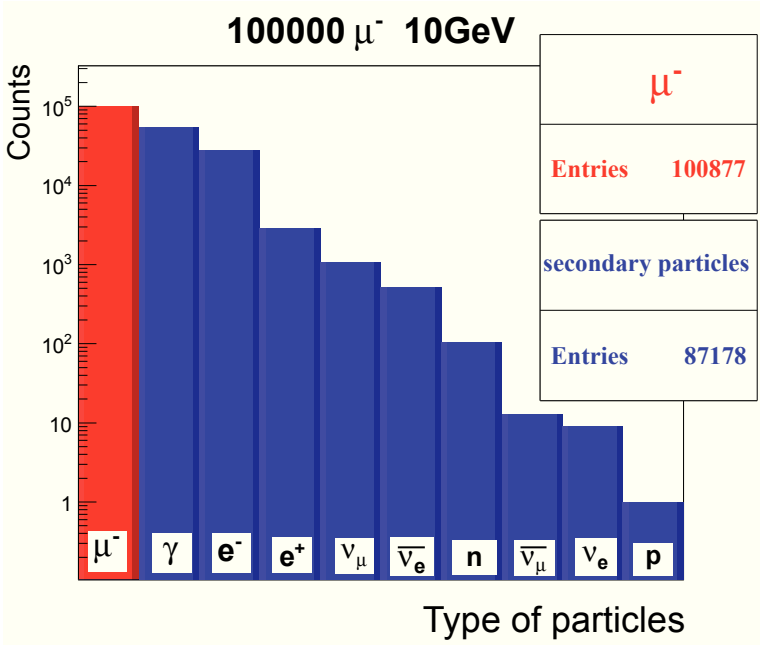

(b)

Figure 8.6: Histograms of the secondary particles produced by vertical primary muons based on the analysis of 100000 events. The primary muons are shown in red while the secondary particles are in blue. **(a):** Primary vertical muons of 1 GeV; **(b):** Primary vertical muons of 10 GeV.

8.1.1 Propagation of μ^-, γ and e^- underground

The penetration depth of the primary muon has been calculated using the z-coordinates of the endpoints of the respective track and is shown in Figure 8.7 for vertical primary muons with energies between 0.8 GeV and 1.5 GeV. From the analysis, it is possible to see that, no particles reach the detector for the energies below 0.8 GeV, since the muons are absorbed in the soil above the detector. For energie $\geq$ 1.5 GeV, almost all of particles reach and go beyond the depth of the detector.

The penetration depth of the primary muons for energies between 0.8 GeV and 10 GeV is calculated evaluating the 0.95-quantile of the distribution that is the value of the penetration depth for which 95% of all events have a smaller value. The 0.95-quantile gives us a value larger than the mean penetration depth. The penetration depth has been plotted against the kinetic energy of the primary muon in Figure 8.8. Each point is based on the analysis of 10000 events with the corresponding RMS value. The data points show a linear dependance on the kinetic energy of the primary muon in whole the considered range.

8.1.2 Detection probability

Muons lose their energy predominantly due to ionization. They are not affected by strong interaction and, therefore, they pass through the atmosphere almost undisturbed. Although only $\sim$ 4% of the particles produced in an EAS belong to the muonic component, around 80% of the particles at sea level are muons. The remaining 20% is composed of electrons and photons, and minimally by protons, kaons and nuclei. These particles, for sufficiently high energies, may pass through the soil above the detector, and produce a signal in the detector. The interaction processes of these particles with matter are different than those of muons. High-energy electrons predominantly lose energy in matter by bremsstrahlung, and high-energy photons by e^+e^- pair production. At low energies electrons and positrons primarily lose energy by ionization, although other processes contribute. While ionization loss rates rise logarithmically with energy, bremsstrahlung losses rise nearly linearly (fractional loss is nearly independent of energy), and dominates above a few tens of MeV in most materials. In this section we discuss

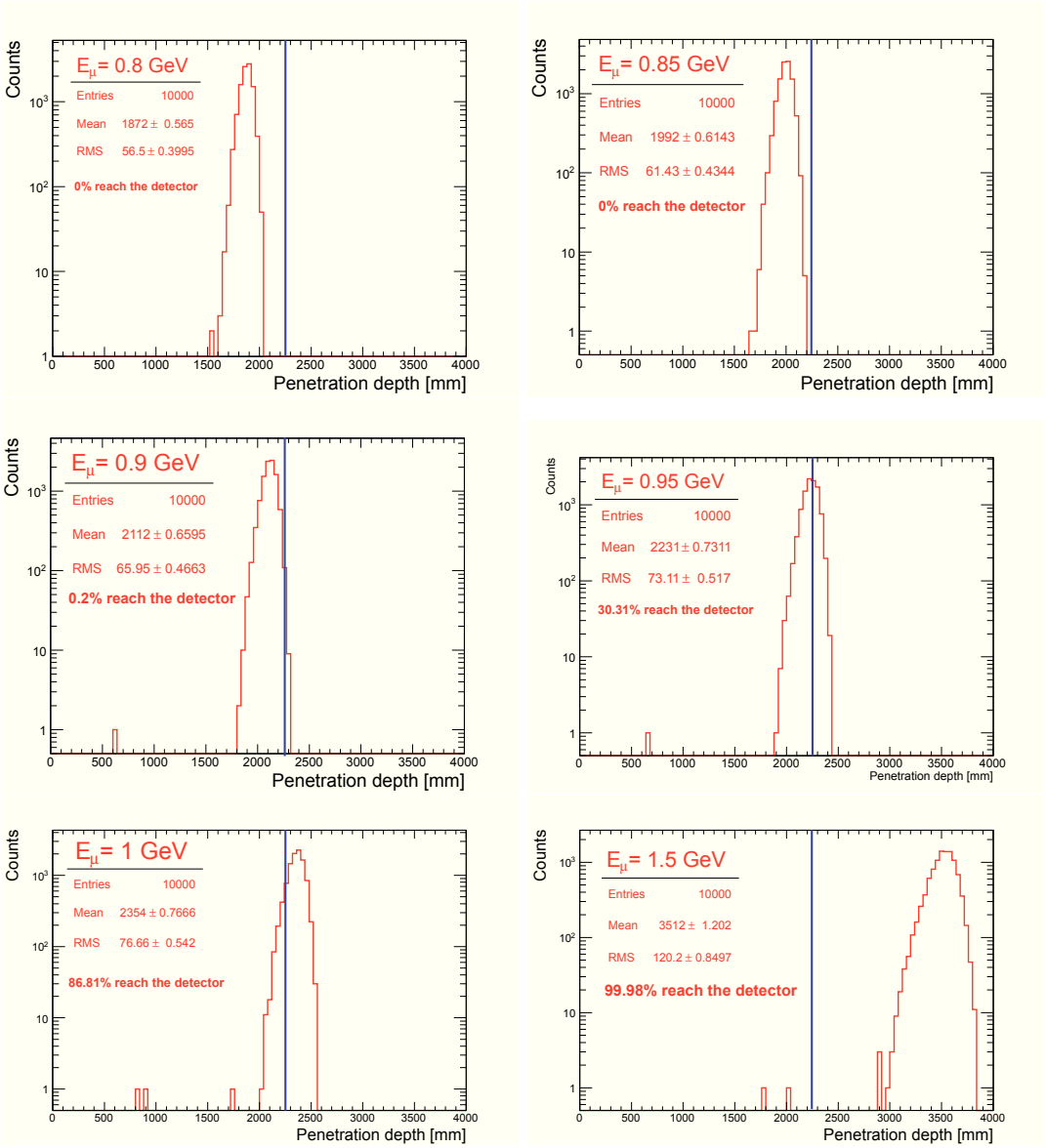

Figure 8.7: Histogram of the penetration depths for vertical muons of kinetic energy between 0.8 GeV and 10 GeV. Each histogram is based on the analysis of 10000 events. The blue line indicates the position of the scintillator module. The percentages of muons reaching the detector are also shown.

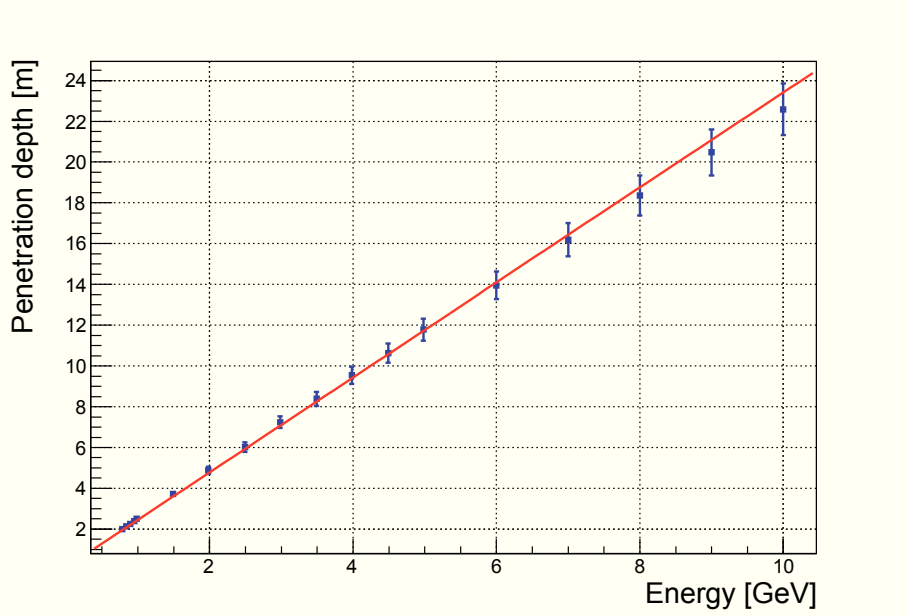

Figure 8.8: 0.95 quantile of the penetration depth as a function of the kinetic energy of the primary muons. Each point is based on the analysis of 10000 events with the corresponding RMS value.

the detection probability of the particles. Simulation studies considering muons, photons and electrons were performed. Figure 8.9 shows the fraction of detected events vs the kinetic energy of the muons, ie the probability of the particles to reach the detector. The simulations were performed for vertical and inclined particles ($\theta = 30°$ and $\theta = 60°$). Each point is the average of 10000 events with the corresponding RMS error (very small and covered by the marker size). The energy range was chosen from 0.8 to 4 GeV.

This detection probability can be parametrized as a function of energy and zenith angle, using the function

$$F(E,\theta) = \frac{1}{e^{\frac{P_0(\theta)-E}{P_1(\theta)}} + 1} \tag{8.1}$$

with parameters

$$\begin{cases} P_0(\theta) = \frac{941.7}{cos(\theta)} \\ P_1(\theta) = \frac{60.51}{cos(\theta - 0.062)} - 34.52 \end{cases} \tag{8.2}$$

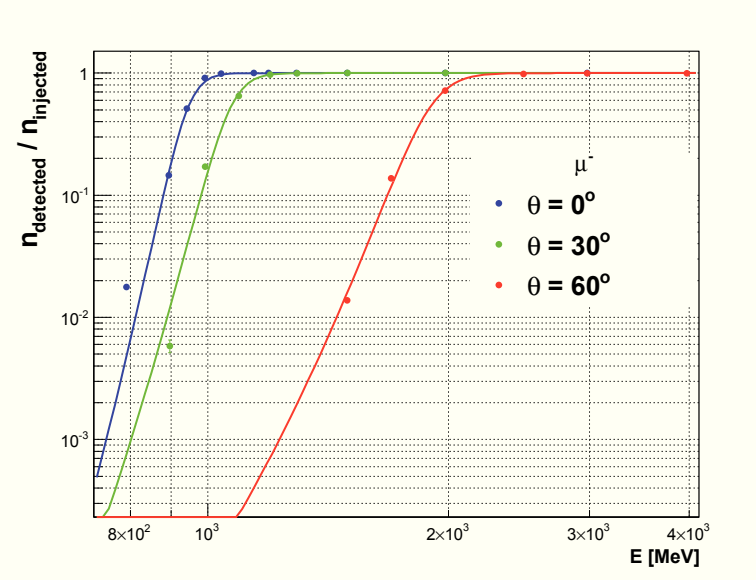

Figure 8.9: Fraction of detected events vs energy for vertical and inclined muons.

With the increasing of the zenith angle, due to the increased path of the particles in the soil, more energy will be needed to reach the detector. Full detection efficiency is obtained for inclined muons ($\theta = 60°$) at energies greater than 3 GeV, while only 1 GeV is enough for the vertical case.
Figure 8.10 shows the percentage probability of detected events in the case of gamma and electrons. The error on each point is not shown because it turned out to be small compared to the used scale. As can be seen, only vertical gamma and electrons of 40 GeV are able to reach the buried detector with a probability of 100%.

In this case, the fractional probability is parametrized as

$$F(E,\theta) = \frac{10^{P_3(log(E))}}{k(\theta)} \tag{8.3}$$

where P_3 is 3rd degree polynomial, with parameters

$$\begin{cases} P_0 = -7.042 \\ P_1 = 2.279 \\ P_2 = 0.080 \\ P_3 = -0.033 \end{cases} \tag{8.4}$$

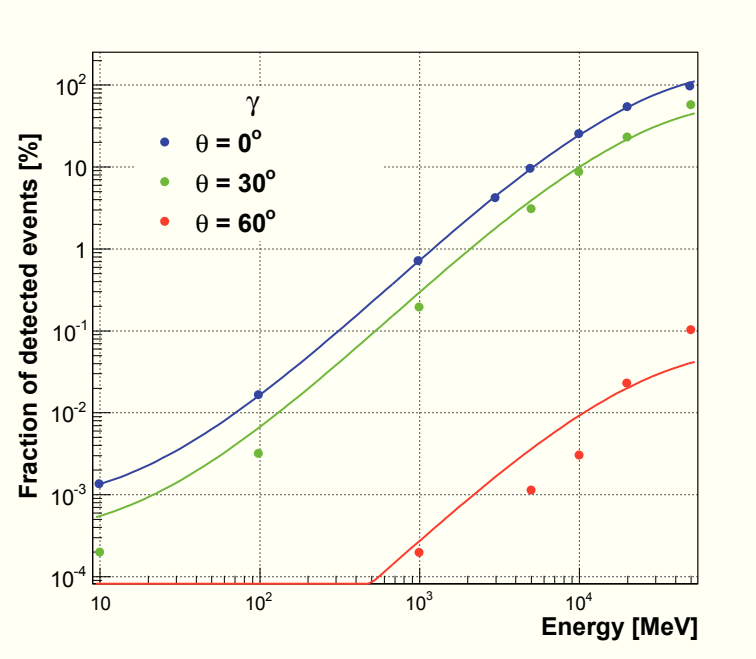

(a)

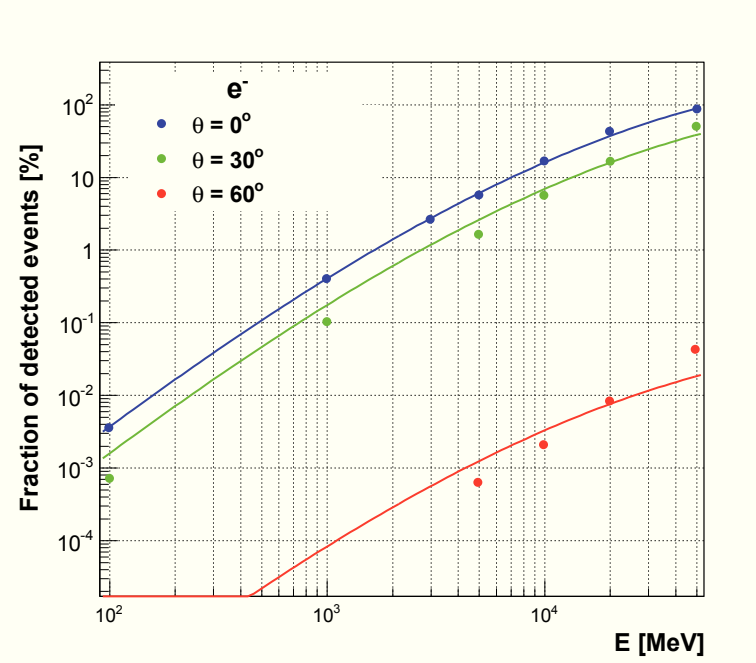

(b)

Figure 8.10: Probability of detected events vs energy for primary gamma and electrons. **(a):** Gamma; **(b):** Electrons.

and k(θ) includes the angular dependence and is given by

$$k(\theta) = e^{-7.92+0.27\theta} + 1 \tag{8.5}$$

in the case of electrons, and

$$F(E,\theta) = \frac{10^{P_3(log(E))}}{k(\theta)} \tag{8.6}$$

with parameters

$$\begin{cases} P_0 = 2.726 \\ P_1 = 0.978 \\ P_2 = 0.949 \\ P_3 = -0.112 \end{cases} \tag{8.7}$$

and

$$k(\theta) = e^{-7.13+0.025\theta} + 1 \tag{8.8}$$

in the case of gamma.

At ground level, the hadronic component is comprised mostly of protons, neutrons and pions. Since the hadronic component is limited to the area very close to the shower core, the contribution of hadrons can be assumed to be negligible. For this reason, these particles were not considered in our simulations.

8.1.3 Studies on the cluster width

The goal of the AMIGA scintillator modules is to directly count muons. However, single hits in the counters can appear clustered, that is consecutive strips can be hit simultaneously. These "clusters" could be e.g. due to small electromagnetic showers produced locally by muons, or by inclined muons hitting more strips. In order to investigate them and study their origin, we simulated 100000 muons, both in vertical and inclined directions. The primary muons are launched towards the module center, in correspondence with the strip 16. Different energy thresholds ($E_{dep} > 100\ keV,\ 300\ keV,\ 500\ keV$) have been considered. These distributions have been performed for muons of 3 and 10 GeV, with $\theta = 0°$, $\theta = 30°$ and $\theta = 60°$. Figures 8.11 and 8.12 show the distributions of the hit strips, expressed in percentage.

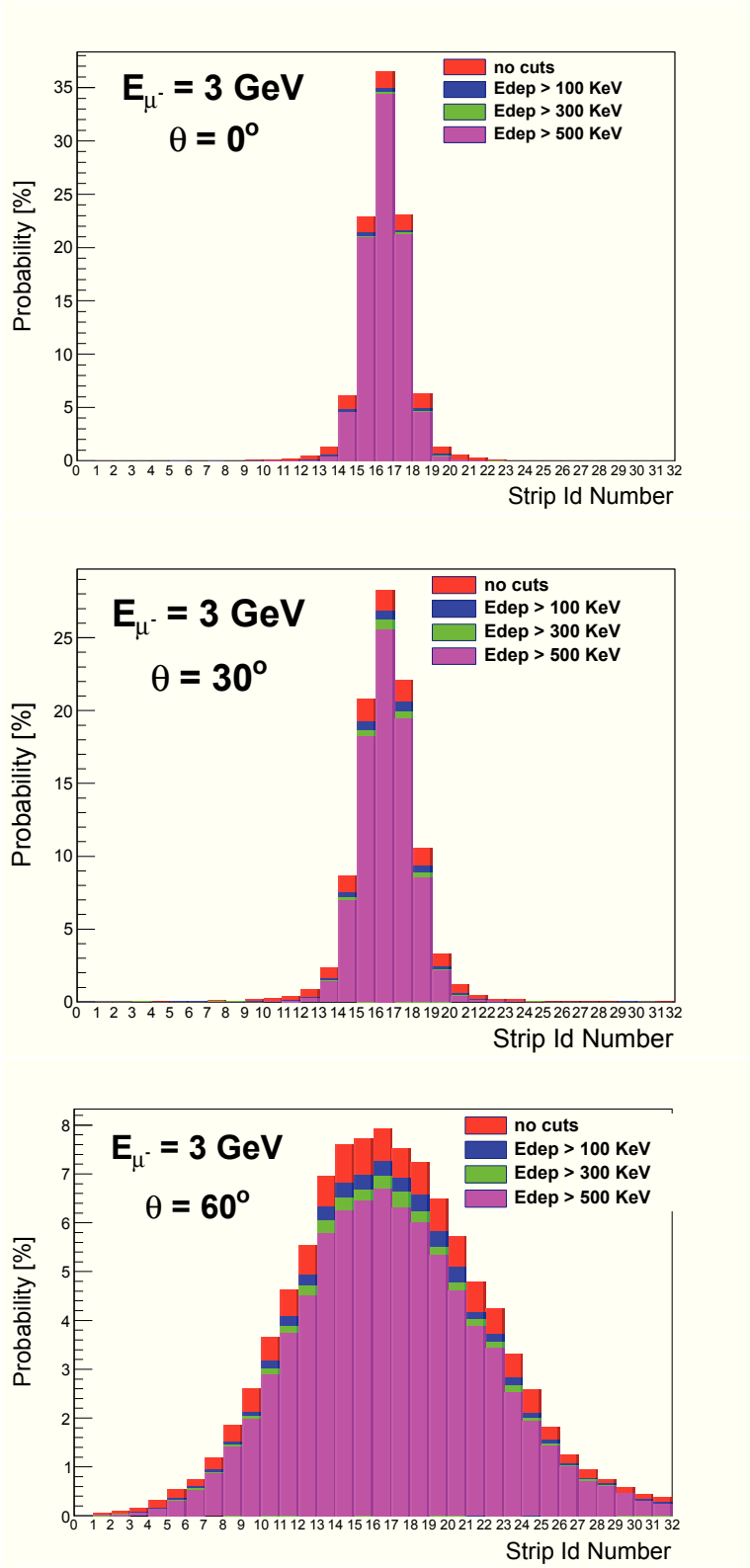

Figure 8.11: Probability of the hit strips for muons of 3 GeV: **(top):** Vertical muons ($\theta = 0°$); **(middle):** inclined muons ($\theta = 30°$); **(bottom):** inclined muons ($\theta = 60°$).

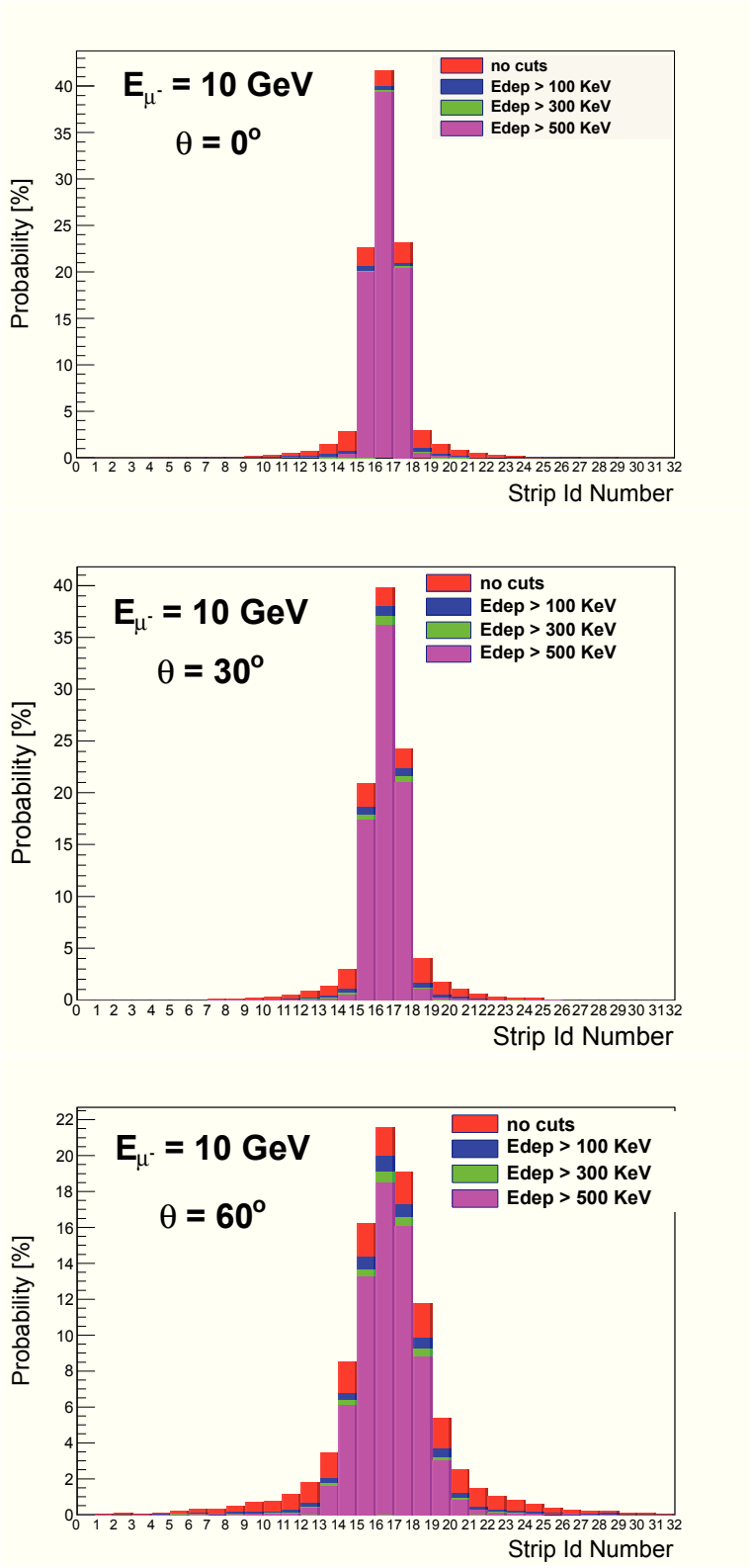

Figure 8.12: Probability of the hit strips for muons of 10 GeV: **(top):** Vertical muons ($\theta = 0°$); **(middle):** inclined muons ($\theta = 30°$); **(bottom):** inclined muons ($\theta = 60°$).

As can be seen for both the energy values, the probability to hit the central strip decreases when the zenith angle increases, which means that more strips are hit. The corresponding hit strip multiplicity is shown in Figures 8.13, 8.14. These results give information on how many strips are hit by the primary and secondary particles for each event. The number of hit strips (for an incoming muon) increases with the zenith angle, and it decreases with the energy threshold. For example, a greater multiplicity is observed in the case of inclined muons ($\theta = 60°$) and without any cut in deposited energy.
The width of cluster is shown in Figures 8.15 and 8.16, being it defined as the distance between the strips hit by a secondary particle and the strip hit by muon primary. In this way one can study in spatial terms the effect of the generated secondary particles by the muon, and then see how many scintillator strips on the plane of the module are involved for each event. Comparing the histograms for the different energies, it is found that the width of the distributions is highly dependent on the energy thresholds and the zenith angle: as an example in the case of vertical muons and no cut in deposited energy, the maximum cluster size ranges from 13 at 3 GeV to 15 at 10 GeV. It is important to note, however, that in all cases the majority of events exhibits a cluster size of 1, which means that only the primary muon passes through the detector.

8.1.4 Detector efficiency

The efficiency measures the ability of a detector to detect the particles that pass through it. We can define the detector efficiency as

$$\varepsilon = \frac{n}{N} \tag{8.9}$$

in which, N is the injected particles number, and n those observed.

In order to determine the efficiency, two fundamental ingredients have been used:

- the light attenuation profile obtained in Section 5.2;
- the library of muon traces obtained in Section 6.2;

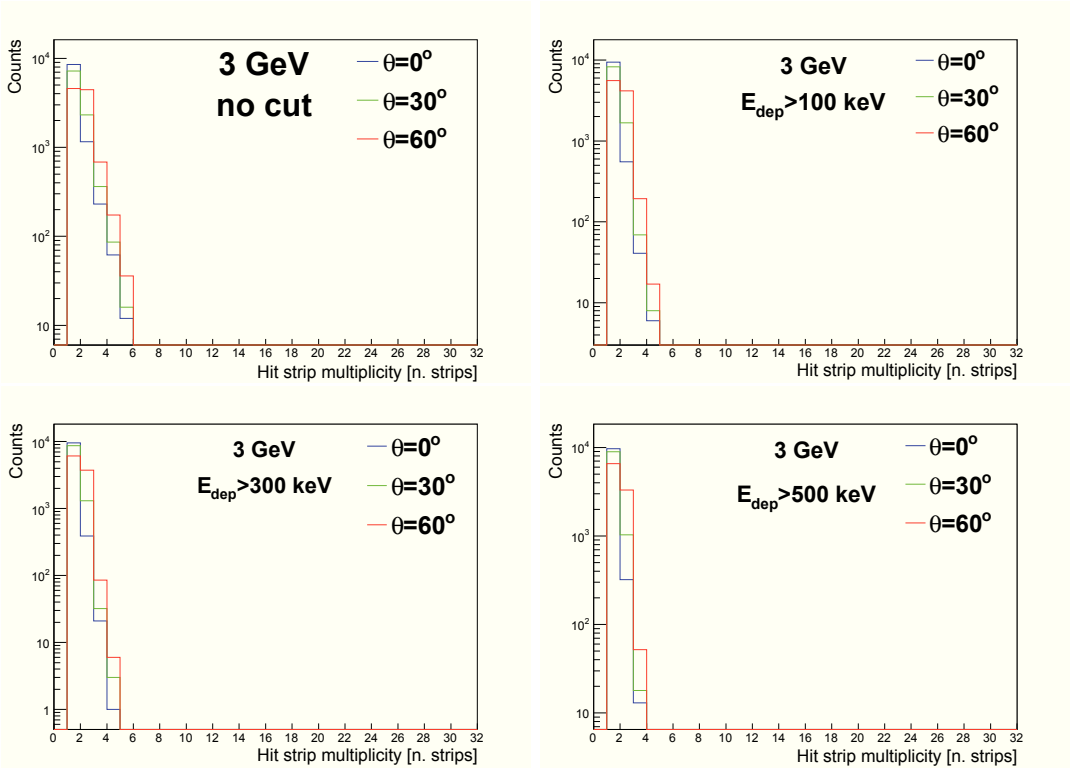

Figure 8.13: Multiplicity of hit strips for different energy thresholds and zenith angle for primary muons of 3 GeV.

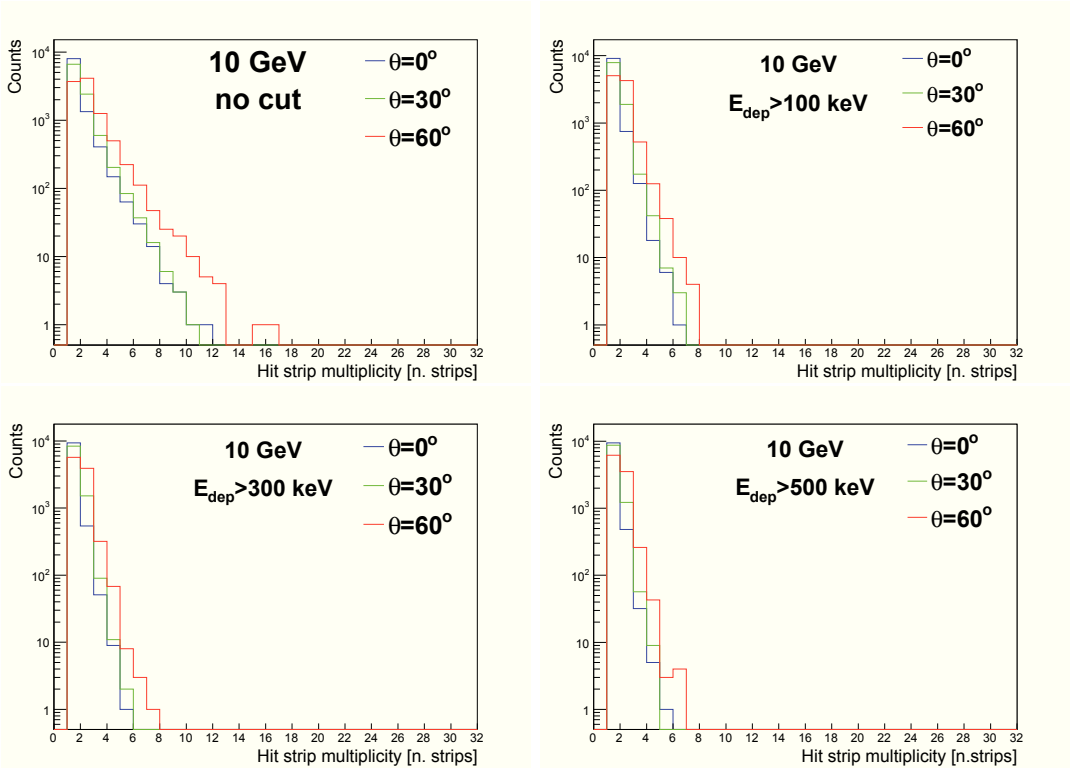

Figure 8.14: Multiplicity of hit strips for different energy thresholds and zenith angle for primary muons of 10 GeV.

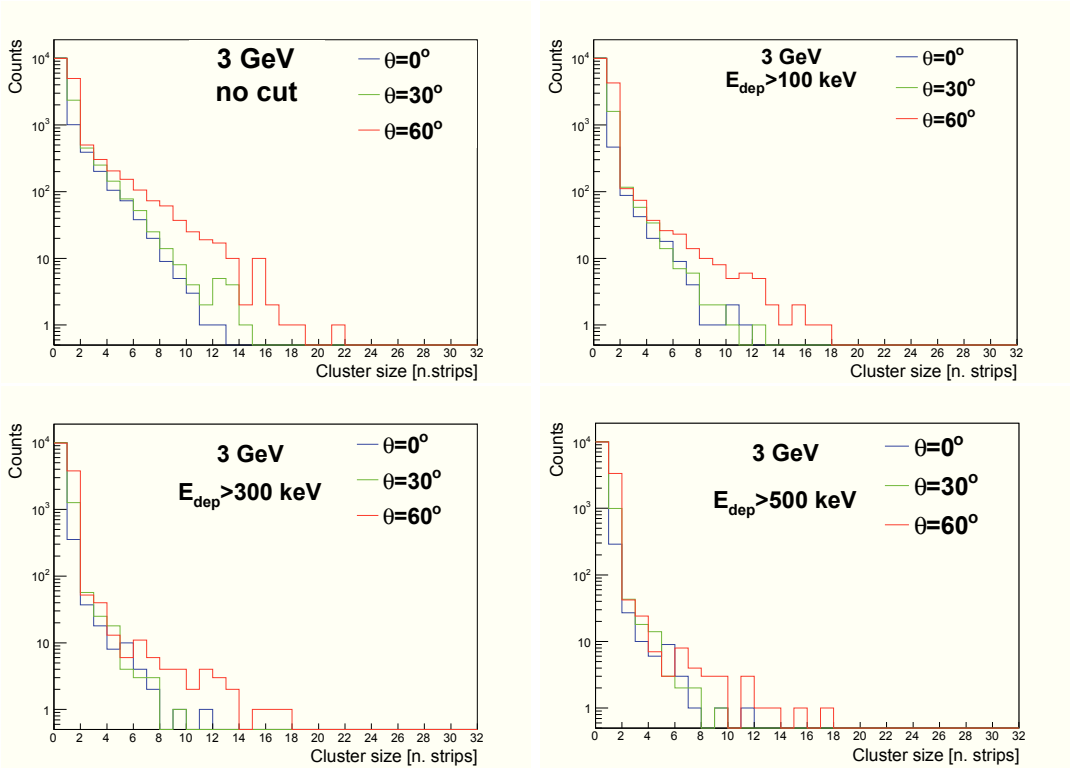

Figure 8.15: Cluster size for different energy thresholds and zenith angle for primary muons of 3 GeV.

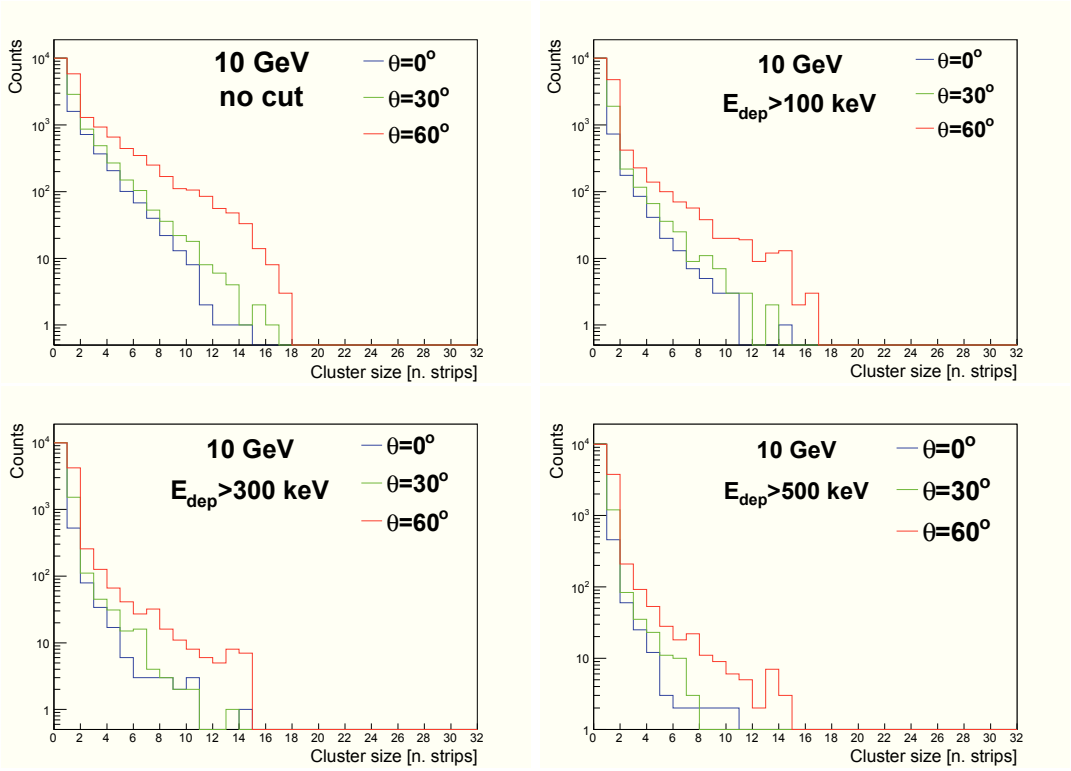

Figure 8.16: Cluster size for different energy thresholds and zenith angle for primary muons of 10 GeV.

The simulation of single muons has been used, this time considering the deposited energy E_{dep}, and the distance d from the PMT at which the particle crossed the detector. Following the method described in Section 6.3, the E_{dep} has been converted into a number of photoelectrons and, once the distance and the number of photoelectrons are given, a trace corresponding to the input has been extracted from the muon library.
Using this simple simulation, the detection efficiency for different counting strategies and discrimination thresholds can be estimated. Each trace is discriminated at a threshold corresponding to a fraction of the mean amplitude of a single photoelectron (*spe*). In this work, different thresholds were used: 20%, 30% and 40%. The strategy chosen to count the number of muons in the detector is based on a pattern recognition. A muon is counted if and only if n "1s" are found in a given position within a given time window w. We indicate as **11** the requirement of at least two consecutive 1s; **1x1** indicates a muon if *two ones* with one sample (0 or 1) among them are found in the time window. The optimum w parameter depends mainly on the fiber type and on the PMT model. The detector efficiency is calculated from the ratio between the detected particles and the injected particles and it is shown in Figures 8.17 and 8.18 fot three different discrimination thresholds, as a function of the distance from the PMT. Vertical ($\theta = 0°$) and inclined ($\theta = 30°$ and $\theta = 60°$) muons of 2 - 5 - 10 - 50 - 100 GeV for a total of 50000 entries have been considered in the simulation (each energy value includes 10000 entries). Each point represents the mean of all entries with the error bar corresponding to the standard error on the mean. The results take into account only the muons that hit the detector.

The overcounting increases with the zenith angle, due to the fact that a inclined muon can hit two strips simultaneously. Another cause of the overcounting may be the cross-talk (XT) between neighboring pixels, which proves to be about 10%. In systems in which the discrimination threshold is set below the *spe* height, this effect can become important. The **1x1** counting appears to be the best suited method for counting muons, as it eliminates the overcounting due to XT regardless of the threshold. For example, in the case of the **1x1** counting, considering vertical muons and a discrimination threshold set to one third of the mean single

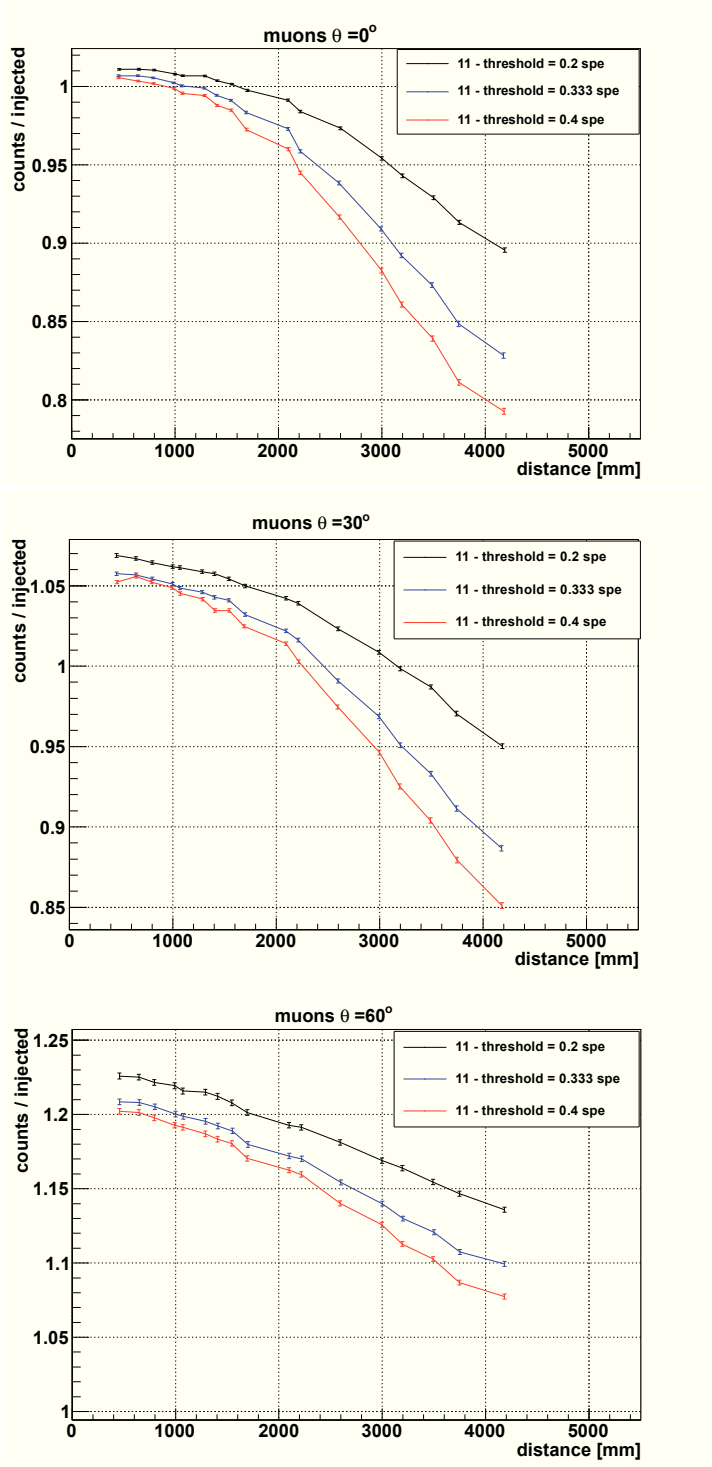

Figure 8.17: Ratio between the number of counts obtained from the module simulation and the total number of injected muons as function of the distance from the PMT. Vertical and inclined muons of 2 - 5 -10 - 50 - 100 GeV have been considered in the simulation. Counting strategy **11** has been used. The error bar corresponds to the error on the mean.

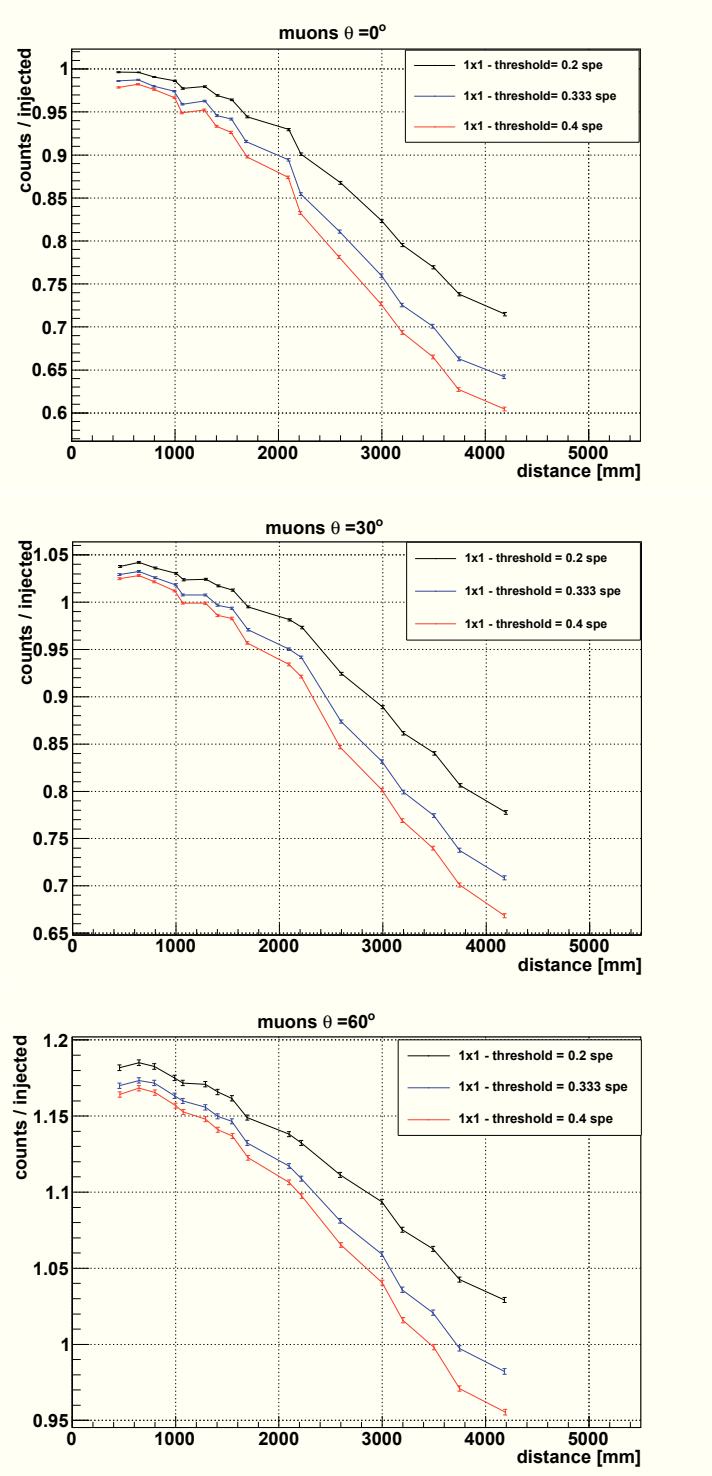

Figure 8.18: Ratio between the number of counts obtained from the module simulation and the total number of injected muons as function of the distance from the PMT. Vertical and inclined muons of 2 - 5 -10 - 50 - 100 GeV have been considered in the simulation. Counting strategy **1x1** has been used. The error bar corresponds to the error on the mean.

photoelectron amplitude (30% spe), an overall ratio of 86% was found. The Table 8.2 shows the overall ratios as a function of the angle theta, of the counting strategy, and of the discrimination threshold. Note that the detector efficiency depends on the applied counting strategy and discrimination threshold.

Subsequently, the effect of the secondary particles generated by muons, also has been considered. Figures 8.19, 8.20, 8.21, 8.22, 8.23, 8.24 show the effect of muons more that of the secondary particles. Vertical ($\theta = 0°$) and inclined ($\theta = 30°$ and $\theta = 60°$) muons of 2 - 5 - 10 GeV, with three different discrimination thresholds, have been considered in the simulation. As you can see, the ratio increases with the increase of energy and azimuthal angle. The **1x1** technique shows the best counting ratio. The overcounting for inclined muons can be explained by the fact that a muon can pass through two strips simultaneously. Figures 8.25 and 8.26 summarize the results obtained, i.e. the effect observed considering only muons, as well as that one considering also the secondary particles. This analisys has been obtained considering muons with $\theta = 0°$, $\theta = 30°$ and $\theta = 60°$, two counting strategies and a fixed discrimination threshold (30%). When we consider only muons, the latter have been regarded with all energy values (2 - 5 - 10 - 50 - 100 GeV), while when adding also the effect of the secondary particles, we consider individually muons of 2, 5 and 10 GeV.

A detailed study of the overcounting due to secondary particles accompanying the muon during its propagation has been performed, considering muons of 5 GeV with $\theta = 0°$, $\theta = 30°$ and $\theta = 60°$, two counting strategies (**1x1** and **11**), and a fixed discrimination threshold (30 % spe amplitude) (see Figure 8.27).

From the performed simulation, the overcounting due to the secondary particles proves to be of about 5%, 6% and 8% respectively for muons with $\theta = 0°$, $\theta = 30°$, and $\theta = 60°$.

It is also possible make some considerations regarding the propagation of the signal along the fiber. This analisys has been performed considering just vertical muons ($\theta = 0°$), two counting strategies and a fixed discrimination threshold (30% spe amplitude) (see Figure 8.28). The graphics show the ratio between the number of counts obtained and the total number of injected muons, as function of the photoelectrons number. The signal at the start and end of the fiber has been considered. As can you see, the difference between the two curves means

Theta angle	Counting	Threshold	Overall ratio
$\theta = 0°$	1x1	0.2 spe	90%
$\theta = 0°$	1x1	0.333 spe	86%
$\theta = 0°$	1x1	0.4 spe	84%
$\theta = 0°$	11	0.2 spe	98%
$\theta = 0°$	11	0.333 spe	95%
$\theta = 0°$	11	0.4 spe	93%
$\theta = 30°$	1x1	0.2 spe	96%
$\theta = 30°$	1x1	0.333 spe	92%
$\theta = 30°$	1x1	0.4 spe	90%
$\theta = 30°$	11	0.2 spe	103%
$\theta = 30°$	11	0.333 spe	100%
$\theta = 30°$	11	0.4 spe	99%
$\theta = 60°$	1x1	0.2 spe	112%
$\theta = 60°$	1x1	0.333 spe	110%
$\theta = 60°$	1x1	0.4 spe	109%
$\theta = 60°$	11	0.2 spe	118%
$\theta = 60°$	11	0.333 spe	116%
$\theta = 60°$	11	0.4 spe	114%

Table 8.2: Overall ratios as a function of the angle theta, of the counting strategy and of the discrimination threshold. The results take into account only primary muons.

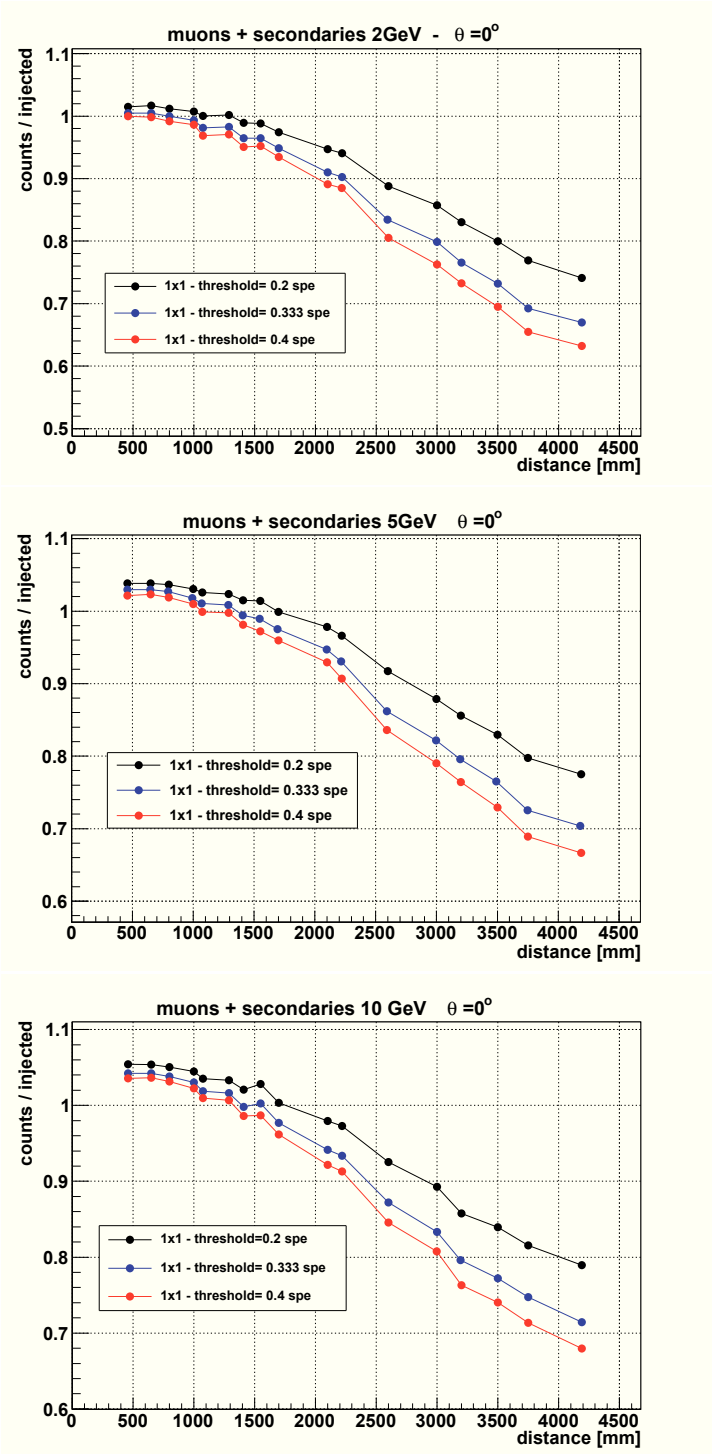

Figure 8.19: Ratio between the number of counts obtained and the total number of injected muons as function of the distance from the PMT. The effect of the secondary particles also has been considered. The plots are obtained by considering the counting strategy **1x1**, vertical muons ($\theta = 0°$) and three values of energy, 2 - 5 - 10 GeV.

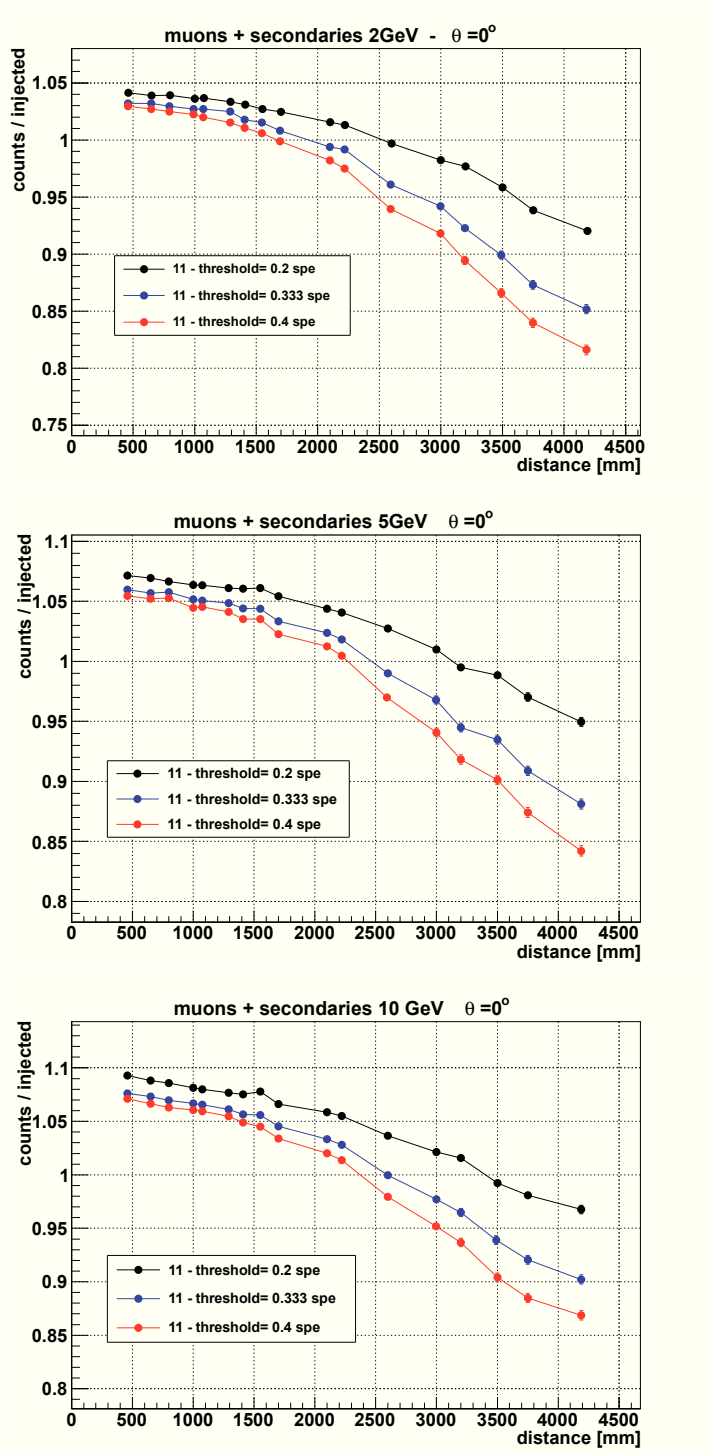

Figure 8.20: Ratio between the number of counts obtained and the total number of injected muons as function of the distance from the PMT. The effect of the secondary particles also has been considered. The plots are obtained by considering the counting strategy **11**, vertical muons ($\theta = 0°$) and three values of energy, 2 - 5 - 10 GeV.

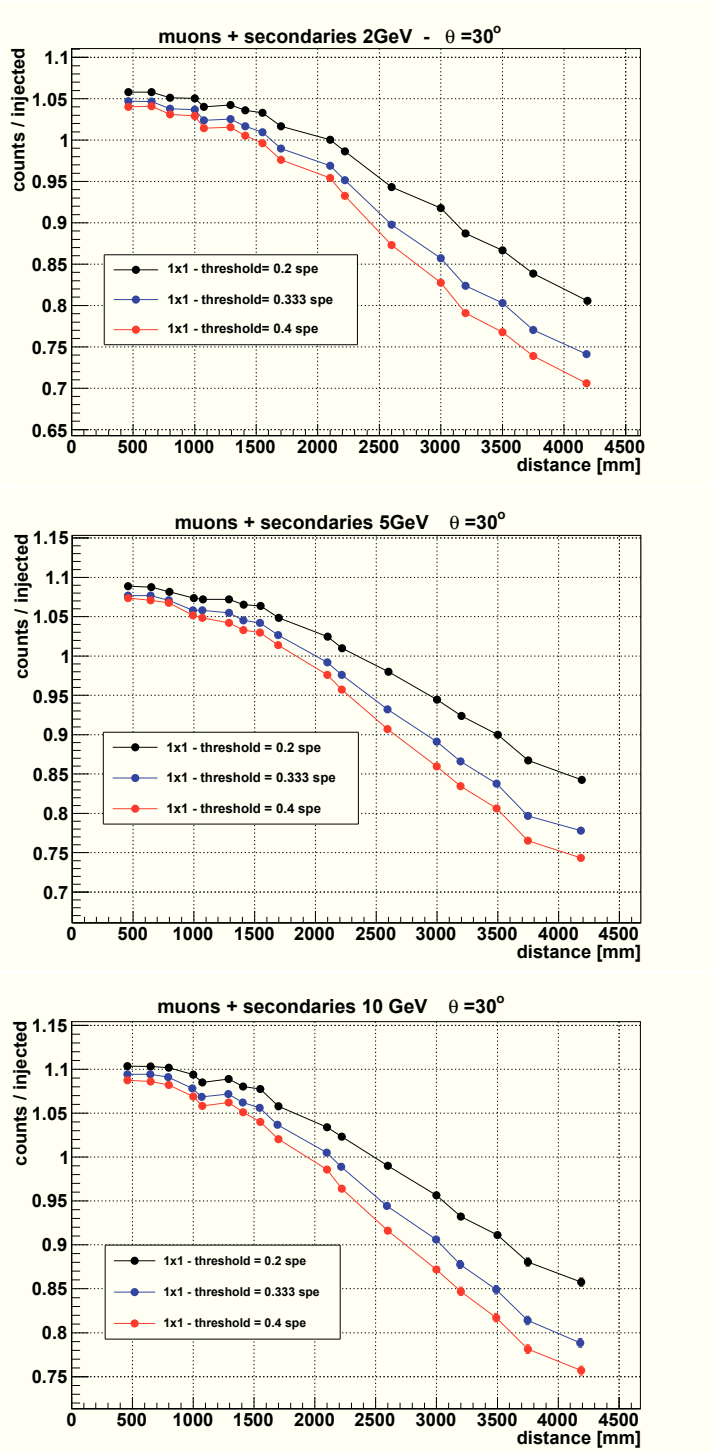

Figure 8.21: Ratio between the number of counts obtained and the total number of injected muons as function of the distance from the PMT. The effect of the secondary particles also has been considered. The plots are obtained by considering the counting strategy **1x1**, inclined muons ($\theta = 30°$) and three values of energy, 2 - 5 - 10 GeV.

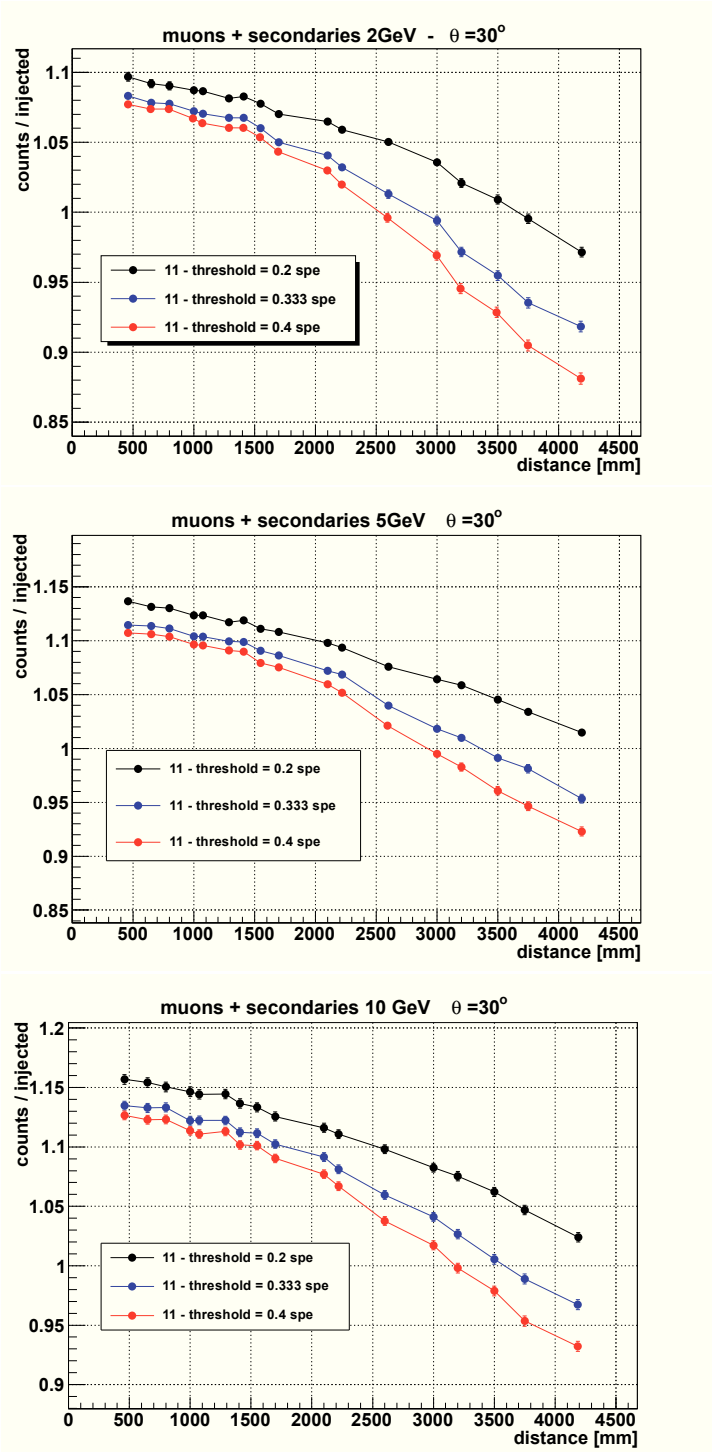

Figure 8.22: Ratio between the number of counts obtained and the total number of injected muons as function of the distance from the PMT. The effect of the secondary particles also has been considered. The plots are obtained by considering the counting strategy **11**, inclined muons ($\theta = 30°$) and three values of energy, 2 - 5 - 10 GeV.

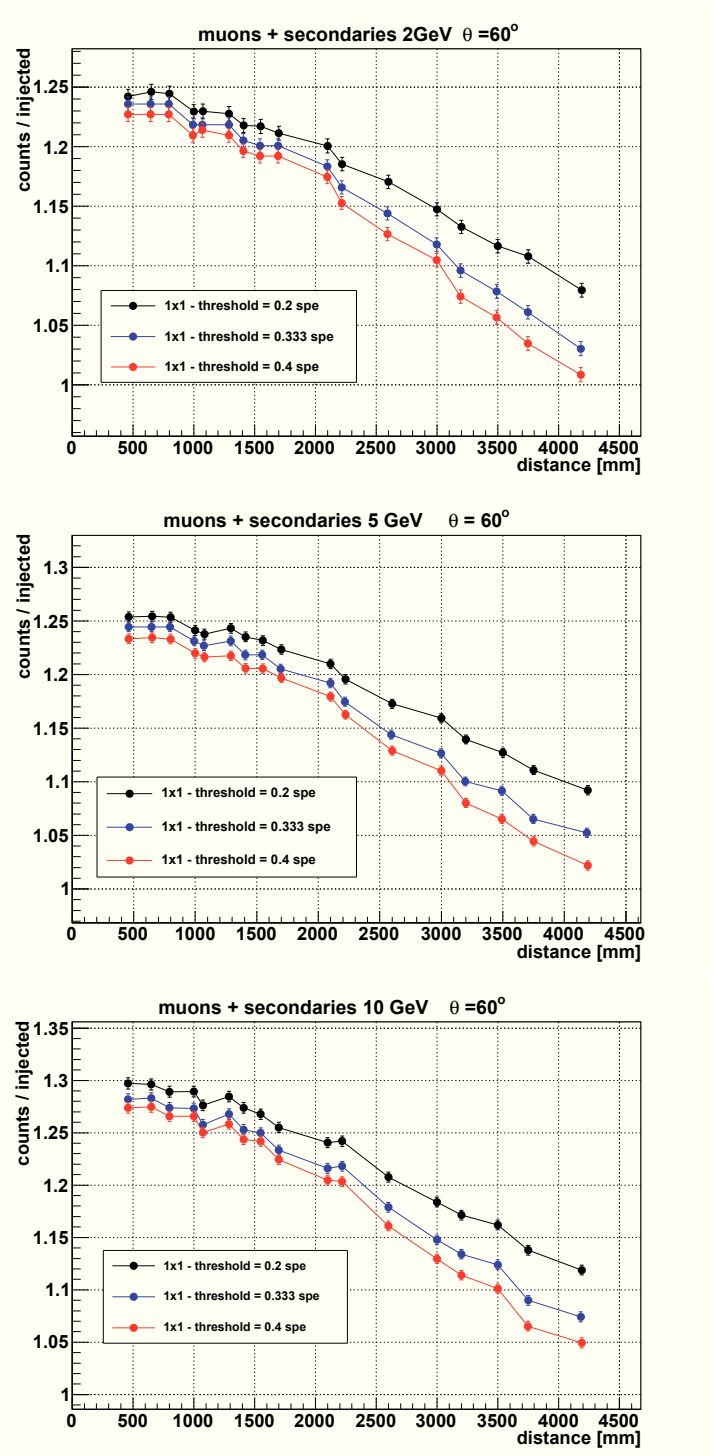

Figure 8.23: Ratio between the number of counts obtained and the total number of injected muons as function of the distance from the PMT. The effect of the secondary particles also has been considered. The plots are obtained by considering the counting strategy **1x1**, inclined muons ($\theta = 60°$) and three values of energy, 2 - 5 - 10 GeV.

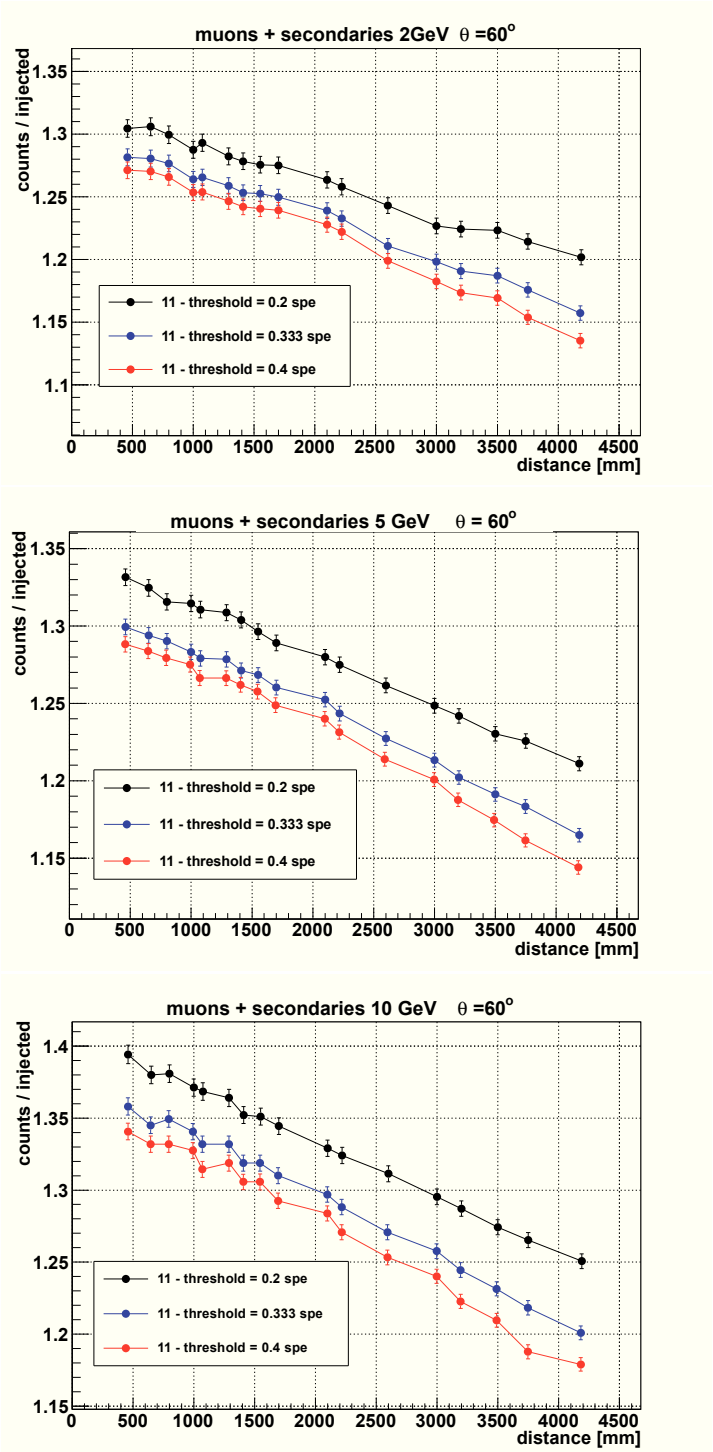

Figure 8.24: Ratio between the number of counts obtained and the total number of injected muons as function of the distance from the PMT. The effect of the secondary particles also has been considered. The plots are obtained by considering the counting strategy **11**, inclined muons ($\theta = 60°$) and three values of energy, 2 - 5 - 10 GeV.

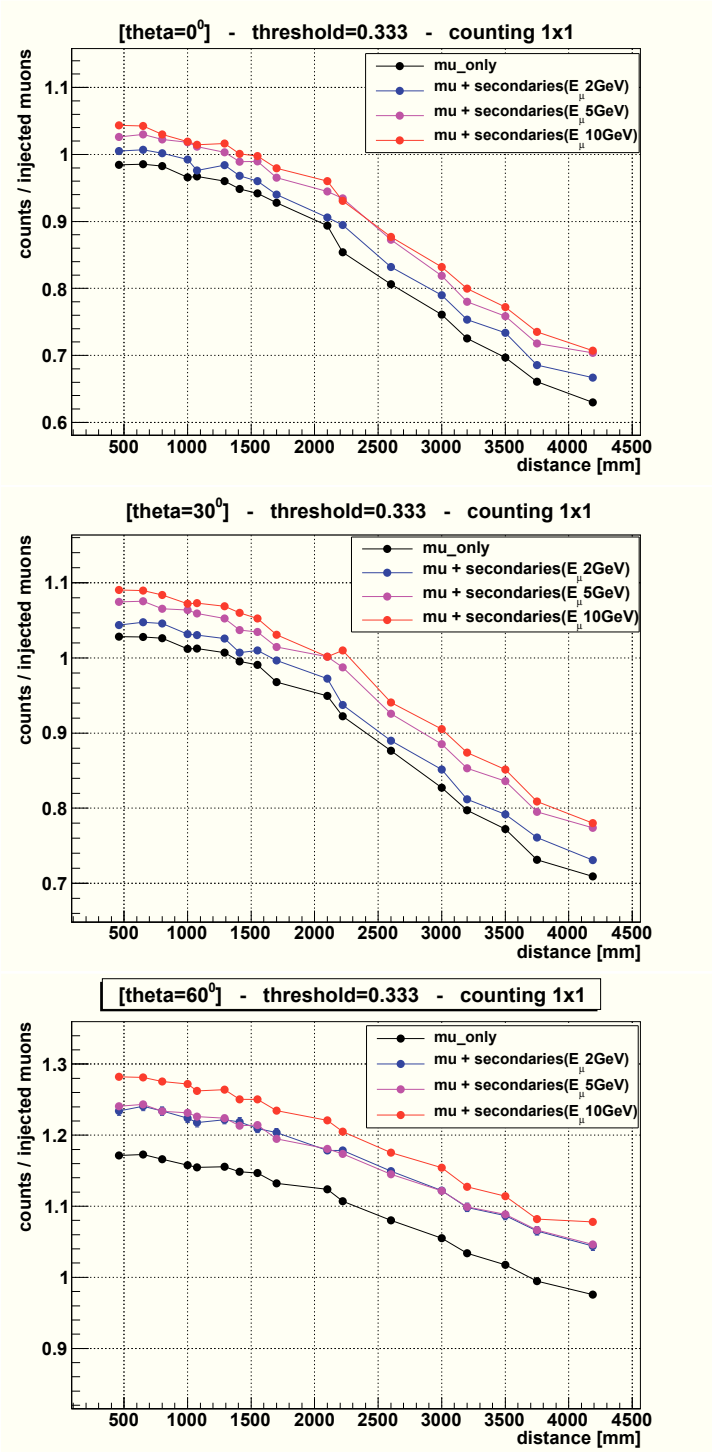

Figure 8.25: Ratio between the number of counts obtained and the total number of injected muons as function of the distance from the PMT. The effect of the secondary particles also has been considered. The plots are obtained by considering the counting strategy **1x1**, vertical and inclined muons of different energies, and a discrimination threshold set to one third of the mean single photoelectron amplitude (0.333 spe).

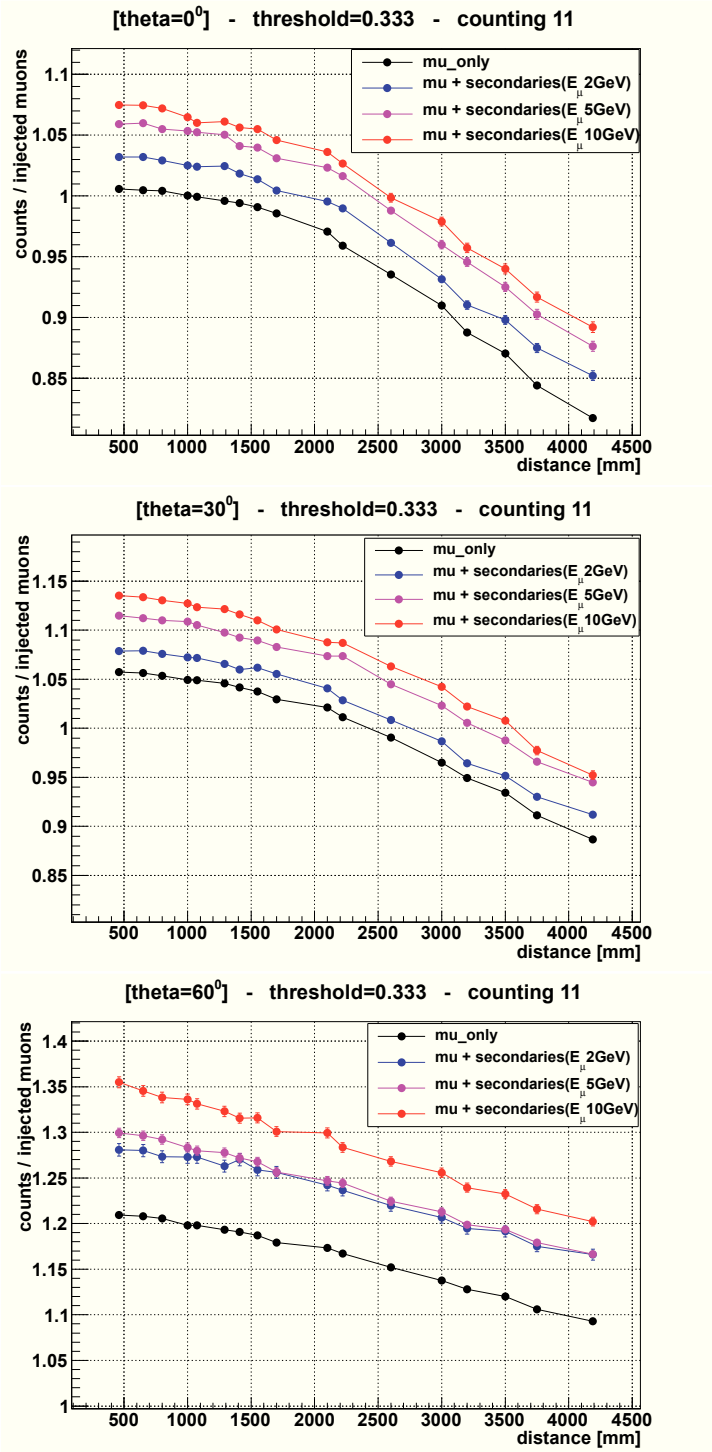

Figure 8.26: Ratio between the number of counts obtained and the total number of injected muons as function of the distance from the PMT. The effect of the secondary particles also has been considered. The plots are obtained by considering the counting strategy **11**, vertical and inclined muons of different energies, and a discrimination threshold set to one third of the mean single photoelectron amplitude (0.333 spe).

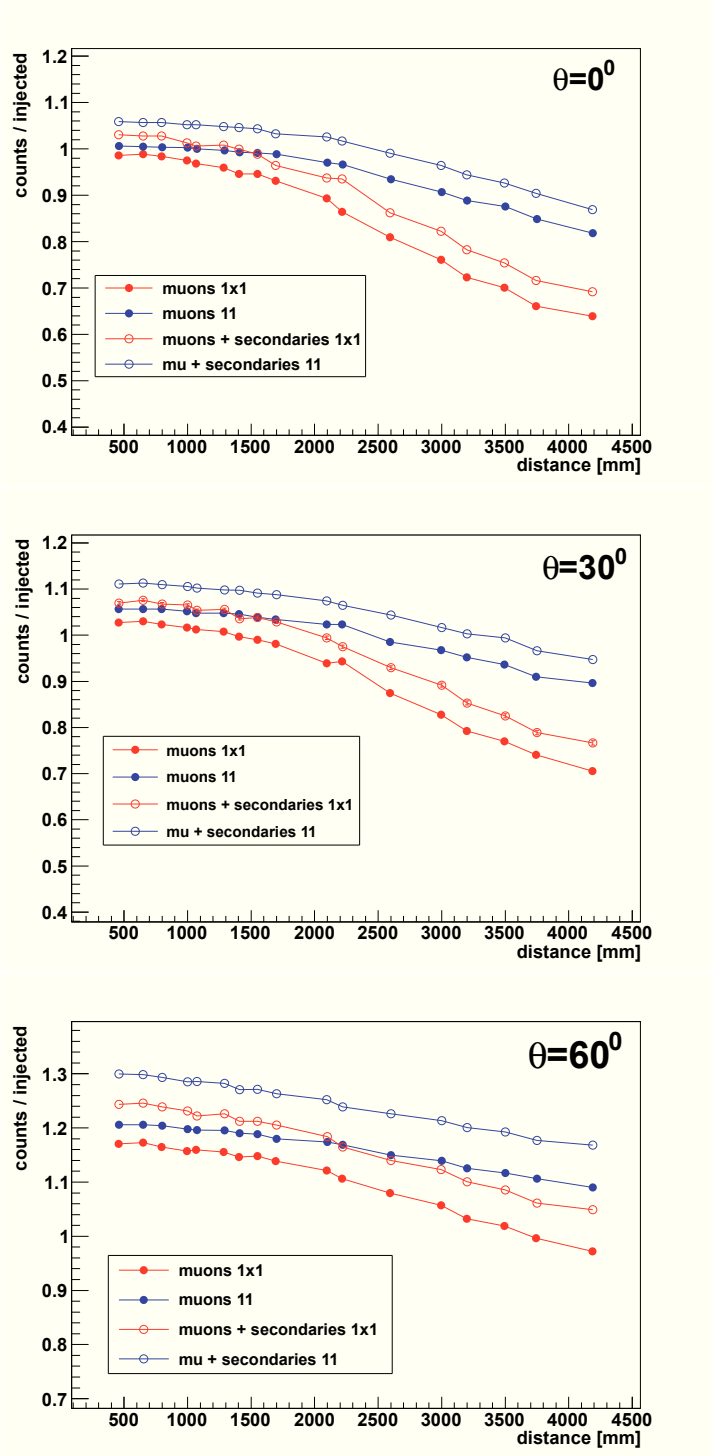

Figure 8.27: Ratio between the number of counts obtained from the module simulation and the total number of injected muons as function of the distance from the particle position to the PMT. Vertical ($\theta = 0°$) and inclined ($\theta = 30°$ and $\theta = 60°$) muons of 5 GeV have been considered in the simulation. The overcounting was studied for two counting strategies (**1x1** and **11**) and a fixed discrimination threshold (30% spe amplitude), and it proves to be of about 5%, 6% and 8% respectively, for muons with $\theta = 0°$, $\theta = 30°$, and $\theta = 60°$.

that near and far signals from the PMT have some shape difference probably due to the propagation of the signal along the fiber. In addition, you can also see that the full detection efficiency occurs from around 11 npe onwards for the **11** strategy, while it occurs around 15 npe for the **1x1** strategy.

8.2 Simulations with showers

The aim of this section is to analyse the muon counter efficiency. For this analysis, 600 proton showers with an energy of $E = 3.16 \times 10^{18}$ eV, zenith angle $< 60°$ and uniform distribution in azimuth, were generated with CORSIKA. These simulations have been performed using the *Module Sequence* described in Section 7.1.3. These events are read by means of the *EventFileReaderOG* module. The shower particles arriving to the Earth surface were then propagated through the soil using the *GroundPropagatorTO* module. Once the particles hit the strips, by means of the *MdEdepSimTO* module, the deposited energy is converted into a number of single photoelectrons and then a signal shape corresponding to the input is extracted from the muon trace library. This signal is then analyzed by counting algorithms, in order to get the muon counter efficiency. To avoid the possibility that the signal be counted twice in the same strip, a time veto window *timew* around 30 ns has been applied. This value should be enough to avoid over-counting. In order to propagate the particles that can produce a signal, the CORSIKA energy cutoff for the muons, electrons and photons was set to 100 MeV, while for all the remaining particles a cutoff of 1TeV was applied. No energy deposit threshold was considered. The distribution of the core-positions of these showers is shown in figure 8.29. Each WCD is coupled with three 10 m^2 buried modules.

8.2.1 Punch-through

Using the parametrization of the fraction of particles reaching the detection depth, the punch-through has been evaluated. The energy distributions for each of these particles have been obtained by means of simulated showers by CORSIKA. One hundred showers induced by $10^{18.5}$ eV protons, with $\theta = 0°$, have been

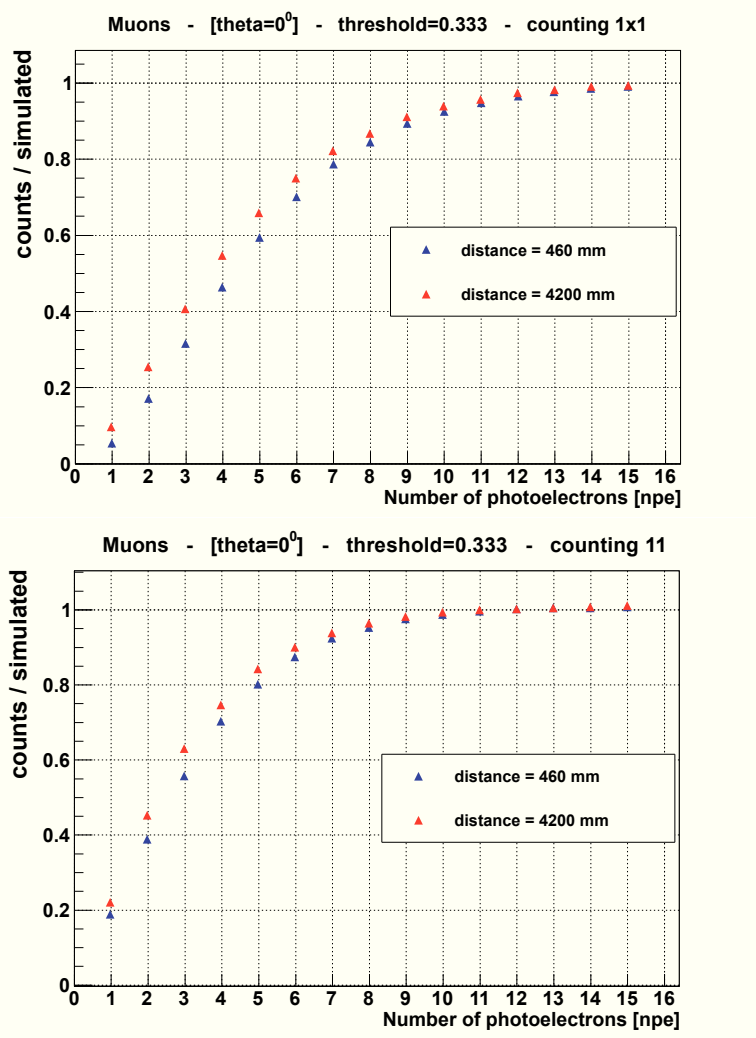

Figure 8.28: Ratio between the number of counts obtained and the total number of injected muons, as function of the photoelectrons number. This analisys shows the effect of the signal propagation along the fiber. The signal at the start and end of the fiber has been considered (the distances labeled on the legend refer compared to PMT). **(a):** Counting strategy **1x1**; **(b):** Counting strategy **11**.

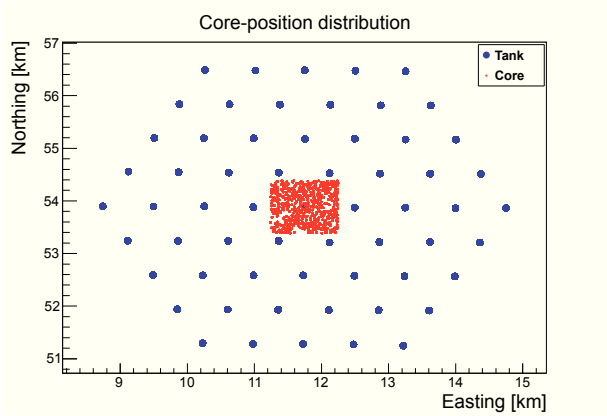

Figure 8.29: Distribution of core-positions of 600 events simulated by CORSIKA, on the AMIGA 750 m array. The area is around to the WCD labelled as "734" (a.k.a. Constanza).

used. Then, these distributions have been weigthed according to the parametrized probabilities obtained previously, in order to get the distributions at detection depth (see Figure 8.30). γ and e^- are the most abundant particles while μ^- have, by far, the highest energies. The distributions of the electromagnetic component peak is below 100 MeV while the muon maximum is close to 4 GeV. It can be seen that most of the electrons and photons are absorbed in the soil above the AMIGA detector, while at the detection depth, the energy spectrum moves towards higher values.

The ratio between the electromagnetic and the muonic component at detector depth has been evaluated considering showers induced by 10^{18} and $10^{18.5}$ eV protons, which allows us to evaluate the punch-through. The punch-through depends on both the distance from shower core and zenith angle. Among the analyzes carried out, we show the case of vertical showers (see Figure 8.31), where the punch-through appears to be about 1 -2% at 200 m from the shower core, at a depth of about 2.5 m underground. For cases with inclined showers, the contamination will always be lower. These results confirm the choice of the depth of 2.3 m, which is a good compromise to avoid the contamination of the electromagnetic component, mantaining the punch-through always below 5%.

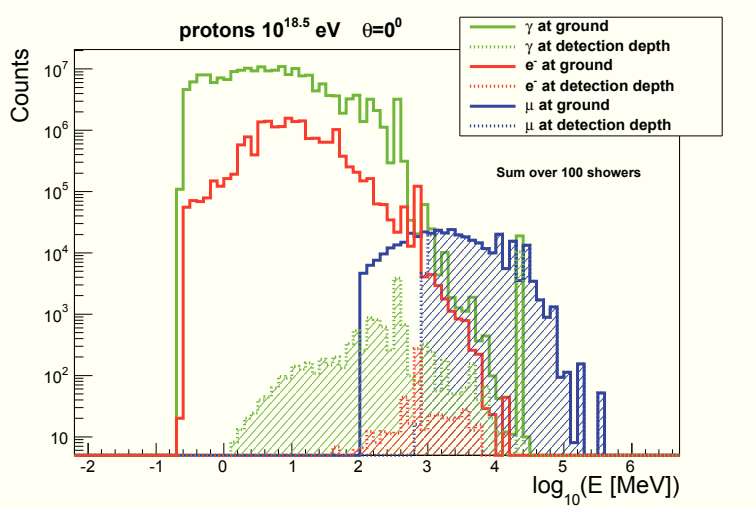

Figure 8.30: Energy distributions of particles. 100 air showers induced by $10^{18.5}$ eV protons with $\theta = 0°$ were used. The electromagnetic component peak is below 100 MeV while the muon maximum is close to 4 GeV.

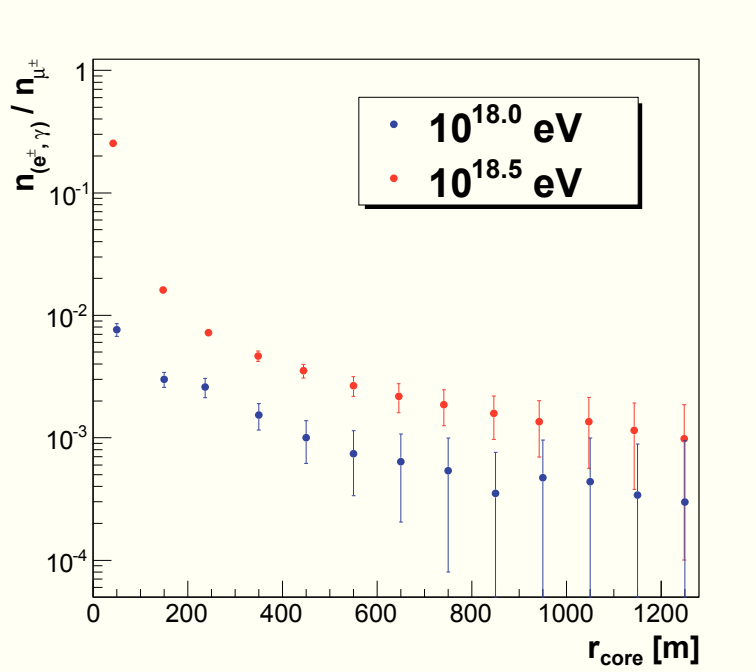

Figure 8.31: Ratio between the electromagnetic and the muonic component at detector depth. Showers induced by 10^{18} and $10^{18.5}$ eV protons have been simulated. Only the statistical errors are indicated.

8.2.2 Muon pile-up results

As explained in Chapter 4, muons hitting the same strip in a predefined time window are counted only once, an effect resulting in an undercounting. When the number of incident muons $N_(\mu)$ increases, the difference with muons counted N_μ^C increases, since there is more and more pile-up The AMIGA detectors are built of 3 or 4 modules of 64 channels each, and the total counts in a full muon counter are just the sum of the counts in the sub-modules. We therefore mapped the pile-up functions only for the basic module with 64 segments. For this analysis two counting strategies (**1x1** and **11**), and three discrimination threshold (20%, 30% and 40% spe amplitude), have been considered. In this way, we study the effect of muon counter segmentation. The undercounting due to muon pile-up can be corrected for by applying Eq.4.3. In Figure 8.32, the relation between N_μ^C and N_μ is shown by the blue points for 64 segments; the corrected muon number is superimposed in red. As you can see, we get a good result of the pile-up correction for the **11** counting strategy, while an undercounting is observed for the **1x1** strategy.

The relative efficiency

$$Eff^{rel} = \frac{N_\mu^C - N_\mu}{N_\mu} \tag{8.10}$$

is plotted in Figure 8.33 as a function of the injected number of muons.

For each point, the displayed error is the RMS error, while the horizontal bar represents the width of the considered bin. The **11** strategy, imposing a discrimination threshold of 40% appears to be the best configuration, since the relative difference, after the correction, appears to be close to zero. In Figure 8.34 the counting ratio of the two used strategies is evaluated at different discrimination thresholds for all simulated showers. Each point represents the average efficiency calculated on all the counters for each simulated event. The **11** strategy proves to be the best suited method for counting muons. For this strategy, a counting ratio around 98% was found for a discrimination threshold of 0.3 times the amplitude of the single photoelectron.

The results obtained so far, have not taken into account some aspects. In fact,

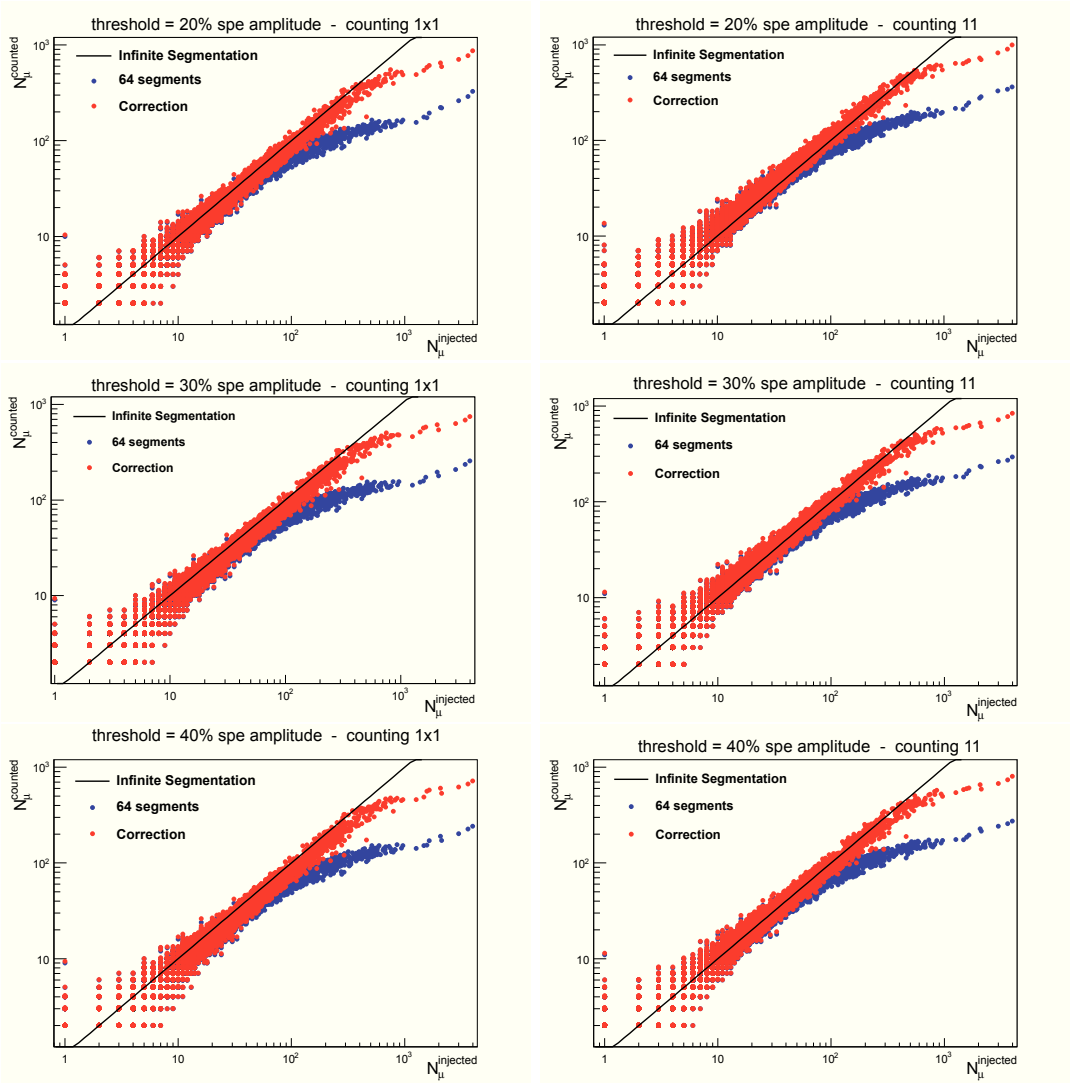

Figure 8.32: Number of counted muons as a function of the incident ones for 64 segments. In the ideal case of infinite segmentation $N_\mu^C = N_\mu$. The pile-up correction is superimposed on the plots. Two counting strategies and three discrimination thresholds have been considered.

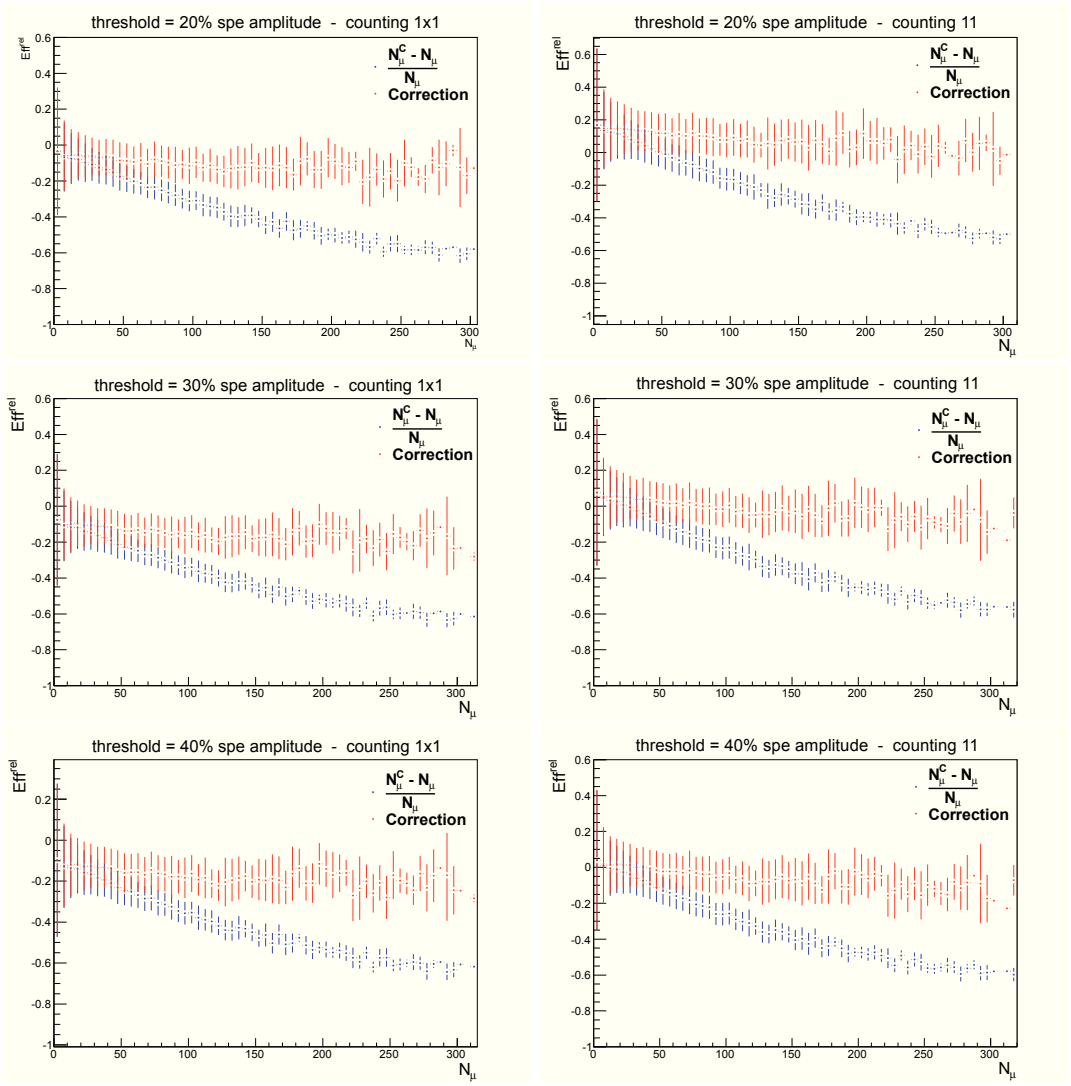

Figure 8.33: Relative efficiency as a function of the injected number of muons. For each point, the displayed error is the RMS error, while the horizontal bar represents the width of the considered bin. Two counting strategies and three discrimination thresholds have been considered.

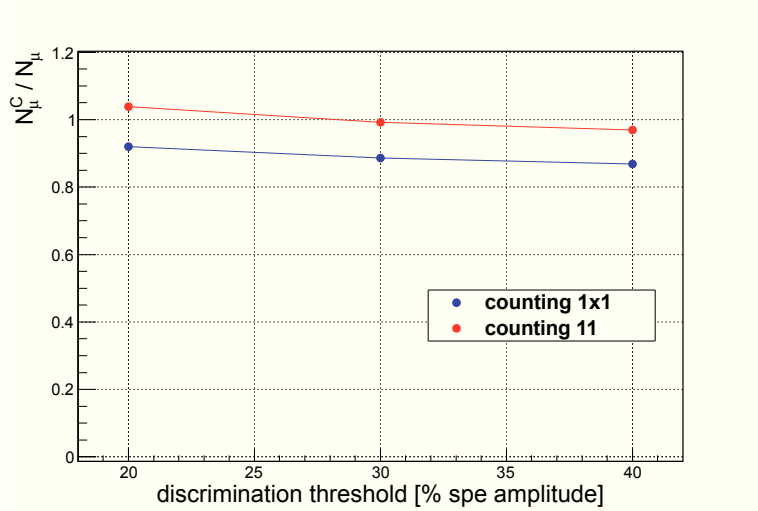

Figure 8.34: The ratio between the obtained number of counts and the total number of injected muons is expressed as function of the discrimination thresholds. For a discrimination threshold set to one third of the mean single photoelectron amplitude, an efficiency of ∼88% can be obtained for the **1x1** strategy and ∼98% for the **11** strategy.

before to support a specific counting strategy, we should include in the simulation some effects, as the detector electronics and the cross-talk. The latter is very important, and it allows us to exclude signals due to of single photoelectrons. Apparently, it would seem that the better efficiency is obtained by adopting the 11 counting strategy. This strategy, considering only two bin, could include single photoelectrons, and therefore would not be very reliable, while the 1x1 strategy would tend to exclude the presence of single photoelectrons.

Chapter 9

Conclusions

The main aim of this work has been to analyze, through laboratory measurements and simulation studies, the performances of the muon detectors of the AMIGA project.
Six muon scintillator modules (two 10 m^2 and four 5 m^2 units) have been built in the mechanical workshop of INFN-Torino. During the construction phase, the response of each module has been tested using both atmospheric muons and a radioactive source, and the results have been reported. In particular the average number of photoelectrons in the PMT for a vertical muon crossing the detector has been measured to be between 5 and 15 according to the position at which the particle crosses the detector with respect to the distance to the photomultiplier. The fiber attenuation curves for all the six modules was derived with this procedure. It is clear from the results that the choice of the smaller modules for the production phase would guarantee to have a higher signal to noise ratio, with a minimum of 7-8 photoelectrons/particle.
Another important step of this work has been to create a library of muon traces, recording the time traces of the muons measured as a function of the number of photoelectrons produced in the scintillator by the particles and of the distance to the photomultiplier.
The muon time traces, together with the above described measures of the attenuation of the signals along the fibers were used to write a complete simulation of the scintillator modules, which was included in a Monte Carlo describing the propagation of either single particles or air showers in air, through the soil, down

to the underground counters.
Using the simulation, the fraction of electromagnetic contamination in the signal detected underground was evaluated. The punch-through proves to be ∼1% at 200 m from shower core for vertical $10^{18.5}$ eV proton shower, at a depth of ∼2.5 m underground. We can thus confirm that the chosen depth for burying the counters is more than enough to guarantee a clean direct measure of the muon component of the air showers.
The detector efficiency (defined as the ratio between the detected and the injected number of particles) was studied for different counting strategies and discrimination thresholds. We studied two strategies to define a muon in the digitized output of the detectors: a **1x1**, where 3 consecutive digits are needed, and a **11**, where only two consecutive "on-signals" are enough. All counts have been corrected for the pile-up due to muons hitting the same strip in the same time, taking into account the basic 64 segmentation of each single module. For this analysis three discrimination threshold (20%, 30% and 40% spe amplitude), have been considered.
Efficiencies of ∼ 85% and 95% were obtained for the **1x1** and for the **11** strategy respectively, considering only vertical primary muons. The efficiency becomes of ∼86% for the **1x1** strategy and ∼98% for the **11** strategy, considering full showers with the zenith angle between 0° and 60°. The overcounting due to the secondary particles proves to be of about 5%, 6% and 8% respectively for muons with $\theta = 0°$, 30°, and 60°. The **11** strategy, with a discrimination threshold of 40%, appears to be the best configuration. However, any conclusion about the best strategy to choose must be considered preliminar, since other important factors, such as the detector electronics and the cross-talk, are still missing in the simulation. Single photoelectron signals, e.g., are recorded in a single digit; as a consequence, they could mimic muons in the **11** strategy, thus causing a serious overcounting problem, while the **1x1** would be more reliable.
The six modules built in Turin have been installed in the Unitary Cell of the AMIGA muon enhancement, which is going to be completed by the end of 2014, while the second twin counter will be ready to record data in the first months of next year. We will be able then to measure the accuracy in the muon counting,

by testing the Poissonian behavior of the muon modules after the pile-up correction has been applied, and to evaluate the presence of possible further systematic effects. The data analysis will allow us to study the detector efficiency and apply the different strategies studied in this thesis to obtain a reliable measure of the muon component of extensive air showers.

An event-by-event determination of the muons in the showers will allow to get invaluable information about the primary composition and, furthermore, to check the indirect measurements of muons that Auger can provide by means of the Surface Detector stations.

Bibliography

Abraham J. (2008). *Astroparticle Physics*, **29**, 243. 30, 33

Abraham J., *et al.* (2004). *Nucl. Instrum. Meth.*, **A523**, 50. 3

Abraham J., *et al.* (2009). *arXiv:0907.4282*. 48

Abraham J., *et al.* (2010). *Nucl. Instrum. Meth.*, **A 613**, 29. 71

Abu-Zayyad, *et al.* (2001). *Astrophys. J*, **557**, 686. 5

Adamson P. for the MINOS Collaboration (1998). *NuMI*, **L-33**. 67

Aglietta M. for the PAO Collaboration (2005). *Proceedings of 29th International Cosmic Ray Conference, Pune, India*, **7**, 279. 41

Agostinelli S., *et al.* (2003). *Nucl. Instrum. Meth.*, **A 506**, 250. 105

Allard D., *et al.* (2005). *Astron. Astrophys.*, **443, L29**. 12

Allison J., *et al.* (2006). *IEEE Trans. Nucl. Sci*, **53**, 270. 105

Almela A., *et al.* (2013). *33RD International Cosmic Ray Conference, Rio de Janeiro, Brazil*, 1209. 70

Alvarez-Muniz J., *et al.* (2002). *Phys. Rev.*, **D 66**, 033011. 21

Anderson C. D. (1961). *Am. J. Phys.*, **29**, 825. 1

Antoni T. (2001). *Astropart. Phys.*, **14**, 245. 37

Apel W. D., *et al.* (2004). *Astropart. Phys.*, **24**, 467. 37

Arciprete F., *et al.* (2006). *Nuclear Physics B*, **150**, 186. 48

Argiro' S., *et al.* (2007). *Nucl. Instrum. Meth.*, **A 580**, 1485. 108

Auger P., *et al.* (1939). *Rev. Mod. Phys.*, **11**, 288. 2

Ave M., *et al.* (2007a). *Astropart. Phys.*, **28**, 41. 47

Ave M., *et al.* (2007b). *Nucl. Instrum. Meth.*, **A 578**, 180. 61

Ave M. for the Airfly Collaboration (2007). *Astroparticle Physics*, **28**, 41. 29

Babson J., *et al.* (1990). *Phys. Rev.*, **D42**, 3613. 27

Baltrusaitis R.M., *et al.* (1985). *Nucl. Inst. Methods*, **A 240**, 410. 3

Bassi P., G. Clark, and B. Rossi (1953). *Phys. Rev.*, **92**, 441. 3

Battistoni G., *et al.* (2007). *AIP Conference Proceeding 896*, 31. 107

Bell C. (1974). *J. Phys. A*, **12**, 990. 3

Belolaptikov I.A., *et al.* (1997). *Astropart. Phys.*, **7**, 263. 27

Berezhko E.G. and Ksenofontov L.T. (1999). *JETP 3*, **89**, 391. 7

Berezinsky V. and Grigoreva S.I. (1987). *Bull. Russ. Acad. Sci. Phys.*, **51N10**, 111. 11

Bertou X., *et al.* (2006). *Nucl. Instrum. Meth.*, **A568**, 839. 41

Bethe H. and Heitler W. (1934). *Proc. R. Soc. Lon. A Math. Phys. Sci.*, **146**, 83. 18

Bezrukov L.B., Bugaev E.V. (1981). *Sov. J. Nucl. Phys.*, **33**, 635. 24

Bhabha H. and Heitler W. (1937). *Proc. R. Soc. Lon. A Math. Phys. Sci.*, **159**, 432. 18

Billoir P. (2008). *Astrop. Phys.*, **30**, 270. 108

Billoir P. and Gouteraux B. (2006). *Internal GAP-Note-058*. 33

Bird D. J., *et al.* (1993). *Phys. Rev. Lett.*, **71**, 3401. 3

Blmer J.,Engel R. ,and Hrandel J. (2009). *Progr. Part. Nucl. Phys.*, **63**, 293. 22

Buchholz P. for the PAO Collaboration (2009). *Proceedings of 31th International Cosmic Ray Conference, Lodz, Poland*, **5**, 22. 72

Buren J., *et al.* (2005). *Proceedings of 29th International Cosmic Ray Conference, Pune, India*, 301. 55, 56

Candia J. (2002). *Astropart. Phys.*, **17**, 23. 8

Canet C., *et al.* (2008). *GAP-Note, 2008-159*. 80, 114

Capdevielle J.N. (1989). *J. Phys.*, **G 15**, 909. 107

Castellina A., *et al.* (2012). *GAP-Note 2012-032*. 60, 62, 65, 73

Castellina A. and Navarra G. (2007). *GAP-Note-126*. 32

Chiba N., *et al.* (1992). *Nucl. Instrum. Meth. A*, **311**, 338. 3

Chou A. (2005). *Proceedings of 26th International Cosmic Ray Conference, Pune, India*. 33

Chung D.J.H., Kolb E.W. and Riotto A. (1999). *Phys. Rev.*, **D60**, 063504. 16

CroninJ. W. (1994). *Phys. Rev.*, **D 50**, 1892. 10

De Donato C. (2007). *Proceedings of 30th International Cosmic Ray Conference, Mrida, Mexico*, 1249. 12

De Vega H.J.and Sanchez N.G. (2003). *Phys. Rev.*, **D67**, 125019. 16

Desiati P., *et al.* (1373). *Proceedings of 28st International Cosmic Ray Conference, Tsukuba, Japan*, 2003. 27

Design Report AMIGA (2006). 41. 55, 56, 76, 77, 78, 79

Dirac P. A. M. (1931). *Proc. Roy. Soc. Lond. A*, **133**, 60. 1

Douglas R. Bergman (2004). *Phys. Rev. Lett.*, **92**. 5

Edge D., *et al.* (1973). *J. Phys. A*, **6**, 1612. 3

Eidelman P. S, *et al.* (2004). *Physics Letters*, **B592**, 1. 116

Engel J., *et al.* (1992). *Phys. Rev.*, **D46**, 5013. 107

Erlykin A.D. and Wolfendale A.W. (2001). *J. Phys. G: Nucl. Part. Phys.*, **27**, 1005. 8

Etchegoyen A. (2007). *Proceedings of 30th International Cosmic Ray Conference, Merida, Mexico*, **5**, 1191. 52

Facal P. for the PAO Collaboration (2011). *Proceedings of 32nd International Cosmic Ray Conference, Beijing, China*. 31

Fesefeldt H. (1985). Pitha. *RWTH Aachen*. 107

Fletcher R.S., *et al.* (1994). *Phys. Rev.*, **D50**, 5710. 107

Frohlich Uwe (2009). *Masterarbeit*. 96

Gaisser T. and Hillas A. M. (1977). *Proceedings of 15th International Cosmic Ray Conference, Plovdiv, Bulgaria*, **8**, 353. 29

Gaisser T. K. (1990). 32

Geant4 Collaboration (2010). *http://geant4.cern.ch*, **Version 9.4**. 115

Greisen K. (1956). *Interscience Publishers, Inc.*, **3**. 36

Greisen K. (1966). *Phys. Rev. Lett.*, **16**, 748. 8, 107

Griffiths D. (1987). 2

Hara T., *et al.* (1970). *cta Phys. Acad. Sci. Hung.*, **29**, 361. 3

Harris J. Fredric (1978). *Proceedings IEEE*, **66**, 51. 96

Heck D., *et al.* (1998). *Report FZKA*, **6019**. 106, 107

Heitler W. (1938). *Proc. R. Soc. Lon. A Math. Phys. Sci.*, **166**, 529. 18

Hess V. F. (1912). *Phys. Z.*, **13**, 1084. 1

Hillas A. M. (1970). *Acta Phys. Acad. Sci. Hung.*, **29 Suppl.**, 3. 37

Hillas A.M. (1984). *Ann. Rev. Astron. Astrophys*, **22**, 425. 11

Hillas A.M. (1985). *Proceedings of 19th International Cosmic Ray Conference, La Jolla, USA*, **1**, 155. 108

Hillas A.M. (2006). *arXiv:astroph*, **0607109v2**. 13

Kalmykov N.N., Ostapchenko S.S. (1993). *Phys. At. Nucl*, **105**, 346. 107

Kamata K. and Nishimura J. (1958). *Progr Theor. Phys. Suppl.*, **6**, 93. 36, 107

Kampert K.H. (2013). *JCAP*, **1302**, 026. 31

Kawai H., *et al.* (2008). *Nuclear Physics B - Proceedings Supplements*, **175-176**, 221. 47

Kleifges M. for the PAO Collaboration (2009). *Proceedings of 31th International Cosmic Ray Conference, Lodz, Poland*. 51

Knapik R., *et al.* (2007). *arXiv:0708.1924*. 50

Knoll G. F. (2000). Radiation detection and measurement. *3rd ed.*, **J. Wiley and Sons**. 78

Kobayakawa K., *et al.* (2002). *Phys. Rev.*, **D 66**, 083004. 8

Kokoulin R.P., Petrukhin A.A. (1971). *Proceedings of 12nd International Cosmic Ray Conference, Hobart, Australia*, **6**, 2436. 24

Lagutin A.A., *et al.* (2001). *Nucl. Phys. B*, **97**. 8

Lattes C. M. G. (1947). *Nature*, **159**, 694. 2

Letessier-Selvon A. and Stanev T. (2011). *Rev. Mod. Phys.*, **83**, 907. 18

Linsley J. (1963). *Phys. Rev. Lett*, **10**, 146. 3

Lipari P. and Stanev T. (1991). *Phys. Rev.*, **D44**, 3543. 26

Maldera S. for the PAO Collaboration (2013). *33RD International Cosmic Ray Conference, Rio de Janeiro, Brazil*, **5**, 84. 86

Matthews J. (2005). *Astrop. Phys.*, **22**, 387. 18, 20, 21

Medina-Tanco (2007). *Proceedings of 30th International Cosmic Ray Conference, Mrida, Mexico*, 991. 12

Nagano M., *et al.* (1984). *J. Phys.*, **G.10**, 1295. 5

Nagano M, *et al.* (1992). *J. Phys. G*, **8**, 423. 3

Nagano M., *et al.* (2004). *Astroparticle Physics*, **22**, 235. 29

Nelson W.R., *et al.* (1985). *Report SLAC*, **265**. 107

Ogio S. and Kakimoto F. (2003). *Proc. 28th International Cosmic Ray Conference, Tsukuba, Japan*, 315. 8

Penzias A. A. and Wilson R. W. (1965). *Astrophys. J.*, 142. 9

Petrukhin A.A., Shestakov V.V. (1968). *Can. J.Phys.*, **46**, S377. 23

Pierre Auger Collaboration (2005). *Proceedings of 29th International Cosmic Ray Conference, Pune, India*, **7**, 291. 36

Plaga R. (2002). *New Astronomy*, **7**, 317. 8

Platino M. for the PAO Collaboration (2009). *Proceedings of 31st International Cosmic Ray Conference, Lodz, Poland*, **3**, 14. 54

Pradier T. for ANTARES Collaboration (2009). *Proceedings of 31st International Cosmic Ray Conference, Lodz, Poland*. 27

Pravdin M.I., *et al.* (2003). *Proceedings of 28th International Cosmic Ray Conference, Tsukuba, Japan*, 389. 5

Privitera P., *et al.* (2005). *Proceedings of 29th International Cosmic Ray Conference, Pune, India*, **00**, 101. 47

Protheroe R. J. and Szabo A. P. (1992). *Phys. Rev. Lett.*, **69**, 2885. 14

Ranft J. (1995). *Phys. Rev.*, **D51**, 64. 107

Rochester G. D. and Butler C. C. (1947). *Nature*, **160**, 855. 2

Smith B. (2008). *Internal GAP-Note 2008-161*. 34

Smith B., *et al.* (2007). *Internal GAP-Note 2007-092*. 34

Smith Steven W. (1998). 93, 94, 95

Sokolsky P. (2008). *Nuclear Physics*, **175-176**, 207. 47

Stanev T., *et al.* (1993). *Astron. and Astroph.*, **274**, 902. 8

Supanitsky A.D. (2005). *Proceedings of 29th International Cosmic Ray Conference, Pune, India*, **7**, 37. 58

Supanitsky A.D. (2008). *Astroparticle Physics*, **29**, 461. 58, 59, 73, 74, 76

Sveshnikova L.G. (2003). *Astron. and Astroph.*, **409**, 799. 8

Swordy S.P. (1995). *Proc. 24th International Cosmic Ray Conference,*, **2**, 697. 8

Takahashi Y. for JEM-EUSO Collaboration (2009). *New J. Phys.*, **11**, 065009. 47

Tkaczyk W. (2001). *Proc. 27th International Cosmic Ray Conference, Hamburg, Germany*, 5. 8

Ulrich R., *et al.* (2009). *New J. Phys.*, **11**, 065018. 21

Unger M. for the PAO Collaboration (2007). *Proceedings of 30th International Cosmic Ray Conference, Merida, Mexico*, 594. 59

Volk H.J. and Zirakashvili V.N. (2003). *Proc. 28th Int. International Cosmic Ray Conference, Tsukuba, Japan*, 2031. 8

Wahlberg H. (2009). *Proceedings of 31st International Cosmic Ray Conference, Lodz, Poland*. 35

Watson A.A. (2006). *Nuclear Physics B,(Proc. Suppl.)*, **151**, 83. 34

Wefel J. P. (1991). *NASA STI/Recon Technical Report A*, **93**, 51971. 7

Werner K. (1993). *Physics Reports*, **232**, 87. 107

Werner K. (2008). *Nuclear Physics B*, **175-176**, 81. 107

Werner K., *et al.* (2001). *arXiv:hep-ph/0209198*. 107

Zatsepin G. T. and Kuzmin V. A. (1966). *JETP Lett.*, **4**, 78. 9

Acknowledgments

I would like to thank the Auger group of Catania: Professor Antonio Insolia who has accepted me into the group and has allowed me to work on this doctoral thesis, Rossella Caruso who has advised me throughout the period, and finally Simone Riggi, Manlio De Domenico, Mario Scuderi and Giuseppe De Mauro for their help in my studies and for the nice moments spent in our laboratory.
I am particularly grateful to Antonella Castellina who has accepted me in the Auger group of Torino and who has helped to plan my PhD thesis just as it is, and with her, I also thank: Marco Aglietta, Simone Maldera, Luca Latronico and Raffaella Bonino. Among them, I am particularly indebted to Simone for his valuable help and his infinite availability to teach me many things.
I cannot forget to thank also my family, for the support given in the past three years.